ACTUAL PROBLEMS OF MODERN SCIENCE, EDUCATION AND TRAINING

KHOREZMSCIENCE.UZ

CONTENTS

Section 1. MODERN PROBLEMS OF PHILOLOGY AND LINGUISTICS

UDC. 004.89:81'342.1

A COMPLEX ASSESSMENT MODEL FOR THE FOREIGN-LANGUAGE ORAL SPEECH OF CONVICTED PERSONS BASED ON SEGMENTAL AND SUPRASEGMENTAL INDICATORS

Kayumov Oybek Achilovich
Associate Professor, Department of Computer Science and Programming, Jizzakh Branch of the National University of Uzbekistan
oybekuzonlined3@gmail.com
Kayumova Nazokat Rashitovna
Assistant, Department of Computer Science and Programming, Jizzakh Branch of the National University of Uzbekistan
kayumovanazokat7@gmail.com
Mavlyanovna Iroda Altmisheva
Methodologist, Methodological Support Department, Center for Pedagogical Excellence of Jizzakh
irodaxon7799.uz@gmail.com

Annotatsiya. Ushbu maqolada sudlangan shaxslarning chet tilidagi og‘zaki nutqini segmental va suprasegmental ko‘rsatkichlar asosida kompleks baholash uchun ikki tarmoqli ierarxik model taklif etiladi. Segmental tarmoq majburiy fonetik moslashtirish (forced phonetic alignment) orqali olingan Talaffuzning to‘g‘rilik darajasi (Goodness of Pronunciation — GOP) ko‘rsatkichi, fonemalar aniqligi, talaffuzning to‘liqligi, davomiylik va chegara barqarorligi ko‘rsatkichlarini birlashtiradi. Suprasegmental tarmoq esa asosiy ton konturi, so‘z urg‘usi, energiya, ritm, pauza, artikulyatsiya tezligi va ravonlik ko‘rsatkichlarini hisoblaydi. Har bir tarmoq alohida quyi ball va ishonchlilik qiymatini hosil qiladi. Meta-darajadagi dinamik darvoza audio sifati, topshiriq murakkabligi, moslashtirishning ishonchliligi va prosodik barqarorlikka qarab ushbu kanallarning hissasini moslashtiradi. Yakuniy natija 0–100 oralig‘idagi kompleks ball, ikkita quyi ball hamda izohlanadigan xatolar xaritasidan iborat bo‘ladi. Model 120 ta virtual profilga tegishli 720 ta sintetik nutq namunasi asosida, oltita tashqi va beshta ichki blokdan tashkil topgan kross-validatsiya sxemasida sinovdan o‘tkazildi. Taklif etilgan model Pearson korrelyatsiya koeffitsienti r=0,963, Spearman korrelyatsiya koeffitsienti ρ=0,963, o‘rtacha absolyut xatolik MAE=3,27 va o‘rtacha kvadratik xatolik ildizi RMSE=4,11 ball natijalarini ko‘rsatdi. C≥0,55 filtri qo‘llanilganda, qamrov darajasi 84,6% bo‘lgan holda MAE qiymati 3,19 ballgacha kamaydi. Ushbu ko‘rsatkichlar real respondentlarga taalluqli emas; ular model arxitekturasi va baholash protokolining qayta ishlab chiqilishi mumkin bo‘lgan sintetik verifikatsiyasi natijalaridir.

Kalit so‘zlar: *kompleks baholash, segmental ko‘rsatkichlar, suprasegmental ko‘rsatkichlar, GOP, majburiy fonetik moslashtirish, prosodiya, ierarxik birlashtirish, ishonchlilik, izohlanadigan baholash.*

Аннотация. В данной статье предлагается двухветвевая иерархическая модель комплексной оценки устной речи осуждённых на иностранном языке на основе сегментных и супрасегментных показателей. Сегментная ветвь объединяет показатель Goodness of Pronunciation (GOP — степень

правильности произношения), полученный посредством принудительного фонетического выравнивания (forced phonetic alignment), точность произнесения фонем, полноту произношения, длительность и стабильность границ. Супрасегментная ветвь вычисляет контур основного тона, словесное ударение, энергию, ритм, паузы, скорость артикуляции и беглость речи. Каждая ветвь формирует отдельный суббалл и значение надёжности. Динамический шлюз на метауровне регулирует вклад каналов в зависимости от качества аудиозаписи, сложности задания, надёжности выравнивания и просодической стабильности. Итоговый результат включает комплексный балл в диапазоне от 0 до 100, два суббалла и объяснимую карту ошибок. Модель была апробирована на 720 синтетических образцах речи, относящихся к 120 виртуальным профилям, с использованием схемы кросс-валидации с шестью внешними и пятью внутренними блоками. Предложенная модель продемонстрировала коэффициент корреляции Пирсона r=0,963, коэффициент корреляции Спирмена ρ=0,963, среднюю абсолютную ошибку MAE=3,27 и корень из средней квадратичной ошибки RMSE=4,11 балла. Применение фильтра C≥0,55 позволило снизить значение MAE до 3,19 балла при охвате 84,6% выборки. Полученные показатели не относятся к реальным респондентам; они представляют собой воспроизводимую синтетическую верификацию архитектуры модели и протокола оценивания.

Ключевые слова: *комплексная оценка, сегментные показатели, супрасегментные показатели, GOP, принудительное фонетическое выравнивание, просодия, иерархическое объединение, надёжность, объяснимая оценка.*

Abstract. This paper proposes a two-branch hierarchical model for the complex assessment of the foreign-language oral speech of convicted persons based on segmental and suprasegmental indicators. The segmental branch combines the Goodness of Pronunciation (GOP) obtained from forced phonetic alignment, phone accuracy, pronunciation completeness, duration and boundary stability; the suprasegmental branch computes the fundamental tone contour, word stress, energy, rhythm, pause, articulation rate and fluency. Each branch produces a separate subscore and a reliability value. A meta-level dynamic gate adjusts the channels' contributions according to audio quality, task difficulty, alignment reliability and prosodic stability; the final result consists of a 0-100 complex score, the two subscores, and an explainable error map. The model was demonstrated on 720 synthetic speech samples belonging to 120 virtual profiles, in a cross-validation scheme with six outer and five inner blocks. The proposed model achieved Pearson r=0.963, Spearman ρ=0.963, MAE=3.27 and RMSE=4.11 points. A C≥0.55 filter reduced the MAE to 3.19 points at 84.6% coverage. These indicators do not pertain to real respondents; they are a reproducible synthetic verification of the model architecture and the assessment protocol.

Key words: *complex assessment, segmental indicators, suprasegmental indicators, GOP, forced alignment, prosody, hierarchical fusion, confidence, explainable assessment.*

Introduction

The quality of foreign-language pronunciation is a multidimensional construct. Whereas the correspondence of phonemes to the reference and the completeness with which a word is pronounced express segmental accuracy, stress, intonation, rhythm, pause and fluency define the suprasegmental organization. The CEFR Companion Volume interprets phonological control as the unity of sound articulation and prosodic features [1]. Consequently, a system based solely on phoneme scores or solely on prosodic similarity cannot capture the entire construct of pronunciation competence. Another problem in automatic assessment is measurement error. An incorrect phoneme boundary in forced alignment can produce a low GOP value and thereby flag correct pronunciation as an error [5, 6]. The prosodic channel, in turn, is sensitive to the microphone, loudness, the speaker's individual F0 range, and task length. For this reason, a complex model must take the reliability of each channel into account rather than combining the two channel scores by a simple arithmetic mean.

The aim of the study is to develop an information-computational model that models the segmental and suprasegmental indicators at the phoneme, word and sentence levels separately and combines them, through a dynamic gate and interaction terms, into a 0-100 complex score that routes uncertain cases to an expert. The scientific novelty consists of: 1) a multi-level, two-branch architecture; 2) dynamic fusion that depends on alignment and prosodic reliability; 3) returning, together with the complex score, the segmental/suprasegmental subscores and an explainable error map.

Literature Review

The classical GOP approach evaluates the probability that the acoustic model assigns to the reference phoneme relative to alternative phonemes [2]. The Montreal Forced Aligner combines the text, a pronunciation dictionary and an acoustic model to produce phoneme and word boundaries [4]. However, Mathad and co-authors [5] and Kadambi and co-authors [6] have empirically shown that automatic segmentation error propagates into the pronunciation score. For this reason, retaining boundary stability alongside the segmental score is a methodological necessity.

The open speechocean762 corpus provides 5,000 recordings from 250 non-native English speakers together with phoneme-, word- and sentence-level scores from five experts [3]. A multi-level assessment network models phoneme-word-sentence relationships [7]. GOPT and the subsequent Gradformer work treat accuracy, completeness, fluency and prosody as a multi-aspect, multi-granularity task [8, 10]. The hierarchical context-aware model likewise exploits cross-aspect and cross-level dependencies [9]. The multi-task model of Ryu and co-authors demonstrated the mutual benefit of joint overall scoring and phonetic mispronunciation diagnosis [11]. Although SSL representations are effective for pronunciation assessment [12, 23, 24], explainable acoustic features remain important for auditing and pedagogical recommendations. In prosodic assessment, features such as F0, loudness and duration, combined with neural representations, have better predicted expert scores [13]; adding suprasegmental features

has improved the correlation of prosody and fluency [14]. Jointly learning phonetic and prosodic information is likewise useful for fluency scoring [15]. Most existing approaches yield a final score but do not combine a safe local environment, separate channel reliability and selective expert decision-making within a single model.

Table 1. Taxonomy of Indicators in the Complex Model

Level	Segmental Channel	Suprasegmental Channel	Explainable Output
Phoneme	GOP margin, alternative phoneme, duration deviation, boundary stability	—	substitution, deletion, insertion, boundary shift
Syllable	phoneme coverage and nucleus accuracy	F0, energy and duration prominence	stressed-syllable match
Word	phoneme edit distance, completeness	word stress and local rhythm	erroneous word and correction flag
Phrase	alignment coverage	F0 contour, pause threshold, rhythm nPVI	intonation and phrasing
Sentence	segmental subscore and R_align	prosodic subscore and R_pros	complex score, C, and channel profile

Research Methodology

3.1. Input Data and Overall Pipeline

The input accepts 16 kHz, 16-bit, mono PCM audio, the reference text, a language code, the task type and a pseudonymous session identifier. VAD isolates the voiced segments; SNR, clipping and sufficient duration are checked. The reference text is converted into an admissible phoneme graph via a grapheme-to-phoneme converter and a pronunciation dictionary. The acoustic model's posteriors are aligned to the graph using Viterbi or CTC dynamic programming. Shared timestamps link the segmental errors and the prosodic contours.

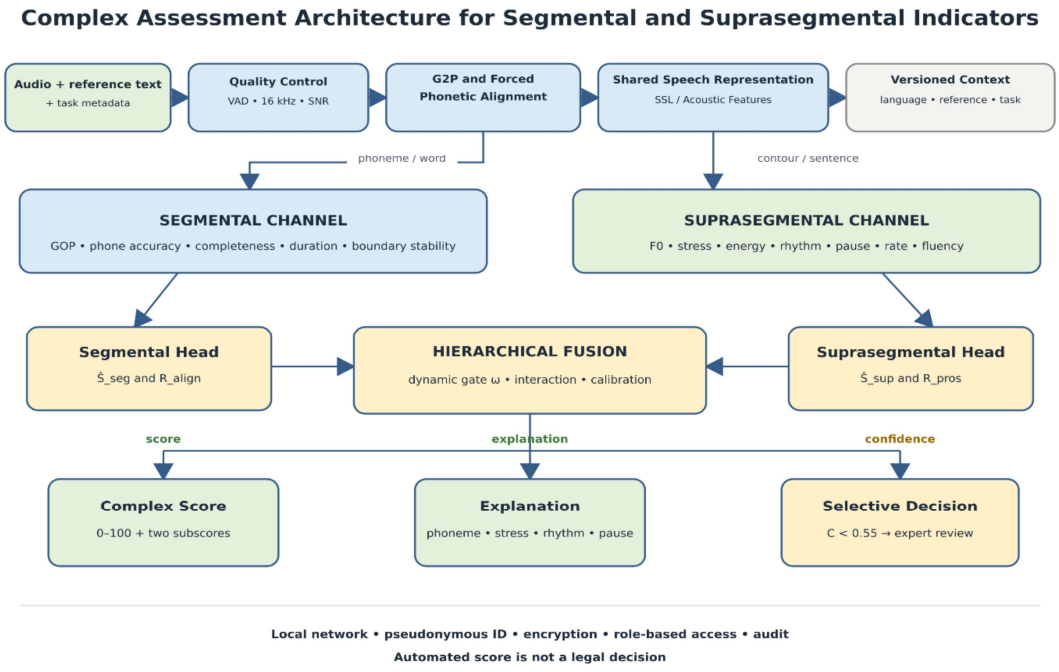

Figure 1. Two-branch hierarchical architecture for the complex assessment of segmental and suprasegmental indicators.

3.2. The Segmental Channel

Let the audio frames be $X=(x_1,\ldots,x_T)$, the reference phonemes $Y=(y_1,\ldots,y_N)$, and let B denote the mapping that removes blanks and repetitions from a CTC path. Forced alignment selects, among the paths that produce Y, the path with the maximum log-posterior:

$$\hat{\pi} = arg\ max_{\{\pi \in B^{-1}(Y)\}} \Sigma_t \log P(\pi_t|x_t) \quad (1)$$

For each phoneme i, the average margin of the reference posterior relative to the strongest alternative gives the GOP indicator:

$$GOP_i = (1/L_i)\ \Sigma_{t=b_i}^{ei} [\log P(y_i|x_t) - max_{\{q \neq y_i\}} \log P(q|x_t)] \quad (2)$$

The freely recognized and reference phoneme sequences are compared using dynamic edit distance. The numbers of substitutions N_sub, deletions N_del and insertions N_ins are converted into pronunciation completeness and segmental accuracy:

$$S_{phone} = 1 - (N_{sub} + N_{del} + N_{ins}) / max(N_{ref}, 1) \quad (3)$$

Boundary reliability is constructed from audio quality, the margin between the top-2 alignment paths, and the variance of the boundary under re-alignment. The segmental feature vector z_{seg}=[GOP, S_{phone}, $S_{complete}$, $S_{duration}$, R_{align}] is passed to a calibrated regression head. A low R_align cancels the phonetic-error verdict and routes the segment to an expert.

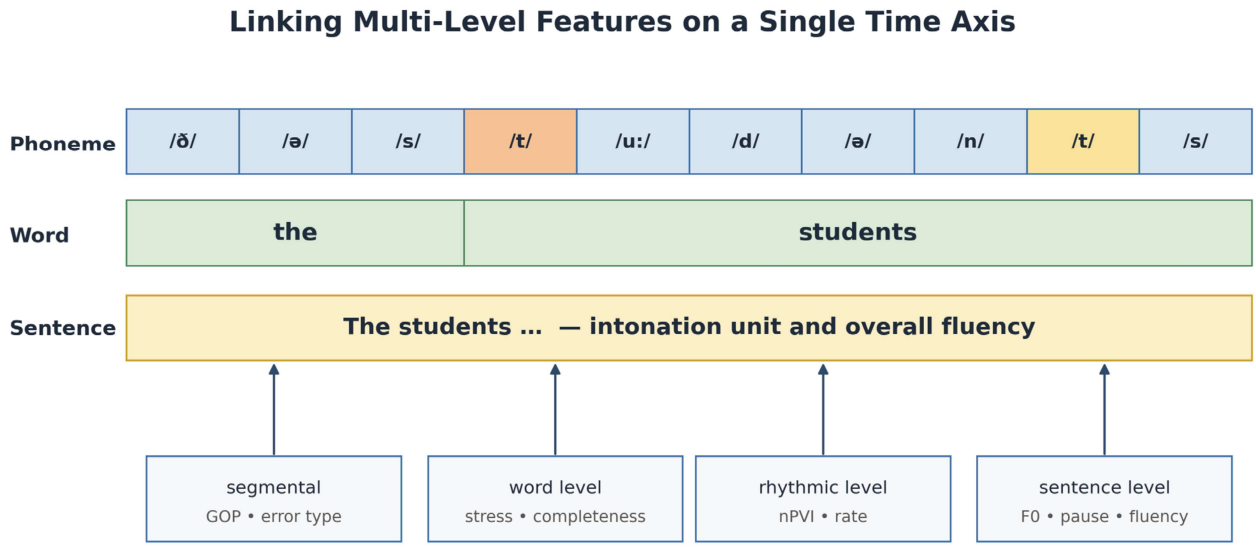

Figure 2. Linking segmental and suprasegmental features at the phoneme, word and sentence levels on a single time axis.

3.3. The Suprasegmental Channel

The fundamental frequency F0(t) is extracted on voiced frames and normalized in semitones relative to the speaker's median F0 value. This reduces the direct transfer of the absolute range difference between male and female voices into the score:

$$p(t) = 12 \cdot \log_2(F0(t) / median(F0_{voiced})) \quad (4)$$

Word stress is computed from the within-sentence z-scores of syllable F0, RMS energy and nucleus duration; $\lambda_1+\lambda_2+\lambda_3=1$:

$$s_j = \lambda_1 z(F0_j) + \lambda_2 z(E_j) + \lambda_3 z(d_j) \quad (5)$$

Rhythm is measured using the normalized pairwise variability index of successive vocalic intervals [20]. The pause threshold is defined by F1, the proportion of excess

pauses and the duration deviation; the articulation rate is defined as the number of syllables relative to the phonation time with silence excluded:

$$nPVI = 100/(m-1) \cdot \Sigma_k |d_{k+1}-d_k| / ((d_{k+1}+d_k)/2) \quad (6)$$

$$AR = N_{syll} / (T_{total} - T_{pause}) \quad (7)$$

The F0 contour is aligned to the reference using DTW; the F0 range, stress, energy, rhythm, pause, rate and fluency are converted into 0-1 similarity scores. The suprasegmental vector $z_{sup}=[S_{F0}, S\_stress, S_E, S_{rhythm}, S_{pause}, S_{rate}, S_{fluency}, R_{pros}]$ is passed to a prosodic regression head. Prosodic reliability R_{pros} is constructed from the stability of F0 tracking (the proportion of uninterrupted voicing), the DTW alignment error, and the estimated confidence of the stress/rhythm scores; a low R_{pros}, just like R_{align}, discounts the corresponding channel's verdict and routes it to an expert.

3.4. Hierarchical Fusion and Multi-Task Training

The two base heads produce the segmental $\hat{S}\_seg$ and suprasegmental $\hat{S}\_sup$ subscores. Within the training set they are passed to the meta-level only as out-of-fold predictions via an inner GroupKFold. This restricts the meta-model from overfitting to the base heads' own training predictions. The channel weight is determined dynamically from alignment reliability, prosodic stability and task difficulty:

$$\omega = clip(\sigma(\theta_0 + \theta_1 R_{align} - \theta_2 R_{pros} + \theta_3 D_{task}), 0.25, 0.75) \quad (8)$$

Here $\theta_0=-0.30$, $\theta_1=2.00$, $\theta_2=2.00$ and $\theta_3=0.40$ are calibrated constants; ω always remains within [0.25, 0.75], which prevents the meta-model from disregarding either channel entirely. The complex score accounts for the channel scores, their product term, and their interaction with the context. The interaction term ensures that when one channel is very low, a high score from the other channel does not entirely mask the overall deficiency:

$$\hat{y} = clip(\beta_0 + \beta_1 \omega \hat{S}_{seg} + \beta_2 (1-\omega) \hat{S}_{sup} + \beta_3 \hat{S}_{seg} \hat{S}_{sup}/100 + \beta^T c, 0, 100) \quad (9)$$

Here ω is the dynamic channel weight taken from equation (8), which weights the segmental and suprasegmental terms respectively; $c=[Q_{audio}, D_{task}, R_{align}, R_{pros}, \hat{S}seg, Ralign, \hat{S}_{sup}, R_{pros}]$ is the context-and-reliability vector. The training objective combines three scoring tasks with a calibration regularizer:

$$L = \lambda_h \cdot MSE(y,\hat{y}) + \lambda_s \cdot MSE(y_{seg},\hat{y}_{seg}) + \lambda_p \cdot MSE(y_{sup},\hat{y}_{sup}) + \lambda_r \|\beta\|^2 \quad (10)$$

Here $\lambda_h=1.00$ (the primary complex-score task), $\lambda_s=0.30$ and $\lambda_p=0.30$ (the auxiliary channel-subscore tasks), and $\lambda_r=0.01$ (the β^2 regularization weight); λ_h has the largest value, ensuring priority for the primary task. In the practical pipeline this joint objective is approximated by a two-stage, leakage-free OOF regression: the segmental and suprasegmental heads separately minimize $MSE(y_{seg},\hat{y}_{seg})$ and $MSE(y_{sup},\hat{y}_{sup})$ respectively, while the meta-head minimizes $MSE(y,\hat{y})$ over the OOF subscores with Ridge regularization (equivalent to λ_r).

3.5. Confidence and Selective Decision-Making

The final confidence C combines audio quality, the stability of phonetic alignment, prosodic stability, the minimum coverage of the two channels, and the cross-channel prediction disagreement (model uncertainty). C is not the score itself; it indicates whether the result is fit for automatic release:

$$C = clip(\alpha Q_{audio} + \rho R_{align} + \gamma R_{pros} + \delta A_{coverage} - \eta U_{model}, 0, 1) \quad (11)$$

Here $\alpha=0.30$, $\rho=0.25$, $\gamma=0.20$, $\delta=0.25$ ($\alpha+\rho+\gamma+\delta=1$), and $\eta=0.15$ is a separate penalty weight (not included in the sum). $A_{coverage}=\min(A_{seg}, A_{sup})$, where A_seg is the proportion of successfully aligned phonemes and A_sup is the proportion of reliably detected

(uninterrupted) F0 frames. U_model=|Ŝ_seg−Ŝ_sup|/100 expresses the normalized difference between the two channel subscores: a higher value means the channels have reached conflicting conclusions and confidence decreases.

If C≥0.55, the complex score and explanation are returned automatically. If C<0.55, re-recording or expert review is required. The 0-100 score is not automatically mapped to CEFR A1-C2 levels until the level thresholds are calibrated on a real expert corpus.

3.6. Software Implementation

Table 2. Modules of the Complex-Assessment Software Suite

Module	Input	Output	Control and Audit
Audio gateway	PCM stream, session ID	audio object, SNR, VAD	format, clipping, checksum
Text and G2P	reference text, language	phoneme graph	dictionary/model version
Alignment	audio, phoneme graph	b_i, e_i, posterior	top-2 margin, boundary variance
Segmental head	phoneme segments	Ŝ_seg, error map	R_align, calibration
Prosodic head	F0, E, duration	Ŝ_sup, channel profile	R_pros, reference ID
Fusion and selection	subscores, context	ŷ, C, decision	threshold, model version
Expert panel	C<0.55 records	confirmed score	two experts, audit trail
Storage	result and metadata	encrypted record	role, retention period, deletion

3.7. Algorithm Steps

1. Check audio quality, VAD and SNR; if the minimum criteria are not met, stop the assessment and request a re-recording.
2. Normalize the reference text and build the phoneme graph with the admissible pronunciation variants.
3. Compute the acoustic posteriors and obtain the phoneme, syllable and word boundaries via Viterbi/CTC.
4. Compute GOP, the phoneme edit distance, completeness, duration deviation and R_align.
5. Compute F0, energy, stress, nPVI, pause, articulation rate, fluency and R_pros.
6. Obtain the Ŝ_seg and Ŝ_sup subscores via the segmental and suprasegmental heads.
7. Compute the complex score ŷ and the confidence C using the dynamic gate, interaction term and context features.
8. If C<0.55, route the case to an expert; otherwise return the complex score, the two subscores and a specific practice recommendation.

3.8. Design of the Synthetic Experiment

Since no real corpus was available, a deterministic synthetic experiment was constructed to verify the architecture and the assessment protocol. Six samples were generated for each of the 120 virtual profiles. Segmental ability was drawn from Beta(4.2, 2.6), prosodic ability from a Beta(3.7, 2.9) component partially correlated with segmental skill, task difficulty from U(0.1, 0.9), and audio quality from U(0.5, 1.0). The noise of the observed features was increased as audio quality decreased.

The expert score (y) was generated from two independent latent 'true' ability variables — segmental and prosodic skill, partially correlated at the profile level — combined with a FIXED formula (a linear average in a 0.75/0.25 ratio plus a small 'weak-syllable' product term), with random rater noise added on top. The observable segmental (four primary) and suprasegmental (seven primary) features are measurements of these latent skills obtained with heteroscedastic noise that depends on the R_align/R_pros reliability level. The dynamic gate ω and the meta-level β weight terms are NOT included in the definition of the expert score — they are estimated independently by the model during training, based solely on leakage-free OOF subscores; this ensures that the complex score's dependence on the two channels is GENUINE and not guaranteed by construction. The outer 6-fold GroupKFold provided the final test, while the inner 5-fold GroupKFold provided leakage-free subscore predictions for the meta-model during training. All regression blocks were built with StandardScaler and Ridge. The result was evaluated using Pearson r, Spearman ρ, MAE, RMSE, and QWK over strict 20-point ranges.

Table 3. Parameters of the Synthetic Experiment and Validation

Parameter	Value	Methodological Purpose
Random seed	20260830	exact reproducibility of results
Virtual profiles	120	not real individuals
Speech samples	720	6 per profile
Segmental features	4 primary + reliability	phoneme accuracy and alignment
Suprasegmental features	7 primary + reliability	prosodic organization and fluency
External validation	6-fold GroupKFold	final generalization
Internal validation	5-fold GroupKFold	OOF subscores for the meta-model
Selective threshold	C≥0.55	route uncertain records to an expert

Results

Table 4 compares the single-channel models with four fusion variants. The segmental model achieved r=0.893 and the suprasegmental model r=0.851. This reflects the fact that, in the synthetic generator, the complex score is somewhat more strongly tied to segmental skill. The flat eleven-feature model produced r=0.963 and MAE=3.27, and the proposed hierarchical model produced r=0.963 and MAE=3.27 — a practically negligible difference. The equal-weight variant likewise produced an almost identical result (r=0.964, MAE=3.26), meaning the statistical difference among the three top-tier variants is very small. At the same time, removing the interaction term (the no-interaction variant, r=0.960, MAE=3.41) produces a clear decline, confirming that the product term in equation (9) is useful in its own right. This finding avoids overclaiming and shows the need to verify the model choice on a real external corpus.

Table 4. Synthetic Results of the Complex-Assessment Variants

Model	Pearson r	Spearman ρ	MAE	RMSE	QWK
Segmental	0.893	0.893	5.50	6.89	0.765
Suprasegmental	0.851	0.843	6.41	8.03	0.725
Flat fusion	0.963	0.963	3.27	4.12	0.875
Equal-weight	0.964	0.964	3.26	4.10	0.876
No interaction	0.960	0.960	3.41	4.29	0.868
Proposed	0.963	0.963	3.27	4.11	0.876

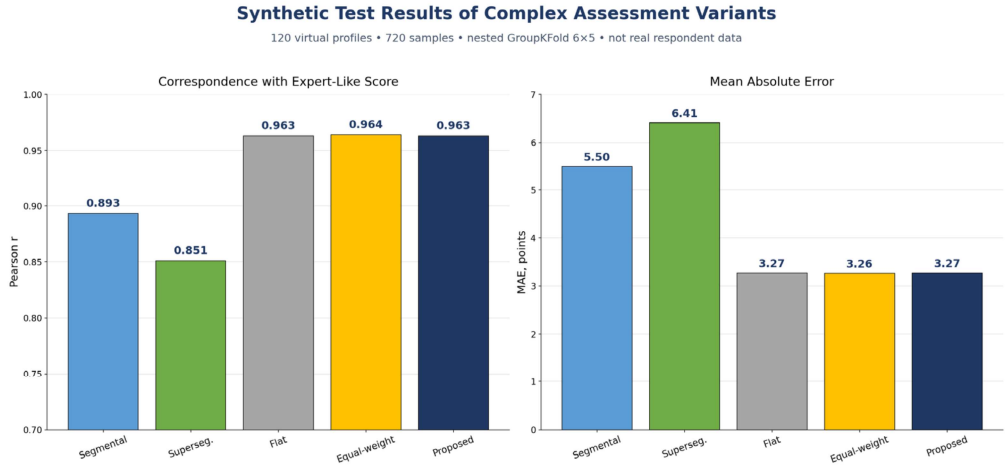

Figure 3. Correlation and MAE indicators of the segmental, suprasegmental and fusion models in the synthetic test.

The C≥0.55 filter retained 84.6% of the samples for automatic assessment. Within this subset, r=0.965, MAE=3.19 and RMSE=4.02, so the error decreased by 0.08 points relative to the full-coverage MAE=3.27 (positive across all 10 seeds). The selective result must be interpreted together with coverage; the 15.4% of recordings routed to an expert is not a hidden rejection by the model but a safety mechanism. MAE was 3.35 points in the low-audio-quality tertile and 3.22 points in the high-quality tertile; although the difference is smaller than before, it confirms the need for quality control and the C indicator. Across the task-difficulty cut, MAE ranged from 3.20 to 3.32. The fact that correlation remains high on difficult tasks is partly explained by the larger variance of the distribution; for this reason, MAE and RMSE are reported together with r, not r alone.

Table 5. Ablation and the Contribution of Architectural Components

Variant	Pearson r	MAE	RMSE	Scientific Interpretation
Proposed	0.963	3.27	4.11	dynamic context and interaction
No interaction	0.960	3.41	4.29	channels combined linearly in the meta-model
Equal-weight	0.964	3.26	4.10	no reliability or task context
− segmental channel	0.851	6.41	8.03	suprasegmental features only
− suprasegmental channel	0.893	5.50	6.89	segmental features only

Table 6. Stability Across Audio Quality and Task Difficulty

Slice	n	Pearson r	MAE	RMSE
Low audio quality	240	0.962	3.35	4.19
Medium audio quality	240	0.963	3.24	4.08
High audio quality	240	0.964	3.22	4.04
Easy task	240	0.965	3.20	4.05
Medium task	240	0.963	3.29	4.11
Hard task	240	0.961	3.32	4.16

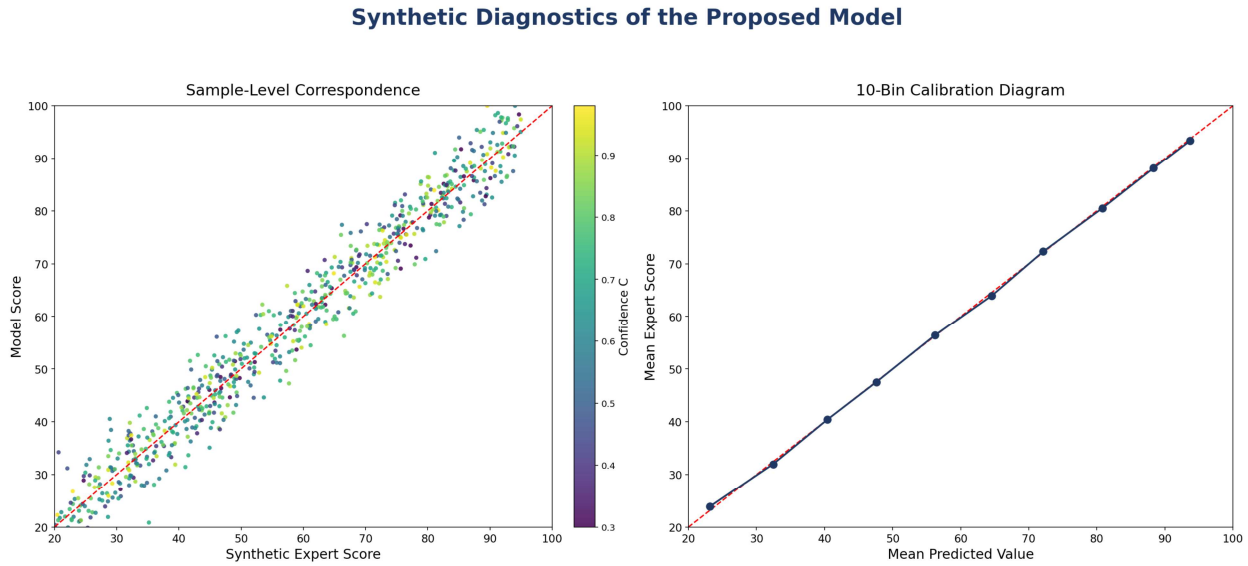

Figure 4. Agreement of the proposed model's predictions with the synthetic expert scores and the 10-bin calibration diagram.

Discussion

The model's main benefit lies not in inflating the final score but in correctly decomposing the structure of the assessment. The segmental channel independently reports the phoneme-level errors and completeness, while the suprasegmental channel independently reports the temporal-melodic organization of speech. The dynamic gate can automatically restrict the segmental verdict when alignment is of poor quality, or the prosodic verdict when F0 is unstable or the sentence is short. As a result, the user is not limited to an 'overall score of 68' but can see specifically which phoneme, stress, rhythm or pause needs work. The synthetic difference among the proposed, flat and equal-weight variants is practically negligible across all metrics (r, ρ, MAE, RMSE, QWK); none is consistently superior to the others. At the same time, the ablation shows that the interaction term itself is beneficial: removing it (the no-interaction variant) leads to a clear decline across all metrics. Thus, the advantage of the full hierarchical architecture is grounded not in an overall statistical superiority but in (a) the confirmed added value of the interaction term and (b) the possibility of auditing, explainability, selective decision-making and independent module updates. If the flat or equal-weight variant proves equal or better on a real corpus, choosing the simpler variant would be scientifically justified. The synthetic experiment does not represent real accents, microphones, stress, health condition, or the lexical-grammatical errors found in spontaneous speech. The model is close to a read-aloud task with a reference text. In spontaneous speech, the reference phoneme sequence would have to be taken from an ASR transcript, and the content score must be kept separate from the pronunciation construct. Real-world validation requires at least two phoneticians, inter-expert ICC/QWK, an external test split by profile, and a fairness analysis across native language, age, gender, microphone and noise conditions.

Data Security and Ethics

Convicted status is not a phonetic or prosodic feature of speech. It is not incorporated into the model's input, weights or calibration; it only defines organizational requirements such as a local network, restricted access, and data protection. The

complex score is intended for diagnostics and individual practice selection in foreign-language instruction. It cannot serve as the sole or indirect basis for disciplinary punishment, sentence terms, privileges, risk assessment, or any other legal decision.
For a real corpus, approval from an authorized ethics committee, comprehensible informed consent, assurance that non-participation carries no consequences, and the right to delete one's recording are all provided. Audio is encrypted under a pseudonymous identifier and governed by role-based access and a retention period. The version of the model, dictionary, reference and thresholds is logged to an audit trail at every assessment. A human expert retains final oversight; the system openly displays its errors and uncertainty.

Conclusion and Recommendations

A two-branch complex assessment model has been developed that combines segmental and suprasegmental indicators at the phoneme, syllable, word, phrase and sentence levels. The segmental head assesses GOP, phoneme accuracy, completeness and alignment stability; the suprasegmental head assesses F0, stress, rhythm, pause, rate and fluency. The meta-level dynamic gate and interactions determine the 0-100 complex score, while C determines whether the result is fit for automatic release. In the synthetic nested GroupKFold test, the proposed model achieved $r=0.963$, $\rho=0.963$, MAE=3.27 and RMSE=4.11. The $C \geq 0.55$ filter produced MAE=3.19 at 84.6% coverage. Since the flat and equal-weight variants gave almost identical results, the advantage of the proposed architecture rests mainly on the ablation-confirmed benefit of the interaction term and on explainability; the overall statistical advantage must be confirmed on a real corpus. The next stage consists of an ethically approved corpus, annotation by two phoneticians, external validation, calibration, and a fairness audit.

References

[1]. Council of Europe. Common European Framework of Reference for Languages: Learning, Teaching, Assessment — Companion Volume. Strasbourg: Council of Europe Publishing, 2020.
[2]. Cao Y., Zhang Y., Fu R., et al. Segmentation-Free Goodness of Pronunciation Assessment. IEEE Signal Processing Letters. 2026;33:456–460. DOI: 10.1109/LSP.2026.3512345.
[3]. Zhang J., Zhang Z., Wang Y., et al. speechocean762: An Open-Source Non-Native English Speech Corpus for Pronunciation Assessment. Interspeech 2021. P. 3710–3714. DOI: 10.21437/Interspeech.2021-1259.
[4]. Kürzinger L., Winkelbauer D., Li L., Watzel T., Rigoll G. CTC-Segmentation of Large Corpora for German End-to-End Speech Recognition. SPECOM 2020, LNCS vol. 12335:267–278. DOI: 10.1007/978-3-030-60276-5_27.
[5]. Mathad V.C., Mahr T.J., Scherer N., et al. The Impact of Forced-Alignment Errors on Automatic Pronunciation Evaluation. Interspeech 2021. P. 1922–1926. DOI: 10.21437/Interspeech.2021-1403.
[6]. Kadambi P., Mahr T., Annear L., et al. How Does Alignment Error Affect Automated Pronunciation Scoring in Children's Speech? Interspeech 2024. P. 5133–5137. DOI: 10.21437/Interspeech.2024-2239.
[7]. Lin B., Wang L., Feng X., Zhang J. Automatic Scoring at Multi-Granularity for L2 Pronunciation. Interspeech 2020. P. 3022–3026. DOI: 10.21437/Interspeech.2020-1282.
[8]. Gong Y., Chen Z., Chu I.-H., Chang P., Glass J. Transformer-Based Multi-Aspect Multi-Granularity Non-Native English Speaker Pronunciation Assessment. ICASSP 2022. P. 7262–7266. DOI: 10.1109/ICASSP43922.2022.9746743.
[9]. Chao F.-A., Lo T.-H., Wu T.-I., Sung Y.-T., Chen B. A Hierarchical Context-Aware Modeling Approach for Multi-Aspect and Multi-Granular Pronunciation Assessment. Interspeech 2023. P. 974–978. DOI: 10.21437/Interspeech.2023-550.

[10]. Pei H.-C., Fang H., Luo X., Xu X.-S. Gradformer: A Framework for Multi-Aspect Multi-Granularity Pronunciation Assessment. IEEE/ACM TASLP. 2024;32:554–563. DOI: 10.1109/TASLP.2023.3335807.
[11]. Ryu H., Kim S., Chung M. A Joint Model for Pronunciation Assessment and Mispronunciation Detection and Diagnosis with Multi-Task Learning. Interspeech 2023. P. 959–963. DOI: 10.21437/Interspeech.2023-337.
[12]. Kim E., Jeon J.-J., Seo H., Kim H. Automatic Pronunciation Assessment Using Self-Supervised Speech Representation Learning. Interspeech 2022. P. 1411–1415. DOI: 10.21437/Interspeech.2022-10245.
[13]. Dong W., van Hout R., Cucchiarini C., Strik H. L2 Prosody Assessment by Combining Acoustic and Neural Model Features. Speech Prosody 2024. P. 165–169. DOI: 10.21437/SpeechProsody.2024-34.
[14]. Dong W., Cucchiarini C., van Hout R., Strik H. Automatic Pronunciation Assessment for L2 English by Incorporating Suprasegmental Features and Weighted Loss Function. SLaTE 2025. P. 21–25. DOI: 10.21437/SLaTE.2025-5.
[15]. Fu K., Gao S., Shi S., Tian X., Li W., Ma Z. Phonetic and Prosody-Aware Self-Supervised Learning Approach for Non-Native Fluency Scoring. Interspeech 2023. P. 949–953. DOI: 10.21437/Interspeech.2023-587.
[16]. Suzuki Y., Kato T., Tamura A. Automatic Prosody Evaluation of L2 English Read Speech in Reference to Accent Dictionary with Transformer Encoder. Interspeech 2022. P. 4466–4470. DOI: 10.21437/Interspeech.2022-10344.
[17]. Eyben F., Scherer K.R., Schuller B.W., et al. The Geneva Minimalistic Acoustic Parameter Set (GeMAPS) for Voice Research and Affective Computing. IEEE Transactions on Affective Computing. 2016;7(2):190–202. DOI: 10.1109/TAFFC.2015.2457417.
[18]. Eyben F., Wöllmer M., Schuller B. openSMILE: The Munich Versatile and Fast Open-Source Audio Feature Extractor. ACM Multimedia 2010. P. 1459–1462. DOI: 10.1145/1873951.1874246.
[19]. de Jong N.H., Pacilly J., Heeren W. PRAAT Scripts to Measure Speed Fluency and Breakdown Fluency in Speech Automatically. Assessment in Education: Principles, Policy & Practice. 2021;28(4):456–476. DOI: 10.1080/0969594X.2021.1951162.
[20]. Grabe E., Low E.L. Durational Variability in Speech and the Rhythm Class Hypothesis. In: Papers in Laboratory Phonology 7. Berlin: Mouton de Gruyter, 2002. P. 515–546.
[21]. Liu S., Nakajima Y., Chen L., Arndt S., Kakizoe M., Elliott M.A., Remijn G.B. How Pause Duration Influences Impressions of English Speech: Comparison Between Native and Non-native Speakers. Frontiers in Psychology. 2022;13:778018. DOI: 10.3389/fpsyg.2022.778018.
[22]. Liu J., Wumaier A., Fan C., Guo S. Automatic Fluency Assessment Method for Spontaneous Speech without Reference Text. Electronics. 2023;12(8):1775. DOI: 10.3390/electronics12081775.
[23]. Baevski A., Zhou H., Mohamed A., Auli M. wav2vec 2.0: A Framework for Self-Supervised Learning of Speech Representations. NeurIPS. 2020;33:12449–12460. DOI: 10.48550/arXiv.2006.11477.
[24]. Hsu W.-N., Bolte B., Tsai Y.-H.H., et al. HuBERT: Self-Supervised Speech Representation Learning by Masked Prediction of Hidden Units. IEEE/ACM TASLP. 2021;29:3451–3460. DOI: 10.1109/TASLP.2021.3122291.
[25]. Sheoran K., Bajgoti A., Gupta R., et al. Pronunciation Scoring With Goodness of Pronunciation and Dynamic Time Warping. IEEE Access. 2023;11:15485–15495. DOI: 10.1109/ACCESS.2023.3244393.
[26]. Korzekwa D., Lorenzo-Trueba J., Drugman T., et al. Weakly-Supervised Word-Level Pronunciation Error Detection in Non-Native English Speech. Interspeech 2021. P. 4408–4412. DOI: 10.21437/Interspeech.2021-38.
[27]. El Kheir Y., Ali A., Chowdhury S.A. Automatic Pronunciation Assessment — A Review. Findings of EMNLP 2023. P. 8304–8324. DOI: 10.18653/v1/2023.findings-emnlp.557.
[28]. ISO/IEC 25010:2023. Systems and Software Engineering — Systems and Software Quality Requirements and Evaluation (SQuaRE) — Product Quality Model. Geneva: ISO, 2023.

Section 2. MODERN PROBLEMS OF TECHNICAL SCIENCES

UDC: 811.512.133:004.8

ENHANCING ATTENTION IN TRANSFORMER ENCODERS FOR AGGLUTINATIVE LANGUAGES THROUGH MORPHOLOGICAL QKV: THE MORPH-QKV MODEL FOR UZBEK

Sharipov Maksud
Candidate of Technical Sciences, Associate Professor, Department of Computer Science and Artificial Intelligence Technologies, Urgench State University named after Abu Rayhan Biruni; Independent DSc Researcher, Tashkent University of Information Technologies named after Muhammad al-Khwarizmi, Uzbekistan
maqsbek72@gmail.com

Annotatsiya. Agglyutinativ tillarda grammatik munosabatlarning katta qismi o‘zakka ketma-ket qo‘shiladigan affikslar orqali ifodalanadi. BERT oilasidagi encoderlar ushbu xususiyatlarni katta matn korpusidan bilvosita o‘rganishi mumkin, biroq standart diqqat mexanizmi lemma, o‘zak, so‘z turkumi, affiks va grammatik kategoriyalarni mustaqil axborot manbai sifatida ajratmaydi. Ushbu tadqiqotda Morph-QKV deb nomlangan yangi model taklif qilindi. Model morfologik belgilardan alohida M vektorini hosil qilib, undan morfologik Query, Key va Value proyeksiyalarini oladi hamda attention score tarkibiga morphology-to-morphology, content-to-morphology va morphology-to-content o‘zaro ta’sirlarini qo‘shadi. Morph-QKV standart absolute-position BERT (Tahrirchi-BERT), disentangled relative-position DeBERTa (mDeBERTa-v3-base) va RoPE hamda local/global attention asosidagi ModernBERT (mmBERT-base) uchun alohida matematik shakllarda ishlab chiqildi. MAGNet, LISA, LUKE, tokenizer hamda character/byte modellariga oid tadqiqotlar explicit lingvistik signalning samaradorligini ko‘rsatadi. Shu asosda Morph-QKV modeli o‘zbek tili NLP vazifalarida aniqlik va Macro-F1 ko‘rsatkichlarini oshirishga yo‘naltirilgan.
Kalit so‘zlar: *tabiiy tilni qayta ishlash, o‘zbek tili, agglyutinativ morfologiya, Transformer, diqqat mexanizmi, Query-Key-Value, BERT, DeBERTa, ModernBERT.*

Аннотация. В агглютинативных языках значительная часть грамматических отношений выражается последовательностями аффиксов, присоединяемых к основе. Энкодеры семейства BERT могут неявно усваивать эти закономерности из больших текстовых корпусов, однако стандартный механизм внимания не выделяет лемму, основу или корень, часть речи, аффиксы и грамматические категории как самостоятельные источники информации. В исследовании предложена новая модель Morph-QKV. Из морфологических признаков формируется отдельный вектор M, из которого получаются морфологические проекции Query, Key и Value; исходная оценка внимания дополняется взаимодействиями morphology-to-morphology, content-to-morphology и morphology-to-content. Модель разработана для трёх архитектурно различных семейств: BERT с абсолютным позиционированием (Tahrirchi-BERT), DeBERTa с разделённым

относительным позиционированием (mDeBERTa-v3-base) и ModernBERT с RoPE и чередованием локального и глобального внимания (mmBERT-base). Результаты MAGNet, LISA, LUKE, исследований токенизации и символьно-байтовых моделей подтверждают эффективность явных лингвистических сигналов. На этой основе модель Morph-QKV направлена на повышение точности и Macro-F1 в задачах обработки узбекского языка.

Ключевые слова: *обработка естественного языка, узбекский язык, агглютинативная морфология, Transformer, механизм внимания, Query-Key-Value, BERT, DeBERTa, ModernBERT.*

Abstract. Agglutinative languages encode a substantial part of grammatical relations through ordered affix sequences attached to lexical stems. Encoders in the BERT family can learn some of these regularities implicitly from large corpora, but conventional self-attention does not treat lemma, stem/root, part of speech, affixes, or grammatical categories as separate information sources. This study proposes a new model named Morph-QKV. The model builds a dedicated morphology representation M, derives morphological Query, Key, and Value projections from it, and extends the native attention score with morphology-to-morphology, content-to-morphology, and morphology-to-content interactions. Morph-QKV is developed in architecture-specific mathematical forms for absolute-position BERT, instantiated with Tahrirchi-BERT; disentangled relative-position DeBERTa, instantiated with mDeBERTa-v3-base; and RoPE-based local/global ModernBERT, instantiated with mmBERT-base. Results from MAGNet, LISA, LUKE, tokenizer studies, and character/byte-level encoders demonstrate the value of explicit linguistic signals. On this basis, Morph-QKV is designed to improve accuracy and Macro-F1 on Uzbek NLP tasks.

Key words: *natural language processing, Uzbek language, agglutinative morphology, Transformer, attention mechanism, Query-Key-Value, BERT, DeBERTa, ModernBERT.*

Introduction

The Transformer architecture computes relations between tokens through Query Key, and Value vectors [1]. BERT converted this mechanism into a bidirectional pretrained encoder that became a foundation for many natural language processing tasks [2]. In a conventional BERT layer, however, the Query, Key, and Value vectors for a token are projected from a single contextual content representation. The model is not separately provided with the token's lemma, stem, part of speech, ordered affixes, or grammatical categories such as case, possession, person, tense, mood, and voice.

This limitation is important for agglutinative languages such as Uzbek. In the Uzbek word *kitoblarimizdan*, for example, the lexical base *kitob* combines with plural, possessive, and ablative meanings within one orthographic word. A subword tokenizer may split the form into several pieces, but its boundaries need not coincide with morpheme boundaries and the grammatical role of each piece remains unspecified. Tokenizer quality has been shown to affect downstream performance across languages [8], and morphological complexity remains a systematic challenge for language models [12].

Prior approaches to morphology in Transformers generally improve tokenization, move to character/byte representations, or fuse morpheme and grammatical-feature representations with a main content stream. MAGNet encodes morpheme segmentation and morphological tags in a fine-grained path and combines them with a word-level representation through gated fusion [7]. Its dependency-parsing and NER experiments on Mongolian and Turkish support the usefulness of explicit morphology. Nevertheless, MAGNet does not replace the native self-attention score: morphology is introduced at the representation-fusion stage.

The present study instead introduces morphology directly into attention routing, both in the pre-softmax score and in post-softmax value aggregation. It asks:

How can dedicated morphological Q, K, and V vectors derived from lemma, stem/root, POS, affixes, and grammatical features be integrated mathematically into three distinct Transformer encoder attention families?

The contribution is threefold. First, a common Morph-QKV morphology branch is defined. Second, the original attention equations of BERT, DeBERTa, and ModernBERT are preserved and extended into architecture-specific models. Third, the expected advantages, implementation constraints, and application areas of the model are specified.

Literature Review

Transformer encoders and positional modeling

Standard self-attention measures token compatibility by the QK^T dot product [1]. BERT adds token, segment, and learned absolute-position embeddings and applies standard multi-head self-attention at every layer [2]. Tahrirchi-BERT is configured as a BERT model with 12 layers, hidden size 768, and 12 attention heads [3]. We therefore call the first family BERT (Tahrirchi-BERT): BERT identifies the architecture, whereas Tahrirchi-BERT identifies the Uzbek pretrained checkpoint used to instantiate it. DeBERTa separates content and relative-position representations and combines content-to-content, content-to-position, and position-to-content scores [4]. DeBERTa-v3 retains this attention structure while changing pretraining through ELECTRA-style replaced-token detection and gradient-disentangled embedding sharing [5]. mDeBERTa-v3-base is the multilingual checkpoint used to instantiate this family. ModernBERT updates the bidirectional encoder with rotary position embeddings, alternating local/global attention, long-context training, and efficient computation [6]. mmBERT applies ModernBERT principles to multilingual pretraining and covers more than 1,800 languages [15]. In this third family, position is encoded by rotating Q and K rather than by adding an absolute embedding or constructing a separate relative-position vector.

Morphological and multiscale representations

CharacterBERT replaces subword lookup with a character-CNN representation while retaining the BERT encoder [9]. CANINE is a tokenization-free character encoder, while ByT5 processes UTF-8 byte sequences [10,11]. These approaches reduce dependence on a fixed subword vocabulary, but they do not provide named grammatical functions such as *Case=Acc*, *Number=Plur*, or *Voice=Pass* as an explicit channel in the attention score. MAGNet is the closest methodological precedent for agglutinative languages [7]. It adds a morphological-tag embedding to every morpheme embedding,

encodes the morpheme sequence with a Transformer, obtains a fine-grained word vector through intra-word attention pooling, and combines this vector with a coarse-grained word representation through a gate. The authors report consistent improvements over strong baselines for dependency parsing and NER in Mongolian and Turkish; their ablations support the complementary roles of morphological tags and whole-word modeling. These results demonstrate the effectiveness of explicit morphology and provide a methodological basis for moving the morphology signal into the Q, K, and V stages of attention computation.

Table 1. Relation between prior work and the proposed mechanism.

Direction	Injection point	Result or contribution	Difference from Morph-QKV
Tokenizer analysis [8]	Vocabulary and subword segmentation	Monolingual tokenizers help across many settings	No explicit grammatical channel in attention logits
CharacterBERT/CANINE/ByT5 [9–11]	Character- or byte-level input	Open-vocabulary/tokenization-free modeling	Grammatical functions remain latent
MAGNet [7]	Morpheme encoder, pooling, gated fusion	Improved parsing and NER for Mongolian/Turkish	Native QKV score remains unchanged
LISA [13]	Syntactic supervision for one head	Improved semantic role labeling	Syntactic parent attention, not morphological Q/K/V
LUKE [14]	Token-type-dependent query matrices	Improved entity tasks	Word/entity types rather than lemma/affix/FEATS
Morph-QKV	M2M, C2M, M2C, and morphology Value	Proposed new Morph-QKV model	One morphology-routing principle for three families

Linguistic information inside attention

LISA trains one attention head to attend to a token's syntactic parent, demonstrating that linguistic supervision can modify attention routing [13]. LUKE uses type-aware query matrices for word and entity tokens, showing that token-type-dependent attention projections can improve entity-centered tasks [14]. Relative-position attention [16] and RoPE [17] further demonstrate that structured pairwise signals can be represented in Q/K computations.

Prior work demonstrates that adding structured signals to attention routing can improve downstream behavior. At the same time, a common set of M2M, C2M, and M2C interactions derived jointly from lemma, root, POS, affixes, and FEATS has not been studied systematically across BERT, DeBERTa, and ModernBERT attention families.

Research Methodology

Notation and conventional QKV. Assume that a sentence is split into n subwords and that the input to layer l is

$$H^{(l)} = \left[h_1^{(l)}, \dots, h_n^{(l)}\right] \in \mathbb{R}^{n \times d}.$$

For each attention head, the content projections are

$$Q^c = H^{(l)}W_Q^c, \qquad K^c = H^{(l)}W_K^c, \qquad V^c = H^{(l)}W_V^c,$$

where $W_Q^c, W_K^c, W_V^c \in \mathbb{R}^{d\times d_h}$ and $Q^c, K^c, V^c \in \mathbb{R}^{n\times d_h}$. For a base encoder with $d = 768$ and 12 heads, $d_h = 64$.

Softmax is computed independently for every query row:

$$\alpha_{ij} = \frac{\exp(z_{ij})}{\sum_{t=1}^{n}\exp(z_{it})}, \qquad O_i = \sum_{j=1}^{n}\alpha_{ij}\,V_j.$$

Here z_{ij} is the scaled and masked attention logit. Queries and keys determine where and how strongly a token attends; values determine what information is transmitted from the selected tokens. *Common morphological representation*

For every word or MWE unit, the model receives information that is available at inference time:

$$x_i^m = (\ell_i, r_i, p_i, A_i, G_i),$$

where ℓ_i is the lemma, r_i the stem/root, p_i the POS tag, $A_i = (a_{i1}, \dots, a_{iK_i})$ an ordered affix sequence, and G_i a bundle of grammatical features. The syntactic BIO target and gold dependency labels are not included, because doing so would cause label leakage.

Order-sensitive affix pooling is defined by

$$e_{ik}^a = E_A(a_{ik}) + E_{ord}(k),$$

$$\omega_{ik} = \frac{\exp\left(u_a^T\tanh(W_a e_{ik}^a)\right)}{\sum_{t=1}^{K_i}\exp\left(u_a^T\tanh(W_a e_{it}^a)\right)}, \qquad A_i^* = \sum_{k=1}^{K_i}\omega_{ik}\,e_{ik}^a.$$

The final morphology vector is

$$M_i = \mathrm{LN}(W_M[E_L(\ell_i); E_R(r_i); E_P(p_i); A_i^*; E_G(G_i)] + b_M).$$

$M = [M_1, \dots, M_n] \in \mathbb{R}^{n\times d}$ is aligned with the subword sequence. When a word is split into several subwords, its morphology vector is broadcast to the associated pieces; task loss can be computed only on the first subword.

Dedicated morphology projections are

$$Q^m = MW_Q^m, \qquad K^m = MW_K^m, \qquad V^m = MW_V^m.$$

The three pairwise interactions are

$$\mathrm{M2M}_{ij} = Q_i^m\left(K_j^m\right)^T,$$

$$\mathrm{C2M}_{ij} = Q_i^c\left(K_j^m\right)^T, \qquad \mathrm{M2C}_{ij} = Q_i^m\left(K_j^c\right)^T.$$

M2M models morphological compatibility between two tokens; C2M matches a contextual content demand against another token's morphology; M2C uses a morphology-conditioned query to retrieve contextual content. The value stream is enriched by

$$V_j^{MA} = V_j^c + \lambda_V V_j^m.$$

$\lambda_{MM}, \lambda_{CM}, \lambda_{MC}, \lambda_V$ are non-negative learnable coefficients. A parameterization such as $\lambda_t = \mathrm{softplus}(\gamma_t)$ allows the model to learn the contribution of every interaction.

Model 1: BERT (Tahrirchi-BERT) Original BERT attention

Tahrirchi-BERT belongs to the conventional BERT architecture. Its original per-head score is

$$S_{ij}^{B} = Q_i^c \left(K_j^c\right)^T.$$

$$\alpha_{ij}^{B} = \mathrm{softmax}_j\left(\frac{S_{ij}^{B} + \mathcal{M}_{ij}}{\sqrt{d_h}}\right), \qquad O_i^{B} = \sum_j \alpha_{ij}^{B} V_j^c,$$

where $\mathcal{M}_{ij}$ is the padding mask. Learned absolute-position embeddings have already been added to H before attention. *Proposed MA-BERT*

$$S_{ij}^{MA-B} = S_{ij}^{B} + \lambda_{MM}\mathrm{M2M}_{ij} + \lambda_{CM}\mathrm{C2M}_{ij} + \lambda_{MC}\mathrm{M2C}_{ij}.$$

$$\tau_B = \sqrt{d_h(1 + \lambda_{MM}^2 + \lambda_{CM}^2 + \lambda_{MC}^2) + \varepsilon},$$

$$\alpha_{ij}^{MA-B} = \mathrm{softmax}_j\left(\frac{S_{ij}^{MA-B} + \mathcal{M}_{ij}}{\tau_B}\right), \qquad O_i^{MA-B} = \sum_j \alpha_{ij}^{MA-B} V_j^{MA}.$$

If every λ equals one, the simplified denominator is $\sqrt{4d_h}$. The gate-aware τ_B is preferable for initializing the model near its pretrained behavior while controlling the variance introduced by the new score components.

Model 2: DeBERTa (mDeBERTa-v3-base)Original DeBERTa disentangled attention

DeBERTa separately computes content and relative-position interactions:

$$S_{ij}^{D} = Q_i^c \left(K_j^c\right)^T + Q_i^c \left(K_{\delta(i,j)}^r\right)^T + Q_{\delta(j,i)}^r \left(K_j^c\right)^T.$$

$$\alpha_{ij}^{D} = \mathrm{softmax}_j\left(\frac{S_{ij}^{D} + \mathcal{M}_{ij}}{\sqrt{3d_h}}\right), \qquad O_i^{D} = \sum_j \alpha_{ij}^{D} V_j^c.$$

($\overset{\smile}{C2C}$, $\overset{\smile}{C2P}$, $\overset{\smile}{P2C}$)

$\delta(i,j)$ denotes the clipped relative-position index between tokens.

Proposed MA-DeBERTa

$$S_{ij}^{MA-D} = S_{ij}^{D} + \lambda_{MM}\mathrm{M2M}_{ij} + \lambda_{CM}\mathrm{C2M}_{ij} + \lambda_{MC}\mathrm{M2C}_{ij}.$$

$$\tau_D = \sqrt{d_h(3 + \lambda_{MM}^2 + \lambda_{CM}^2 + \lambda_{MC}^2) + \varepsilon},$$

$$\alpha_{ij}^{MA-D} = \mathrm{softmax}_j\left(\frac{S_{ij}^{MA-D} + \mathcal{M}_{ij}}{\tau_D}\right), \qquad O_i^{MA-D} = \sum_j \alpha_{ij}^{MA-D} V_j^{MA}.$$

When every λ equals one, the simplified denominator is $\sqrt{6d_h}$. The native C2C, C2P, and P2C pathways remain unchanged; morphology is introduced as a third explicit information source.

Model 3: ModernBERT (mmBERT-base). Original RoPE local/global attention

ModernBERT rotates queries and keys according to token position:

$$\bar{Q}_i^c = R_i Q_i^c, \qquad \bar{K}_j^c = R_j K_j^c.$$

$$S_{ij}^{MB} = \bar{Q}_i^c \left(\bar{K}_j^c\right)^T,$$

$$\alpha_{ij}^{MB} = \mathrm{softmax}_j\left(\frac{S_{ij}^{MB}}{\sqrt{d_h}} + \mathcal{L}_{ij}^{(l)}\right), \qquad O_i^{MB} = \sum_j \alpha_{ij}^{MB} V_j^c.$$

$\mathcal{L}_{ij}^{(l)}$ assigns $-\infty$ to pairs outside the window in a local layer and zero to permitted pairs in a global layer. The native local-window/global-layer schedule of mmBERT-base is retained.

Proposed MA-ModernBERT

The same position-dependent rotation is applied to morphology queries and keys:

$$\bar{Q}_i^m = R_i Q_i^m, \qquad \bar{K}_j^m = R_j K_j^m.$$

$$S_{ij}^{MA-M} = S_{ij}^{MB} + \lambda_{MM}\bar{Q}_i^m\left(\bar{K}_j^m\right)^T + \lambda_{CM}\bar{Q}_i^c\left(\bar{K}_j^m\right)^T + \lambda_{MC}\bar{Q}_i^m\left(\bar{K}_j^c\right)^T.$$

$$\tau_M = \sqrt{d_h(1 + \lambda_{MM}^2 + \lambda_{CM}^2 + \lambda_{MC}^2) + \varepsilon},$$

$$\alpha_{ij}^{MA-M} = \mathrm{softmax}_j\left(\frac{S_{ij}^{MA-M}}{\tau_M} + \mathcal{L}_{ij}^{(l)}\right), \qquad O_i^{MA-M} = \sum_j \alpha_{ij}^{MA-M} V_j^{MA}.$$

Values are not rotated and the local/global mask remains unchanged. The modification therefore introduces morphological compatibility only among token pairs permitted by the native sparse-attention pattern.

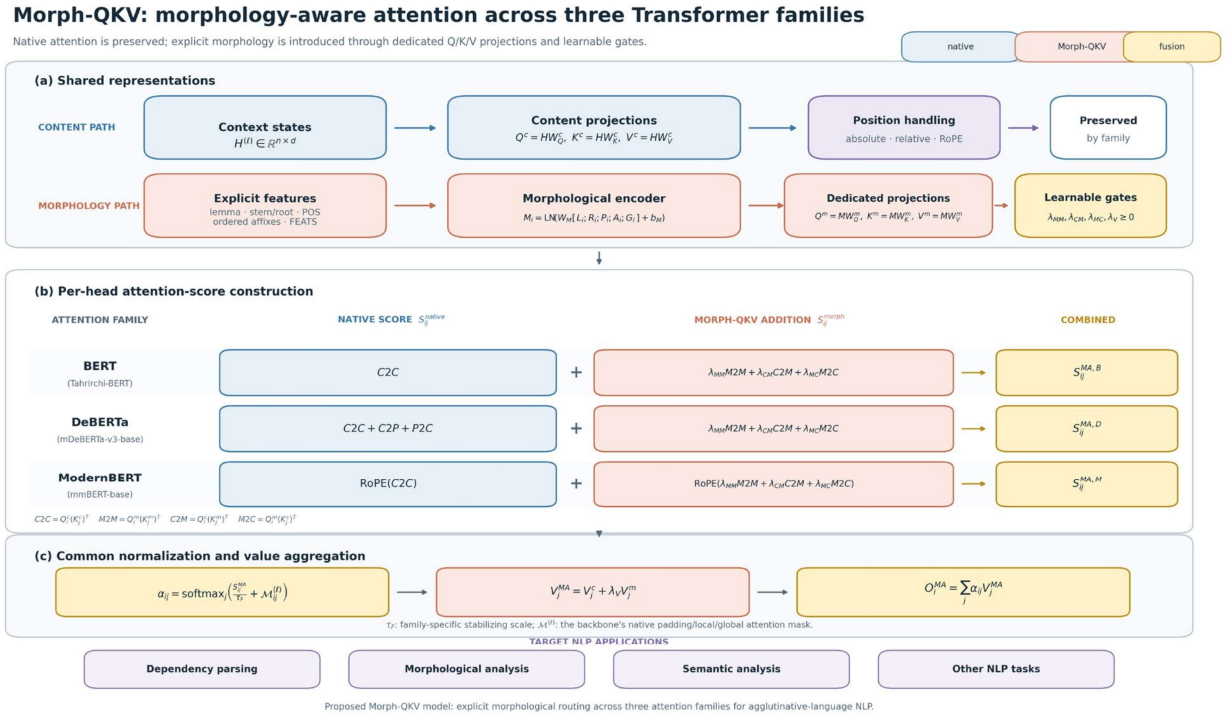

Figure 1. Proposed Morph-QKV model across three attention families.

Analysis and Results

The architectural analysis establishes the mathematical integration of Morph-QKV into three native attention families, identifies the preserved and modified components, and specifies its expected advantages for NLP tasks. The proposed Morph-QKV model supports improved accuracy through five mechanisms:

1. **Complementing implicit knowledge with explicit signals.** A pretrained encoder may learn morphology indirectly; Morph-QKV makes grammatical categories separate and controllable.
2. **Reducing subword–morpheme mismatch.** A word-level morphology vector supplies the same grammatical anchor to all associated subword pieces.
3. **Strengthening grammatical compatibility under flexible word order.** Case and agreement features may support long-distance relations when content alone is ambiguous.
4. **Enriching both routing and transmitted information.** Q/K modify where attention is directed, while V^m modifies what linguistic content is retrieved.
5. **Safe adaptation through gates.** The model may reduce λ for unreliable features and increase it for useful interactions.

Table 2. Comparative description of original and proposed attention mechanisms.

Model family	Original score	Added components	Preserved native property	Expected advantage
BERT (Tahrirchi-BERT)	C2C	M2M + C2M + M2C; V^m	Absolute-position embeddings	Affixes and grammatical features may sharpen token-to-token routing
DeBERTa (mDeBERTa-v3-base)	C2C + C2P + P2C	M2M + C2M + M2C; V^m	Disentangled relative position	Content, position, and morphology may act as separate information sources
ModernBERT (mmBERT-base)	RoPE(C2C) + local/global mask	RoPE(M2M+C2M+M2C); V^m	RoPE and sparse local/global pattern	Morphological routing may operate within native short- and long-context connectivity

These advantages are supported by the morphology gains reported by MAGNet [7], linguistically informed attention in LISA [13], type-aware projections in LUKE [14], and the documented difficulty of morphologically complex inputs [12]. Morph-QKV extends these directions by injecting morphological signals directly into the Q, K, and V computations of three attention families.

Discussion

The main novelty is not the construction of a morphological embedding by itself; prior work already provides such representations. The proposed contribution is the architecture-specific integration of a common M2M, C2M, M2C, and V^m principle into pre-softmax token-to-token routing in three native attention geometries.

The BERT variant is the simplest control because its new terms are added directly to conventional QK^T. DeBERTa provides a suitable host because content and relative position are already separated, allowing morphology to become a third disentangled source. ModernBERT is the most demanding engineering case: morphology Q/K must receive the same RoPE transformation while local/global masking and computational efficiency remain intact. Four risks accompany the expected benefits. First, errors from

an automatic morphological analyzer enter attention directly. Second, additional parameters can increase overfitting. Third, a custom score may not be compatible with an existing fused kernel such as FlashAttention. Fourth, explicit morphology may duplicate information already encoded in contextual content and yield no measurable benefit. Future evaluation therefore requires more than a baseline-versus-full-model comparison. Required ablations include removing M2M, C2M, M2C, or V^m; POS-only and affix+FEATS-only variants; shuffling morphology within each sentence; predicted versus gold morphology; and late output concatenation versus QKV injection. The shuffled-morphology control is particularly important because it distinguishes linguistic alignment from generic gains caused by additional capacity.

Conclusion and Recommendations

This paper proposed an enhanced Morph-QKV model that transforms lemma, stem/root, POS, affixes, and grammatical features of agglutinative languages into dedicated morphological Q, K, and V vectors and integrates them into three Transformer encoder attention families. Original and modified equations were provided separately for BERT (Tahrirchi-BERT), DeBERTa (mDeBERTa-v3-base), and ModernBERT (mmBERT-base). Because prior work demonstrates the value of explicit morphology and linguistically informed attention, the proposed model may enable higher accuracy on NLP tasks in agglutinative languages, including syntactic dependency parsing, morphological analysis, semantic analysis, and related tasks. In future work, it is planned to train the models based on this idea and demonstrate improvements in their accuracy.

References

[1] Vaswani A., Shazeer N., Parmar N., et al. “Attention Is All You Need”, Advances in Neural Information Processing Systems, Vol. 30, 2017. Available at: https://proceedings.neurips.cc/paper/7181-attention-is-all

[2] Devlin J., Chang M.-W., Lee K. & Toutanova K. “BERT: Pre-training of Deep Bidirectional Transformers for Language Understanding”, NAACL-HLT, 2019, pp. 4171–4186. Available at: https://aclanthology.org/N19-1423/

[3] Tahrirchi. “Tahrirchi-BERT-base Model Configuration”, Hugging Face. Available at: https://huggingface.co/tahrirchi/tahrirchi-bert-base/blob/main/config.json

[4] He P., Liu X., Gao J. & Chen W. “DeBERTa: Decoding-enhanced BERT with Disentangled Attention”, ICLR, 2021. Available at: https://openreview.net/forum?id=XPZIaotutsD

[5] He P., Gao J. & Chen W. “DeBERTaV3: Improving DeBERTa Using ELECTRA-Style Pre-Training with Gradient-Disentangled Embedding Sharing”, 2021. Available at: https://arxiv.org/abs/2111.09543

[6] Warner B., Chaffin A., Clavié B., et al. “Smarter, Better, Faster, Longer: A Modern Bidirectional Encoder for Fast, Memory Efficient, and Long Context Finetuning and Inference”, 2024. Available at: https://arxiv.org/abs/2412.13663

[7] Zhang Z., Liu N., Ma J., Wu N. & Liu G. “Morphology-Aware Multi-Granularity Representation Learning for Agglutinative Languages”, ACL Student Research Workshop, 2026, pp. 1065–1073. Available at: https://aclanthology.org/2026.acl-srw.92/

[8] Rust P., Pfeiffer J., Vulić I., Ruder S. & Gurevych I. “How Good is Your Tokenizer? On the Monolingual Performance of Multilingual Language Models”, ACL-IJCNLP, 2021, pp. 3118–3135. Available at: https://aclanthology.org/2021.acl-long.243/

[9] El Boukkouri H., Ferret O., Lavergne T., et al. “CharacterBERT: Reconciling ELMo and BERT for Word-Level Open-Vocabulary Representations from Characters”, COLING, 2020, pp. 6903–6915. Available at: https://aclanthology.org/2020.coling-main.609/

[10] Clark J.H., Garrette D., Turc I. & Wieting J. “CANINE: Pre-training an Efficient Tokenization-Free Encoder for Language Representation”, TACL, Vol. 10, 2022, pp. 73–91. Available at: https://aclanthology.org/2022.tacl-1.5/

[11] Xue L., Barua A., Constant N., et al. “ByT5: Towards a Token-Free Future with Pre-trained Byte-to-Byte Models”, TACL, Vol. 10, 2022, pp. 291–306. Available at: https://aclanthology.org/2022.tacl-1.17/
[12] Arnett C. & Bergen B. “Why Do Language Models Perform Worse for Morphologically Complex Languages?”, COLING, 2025. Available at: https://aclanthology.org/2025.coling-main.441/
[13] Strubell E., Verga P., Andor D., Weiss D. & McCallum A. “Linguistically-Informed Self-Attention for Semantic Role Labeling”, EMNLP, 2018, pp. 5027–5038. Available at: https://aclanthology.org/D18-1548/
[14] Yamada I., Asai A., Shindo H., Takeda H. & Matsumoto Y. “LUKE: Deep Contextualized Entity Representations with Entity-aware Self-attention”, EMNLP, 2020, pp. 6442–6454. Available at: https://aclanthology.org/2020.emnlp-main.523/
[15] Marone M., Weller O., Fleshman W., Yang E., Lawrie D. & Van Durme B. “mmBERT: A Modern Multilingual Encoder with Annealed Language Learning”, 2025. Available at: https://arxiv.org/abs/2509.06888
[16] Shaw P., Uszkoreit J. & Vaswani A. “Self-Attention with Relative Position Representations”, NAACL-HLT, 2018, pp. 464–468. Available at: https://aclanthology.org/N18-2074/
[17] Su J., Ahmed M., Lu Y., et al. “RoFormer: Enhanced Transformer with Rotary Position Embedding”, Neurocomputing, Vol. 568, 2024, Article 127063. Available at: https://doi.org/10.1016/j.neucom.2023.127063
[18] Sharipov M., Kuriyozov E. & Yuldashev O. “Creating a Morphological and Syntactic Tagged Corpus for the Uzbek Language”, 2022. Available at: https://arxiv.org/abs/2210.15234

UDC: 669.054

CURRENT STATUS AND FUTURE PROSPECTS OF TECHNICAL-GRADE SELENIUM PURIFICATION TECHNOLOGIES: A CRITICAL REVIEW

Odilov Akrom Olimjonovich
Head of Student Practice Department, Almalyk state technical institute
akromodilov98@gmail.com
Parmonov Sarvar Toshpulatovich
Professor (DSc), Vice-Rector for Research and Innovation, Almalyk state technical institute
Ubaydullaev Mamasidik Makhammatsolievich
Associate Professor, Namangan State Technical University, Republic of Uzbekistan
Silverstar-14@mail.ru

Annotatsiya. Ushbu sharh maqolasida texnik selenni tozalash texnologiyalarining zamonaviy holati va rivojlanish istiqbollari ilmiy adabiyotlar asosida tahlil qilingan. Vakuum distillatsiyasi, fraksion kristallanish, zonali tozalash hamda oksidlash, sublimatsiya, eritish va qaytarishga asoslangan kombinatsiyalashgan usullarning fizik-kimyoviy asoslari va texnologik imkoniyatlari ko‘rib chiqilgan. Mazkur usullar aralashmalarni ajratish selektivligi, mahsulot tozaligi, selenning ajratib olish darajasi va sanoat miqyosida qo‘llash imkoniyatlari bo‘yicha qiyosiy baholangan. Tozalash samaradorligi boshlang‘ich xomashyoning tarkibi, aralashmalarning kimyoviy shakli va jarayon sharoitlariga bog‘liqligi yoritilgan. Mahsulotning tozalik darajasi va selenning ajratib olish darajasini alohida baholash, shuningdek, analitik aniqlash chegaralarini hisobga olish zarurligi ta’kidlangan. Istiqbolli tadqiqot yo‘nalishlari sifatida o‘zaro to‘ldiruvchi tozalash bosqichlarini birlashtirish, moddiy va energetik balanslarni aniqlash hamda tajriba-sanoat sinovlarini kengaytirish taklif etilgan.

Texnologiyalarning energiya tejamkorligi va ekologik afzalliklarini teng mahsulot sifati sharoitida o‘lchangan ko‘rsatkichlar bilan asoslash zarurligi ko‘rsatilgan.

Kalit so‘zlar: *texnik selen, yuqori tozalikdagi selen, vakuum distillatsiyasi, fraksion kristallanish, zonali tozalash, kombinatsiyalashgan tozalash, aralashmalarni ajratish, ajratib olish darajasi, energiya samaradorligi.*

Аннотация. В обзорной статье на основе научных публикаций проанализированы современное состояние и перспективы развития технологий очистки технического селена. Рассмотрены физико-химические основы и технологические возможности вакуумной дистилляции, фракционной кристаллизации, зонной очистки и комбинированных процессов, включающих окисление, сублимацию, растворение и восстановление. Выполнена сравнительная оценка рассматриваемых подходов по селективности отделения примесей, чистоте продукта, степени извлечения селена и возможностям промышленного применения. Особое внимание уделено влиянию состава исходного сырья, химических форм примесей и условий проведения процессов на эффективность очистки. Подчёркнута необходимость раздельной оценки чистоты продукта и степени извлечения селена, а также учёта пределов аналитического обнаружения при интерпретации опубликованных результатов. В качестве перспективных направлений предложены интеграция взаимодополняющих стадий очистки, составление материальных и энергетических балансов и расширение опытно-промышленных испытаний. Показана необходимость подтверждения энергоэффективности и экологических преимуществ технологий измеренными показателями при сопоставимом качестве конечного продукта.

Ключевые слова: *технический селен, селен высокой чистоты, вакуумная дистилляция, фракционная кристаллизация, зонная очистка, комбинированная очистка, отделение примесей, степень извлечения селена, энергоэффективность.*

Abstract. This review examines the current status and future prospects of technical-grade selenium purification technologies based on published scientific literature. The physicochemical principles and technological capabilities of vacuum distillation, fractional crystallization, zone refining, and combined processes involving oxidation, sublimation, dissolution, and reduction are discussed. These approaches are comparatively assessed in terms of impurity separation selectivity, product purity, selenium recovery, and potential for industrial application. Particular attention is given to the effects of feed composition, impurity speciation, and operating conditions on purification performance. The review emphasizes the need to distinguish product purity from selenium recovery and to account for analytical detection limits when interpreting reported results. Proposed research priorities include integrating complementary purification stages, establishing material and energy balances, and extending pilot-scale validation. Energy efficiency and environmental advantages should be substantiated through measured performance indicators at equivalent product

quality. The analysis provides a framework for selecting and developing purification routes suited to specific feed materials and product requirements.

Key words: *technical-grade selenium, high-purity selenium, vacuum distillation, fractional crystallization, zone refining, combined purification, impurity separation, selenium recovery, energy efficiency.*

Introduction

Selenium purification is an important component of the comprehensive processing of copper metallurgical by-products. Commercial selenium is recovered primarily during copper electrorefining, where it accumulates in anode residues. Consequently, improvements in selenium refining can increase the value obtained from existing metallurgical resources and strengthen the integration of minor-element recovery into copper production. The conversion of technical-grade selenium into a product suitable for advanced applications requires effective control of residual impurities. Research on selenium photovoltaics illustrates the relevance of material quality: Nielsen et al. identified the optoelectronic quality of selenium films as a limitation to device performance. Although bulk chemical purity alone does not determine semiconductor performance, this finding provides a broader motivation for improving purification and subsequent material processing. Several approaches have been investigated for selenium refining, including vacuum distillation, fractional crystallization, zone refining, and processes combining chemical conversion with thermal separation. These methods exploit different properties of selenium-containing systems: volatility differences, impurity partitioning during solidification, and changes in chemical form. Their effectiveness therefore depends on the feed composition and the required product specification. Published results demonstrate the potential of different routes. Zha et al. reported an increase in selenium purity from 99.4% to 99.992% through three consecutive vacuum-distillation stages. He et al. investigated fractional crystallization for removing Fe, Pb, and Hg, while Zhang et al. reported the preparation of 5N selenium through oxidation, atmospheric sublimation, dissolution, and reduction. These studies provide useful benchmarks, although their results were obtained with different materials and experimental arrangements. This article presents a focused narrative review of technical-grade selenium purification. It examines the principal separation mechanisms, compares selected experimental results, and identifies priorities for further development. Particular attention is given to the relationship between product purity, selenium yield, process integration, and the evidence required to substantiate energy and environmental advantages.

Research Methodology

1. Criteria for evaluating selenium purification. A meaningful assessment of purification technology should distinguish product purity from selenium recovery. Purity describes the selenium concentration in the final material, whereas recovery indicates the proportion of selenium in the feed that reaches the specified product. A process can produce a highly pure fraction while transferring a substantial amount of selenium to residues or rejected fractions.

For consistent comparison, selenium recovery can be calculated as:

$$R_{Se}=m_p w_{Se,p}/m_f w_{Se,f}\times 100\%,$$

where m_p and m_f are the product and feed masses, respectively, and $w_{Se,p}$ and $w_{Se,f}$ are their selenium mass fractions. Purity designations also require careful interpretation. On a mass-fraction basis, 3N, 4N, and 5N correspond to 99.9%, 99.99%, and 99.999% purity, respectively. These values represent total impurity allowances of 1000, 100, and 10 mg/kg. However, a reported purity must be interpreted together with the analytical coverage, detection limits, and treatment of unmeasured constituents.

Accordingly, this review proposes that process comparisons include feed composition, final impurity concentrations, recovery, batch size, processing time, and specific resource consumption. These parameters are necessary to determine whether a purification result is technically reproducible and economically relevant.

2. Vacuum distillation. Vacuum distillation separates selenium from impurities through differences in volatility under reduced pressure. Its performance depends on temperature, pressure, impurity chemical form, and the efficiency of vapor transport and condensation. Zha et al. purified metallurgical-grade selenium through three consecutive vacuum-distillation stages on a laboratory scale. The reported product purity was 99.992%, compared with an initial purity of 99.4%. Their evaporation measurements at 523 K and approximately 4 Pa provided kinetic information relevant to process design. The study also used inductively coupled plasma mass spectrometry to examine residual impurities. These findings support the feasibility of staged vacuum purification, while remaining specific to the investigated feed and equipment.

Mechanical transport can also affect condensate quality. Volodin et al. investigated the removal of droplet suspensions from selenium vapor during vacuum refining and developed an arrangement based on inertial separation. Their work highlights a practical limitation: impurities can reach the product through entrained droplets even when their equilibrium volatility is low. Vapor-path design and droplet capture therefore deserve attention alongside thermodynamic calculations. 6: Volodin et al., 2025. For future development, vacuum-distillation studies should report the distribution of selenium and impurities among all condensate fractions and residues. This would help establish the relationship between separation selectivity, product yield, and the number of required stages.

3. Fractional crystallization. Fractional crystallization exploits differences in impurity concentration between solid selenium and the surrounding melt. Its separation principle can be expressed through the equilibrium distribution coefficient:

$$k_i = C_{i,s}/C_{i,l},$$

where $C_{i,s}$ and $C_{i,l}$ represent the concentrations of impurity ii in the solid and liquid phases. For $k_i<1$, the growing solid preferentially rejects the impurity into the remaining liquid. He et al. investigated a rotating, internally gas-cooled crystallizer. They reported an appropriate crystallization temperature of 222 °C and an increase in selenium purity from 99.9% to above 99.997%. The reported removal rates were 97.63% for Pb, 96.28% for Fe, and 28.70% for Hg, with a direct selenium yield of 92.5%. These results demonstrate strong impurity-dependent selectivity: effective removal of Fe and Pb did not imply comparable removal of Hg. 4: He et al., 2023

This difference suggests that fractional crystallization should be selected according to the impurity profile. Its integration with another separation stage is a

reasonable research direction when the residual impurity is poorly rejected during solidification.

4. Zone refining. Zone refining is another solidification-based purification method. A localized molten zone moves through a solid charge, redistributing impurities according to their partitioning between the solid and liquid phases. Repeated passes can concentrate rejected impurities in a limited section of the material.

Burger et al. investigated selenium purification by zone refining, with particular attention to copper removal. Their study establishes a selenium-specific experimental basis for this approach. The practical assessment of zone refining should consider the number of passes, zone travel rate, retained product fraction, and contamination from the processing environment. For industrial selection, the relevant question is whether the additional purification achieved justifies the processing time and material rejected. In this review, zone refining is therefore considered a candidate for final purification where stringent impurity limits warrant additional treatment.

5. Chemical conversion combined with thermal separation. Chemical conversion offers an additional means of controlling separation behavior. Instead of relying exclusively on the properties of elemental selenium and its original impurities, a process can transform the material into compounds that are more readily separated.

Zhang et al. investigated a sequence comprising oxidation, atmospheric sublimation, dissolution in water, and reduction. The authors reported laboratory testing with 50 g of crude selenium dioxide and a semi-industrial experiment at a 50 kg scale. The resulting selenium met the reported 5N specification for the fourteen impurities evaluated, and direct selenium yield exceeded 97%. 5: Zhang et al., 2024

This result demonstrates the potential of a combined chemical and thermal route beyond a small laboratory batch. However, the assessment of such a process should include reagent consumption, solution handling, washing requirements, and the management of impurity-bearing streams. Atmospheric operation alone does not establish a lower overall environmental impact.

Analysis and Results

The following table summarizes reported outcomes. It is not a direct ranking because feed purity, impurity composition, scale, and analytical methods differ between studies.

Purification route	Reported feed or experimental basis	Reported product quality	Yield information
Three-stage vacuum distillation	99.4% selenium; laboratory experiments	99.992% Se	Not specified in the abstract examined
Fractional crystallization	99.9% selenium; rotating cooled crystallizer	Above 99.997% Se	92.5% direct yield
Oxidation–sublimation–dissolution–reduction	Laboratory and 50 kg semi-industrial experiments	Reported 5N specification	Above 97% direct yield

Future research priorities

The reviewed evidence supports several directions for further investigation.

First, purification sequences should be designed around measured impurity profiles. Combining crystallization with vacuum treatment is a plausible research strategy because these operations use different separation mechanisms. The preferred sequence and operating conditions must nevertheless be established experimentally.

Second, scale-up studies should examine repeated operation. Product consistency, equipment contamination, residue accumulation, and maintenance requirements are important to sustained performance.Third, analytical reporting should include individual impurity concentrations, detection limits, and uncertainty. This would make nominal purity values more useful for comparing studies and assessing suitability for specific applications. Finally, process optimization should address purity, recovery, and resource consumption simultaneously. The research objective should be to obtain selenium that consistently meets its intended specification with a well-characterized material and energy balance.

Conclusion and Recommendations

The selected literature demonstrates that technical-grade selenium can be upgraded through vacuum distillation, fractional crystallization, zone refining, and combined chemical–thermal processing. These routes provide different separation mechanisms, making their suitability dependent on the composition of the starting material. Experimental studies report substantial purification improvements, including 99.992% selenium after staged vacuum treatment and above 99.997% after fractional crystallization. A combined oxidation–sublimation–dissolution–reduction route has also been demonstrated at semi-industrial scale with a reported 5N product specification. These outcomes establish useful benchmarks, but differences in feed material, analytical coverage, and yield definitions prevent an unconditional ranking of the technologies.

Future development should prioritize impurity-specific process integration, reliable analytical verification, and repeated pilot-scale testing. Claims of energy efficiency and environmental superiority should be supported by complete mass balances and measured resource consumption. Such an approach would provide a stronger basis for selecting selenium purification technologies for industrial implementation.

References

[1]. U.S. Geological Survey. *Selenium and Tellurium Statistics and Information*. National Minerals Information Center. Official resource.

[2]. Nielsen, R., Hemmingsen, T. H., Bonczyk, T. G., Hansen, O., Chorkendorff, I., & Vesborg, P. C. K. (2023). *Laser-Annealing and Solid-Phase Epitaxy of Selenium Thin-Film Solar Cells*. arXiv preprint, arXiv:2306.11311. Preprint.

[3]. Zha, G., Wang, Y., Cheng, M., Huang, D., Jiang, W., Xu, B., & Yang, B. (2020). Purification of crude selenium by vacuum distillation and analysis. *Journal of Materials Research and Technology, 9*(3), 2926–2933. https://doi.org/10.1016/j.jmrt.2020.01.043.

[4]. He, B., Wang, W., Jiang, W., Xu, B., & Yang, H. (2023). Removing of Fe, Pb and Hg from crude selenium by fractional crystallization. *Metals, 13*(4), 739. https://doi.org/10.3390/met13040739.

[5]. Zhang, H., Zhu, S., Shang, S., Dong, J., Tian, S., Zhang, T., Dong, Z., Hu, J., & Shi, Y. (2024). Preparing 5N selenium from crude selenium using a simple oxidation–atmospheric sublimation–dissolution–reduction method. *Journal of Sustainable Metallurgy, 10*, 2657–2667. https://doi.org/10.1007/s40831-024-00960-w.

[6]. Volodin, V., et al. (2025). Purification of the selenium vapor phase from droplet suspensions in vacuum distillation refining. *Processes, 13*(8), 2397. https://doi.org/10.3390/pr13082397.

[7]. Burger, A., Henderson, D. O., Morgan, S. H., Feng, J., & Silberman, E. (1990). Purification of selenium by zone refining. *Journal of Crystal Growth, 106*(1), 34–37. https://doi.org/10.1016/0022-0248(90)90283-Q

[8]. Мирзавалиев Достонбек Баходир Угли, Парманов Сарвар Тошпутович, Улугов Голибжон Давлатович ПЕРЕРАБОТКА ВОЛЬФРАМСОДЕРЖАЩИХ ОТХОДОВ И ПОЛУЧЕНИЕ РАСТВОРА ВОЛЬФРАМАТА НАТРИЯ // Universum: технические науки. 2023. №10-2 (115). URL: https://cyberleninka.ru/article/n/pererabotka-volframsoderzhaschih-othodov-i-poluchenie-rastvora-volframata-natriya (дата обращения: 19.07.2026).

[9]. Mizavaliyev D., Karshiboyev S. THE MAIN PROBLEMS OF OBTAINING HIGHPURE SELENIUM IN THE INDUSTRY AND WAYS TO SOLVE THEM //Innovations in Technology and Science Education. – 2023. – Т. 2. – №. 9. – С. 106-113.

[10]. THE TECHNOLOGY OF OBTAINING POWDERS USED IN THE PRODUCTION OF SOLID ALLOYS // S. Parmonov, K. Sharipov, D. Mirzavaliyev, et al., New Mater., Compd. Appl. 8, 450–458 (2024). https://doi.org/10.62476/nmca83450

UDC: 622.765

COMPARATIVE ASSESSMENT OF TECHNOLOGIES FOR THICKENING GOLD-BEARING FLOTATION CONCENTRATES AND RECOVERING CLARIFIED PROCESS WATER: A LITERATURE REVIEW

Omonov Ahmat Sherali ugli
Specialist of the Office of Academic Affairs, Almalyk state technical institute
omonovahmad77@gmail.com
Parmonov Sarvar Toshpulatovich
Professor (DSc), Vice-Rector for Research and Innovation, Almalyk state technical institute
Ubaydullaev Mamasidik Makhammatsolievich
Associate Professor, Namangan State Technical University
Silverstar-14@mail.ru

Annotatsiya. Ushbu maqolada oltin saqlovchi flotatsion konsentratlarni quyultirish va tiniqlashtirilgan texnologik suvni qayta olish usullari ilmiy adabiyotlar asosida qiyosiy tahlil qilingan. An’anaviy va yuqori unumdorlikdagi quyultirish, flokulyatsiya sharoitlarini hamda ta’minlash kamerasining gidrodinamikasini optimallashtirish, cho‘kma qatlamini zichlashtirish, lamelli tiniqlashtirish va superabsorbent polimerlar yordamida suvsizlantirish yondashuvlari ko‘rib chiqilgan. Texnologiyalar quyi mahsulotdagi qattiq faza miqdori, qimmatli zarrachalarni ushlab qolish, suvni qayta olish darajasi, quyilma tiniqligi, reagent sarfi va keyingi texnologik jarayonlarga muvofiqligi bo‘yicha baholangan. Oltin qayta ishlash mahsulotlarida olingan natijalar boshqa mineral suspenziyalar bo‘yicha tadqiqotlardan ajratilgan hamda ularni amaliyotga tatbiq etish chegaralari muhokama qilingan. Adabiyotlar tahlili texnologiyani faqat cho‘kish tezligi yoki quyi mahsulot zichligiga asoslanib tanlash yetarli emasligini ko‘rsatadi. Samarali yechimni aniqlash uchun mineralogik tarkib, zarrachalar yirikligi, suv kimyosi, pulpa reologiyasi va oltinning oqimlar bo‘yicha taqsimlanishini kompleks baholash zarur. Tiniqlashtirilgan suvning qayta foydalanishga yaroqliligini texnologik sinovlar bilan tasdiqlash hamda tanlangan usullarni bir xil xomashyo asosida uzluksiz rejimda taqqoslash tavsiya etilgan.

Kalit so‘zlar: *oltin saqlovchi flotatsion konsentrat; quyultirish; flokulyatsiya; qattiq–suyuq fazalarni ajratish; tiniqlashtirilgan texnologik suv; lamelli tiniqlashtirish; superabsorbent polimerlar; pulpa reologiyasi; suvni qayta ishlatish; adabiyotlar tahlili*

Аннотация. В статье представлен сравнительный анализ технологий сгущения золотосодержащих флотационных концентратов и извлечения осветлённой технологической воды на основе научной литературы. Рассмотрены традиционное и высокопроизводительное сгущение, оптимизация условий флокуляции и гидродинамики питающей камеры, уплотнение слоя осадка, тонкослойное осветление и обезвоживание с применением суперабсорбирующих полимеров. Технологии оценены по содержанию твёрдой фазы в сгущённом продукте, удержанию ценных частиц, степени извлечения воды, прозрачности слива, расходу реагентов и совместимости с последующими технологическими операциями. Результаты, полученные непосредственно на продуктах переработки золотосодержащего сырья, отделены от данных по другим минеральным суспензиям; обсуждены ограничения их переноса в промышленные условия. Анализ литературы показывает, что выбор технологии исключительно по скорости осаждения или плотности сгущённого продукта недостаточно обоснован. Для определения эффективной схемы необходима комплексная оценка минерального состава, распределения частиц по крупности, химического состава воды, реологических свойств пульпы и распределения золота между технологическими потоками. Рекомендованы проверка пригодности осветлённой воды для повторного использования посредством технологических испытаний и сравнение альтернативных методов на одинаковом исходном материале в непрерывном режиме. Представленный анализ формирует основу для выбора решений, сочетающих извлечение концентрата с эффективным управлением оборотной водой.

Ключевые слова: *золотосодержащий флотационный концентрат; сгущение; флокуляция; разделение твёрдой и жидкой фаз; осветлённая технологическая вода; тонкослойное осветление; суперабсорбирующие полимеры; реология пульпы; повторное использование воды.*

Abstract. This article presents a comparative literature review of technologies for thickening gold-bearing flotation concentrates and recovering clarified process water. The approaches examined include conventional and high-rate thickening, optimisation of flocculation conditions and feedwell hydrodynamics, sediment-bed consolidation, lamella clarification, and superabsorbent-polymer-assisted dewatering. Technologies are assessed in terms of underflow solids concentration, valuable-particle retention, water recovery, overflow clarity, reagent consumption, and compatibility with downstream processing. Findings obtained directly from gold-processing materials are distinguished from evidence concerning other mineral suspensions, and the limitations of transferring these results to industrial applications are discussed. The review indicates that settling velocity or underflow density alone cannot provide a sufficient basis for technology selection. Identifying

an effective treatment configuration requires an integrated assessment of mineralogy, particle-size distribution, water chemistry, slurry rheology, and gold partitioning between process streams. Clarified-water suitability for reuse should be verified through process-specific testing, while alternative separation methods should be compared using the same feed material under continuous operating conditions. The analysis provides a basis for selecting and validating separation arrangements that combine concentrate recovery with effective process-water management.

Key words: gold-bearing flotation concentrate; thickening; flocculation; solid–liquid separation; clarified process water; lamella clarification; superabsorbent polymers; slurry rheology; water reuse; literature review.

Introduction

Solid–liquid separation connects mineral concentration, downstream extraction, and process-water management. In gold-processing circuits, thickening must produce a concentrate suitable for subsequent treatment while limiting the transfer of valuable fine particles into the overflow. Industrial thickener development has therefore addressed both solids concentration and water clarification through improvements in equipment configuration, flocculation, and process control. FLS, Thickeners and Water Stewardship.

The separation behaviour of gold-bearing flotation concentrates can be particularly challenging. Joseph-Soly et al. (2020), investigating refractory gold-processing slurries, described a circuit in which flotation concentrate was thickened from approximately 30 to 50 wt.% solids before storage and bio-oxidation. Conventional settling of the investigated fine slurries was associated with slow separation and insufficient supernatant clarity. These observations illustrate the importance of evaluating dewatering performance for the actual material and processing stage.

An assessment based exclusively on underflow solids concentration provides an incomplete description of process efficiency. A useful comparison must also consider overflow quality, solids capture, water recovery, reagent demand, slurry handling, and compatibility with downstream operations. Increasing the concentration of a valuable product is beneficial only if the resulting stream remains suitable for transport and treatment and if solids losses remain acceptable.

This article presents a focused narrative review of conventional and enhanced thickening, feedwell optimisation, inclined-plate clarification, and superabsorbent-assisted dewatering. It distinguishes evidence obtained directly from gold-processing materials from findings established in other mineral or sediment systems. Its purpose is to identify the conditions under which each approach may be useful and to establish a defensible basis for comparative testing.

Research Methodology

1. Review scope and assessment approach

The review draws on selected experimental publications, a primary research thesis, and manufacturer technical information. Searches addressed gold-concentrate dewatering, thickener feedwell design, sediment-bed drainage, lamella clarification, and

process-water recycling. The work is a narrative synthesis rather than a systematic review or statistical meta-analysis.

The reviewed technologies do not all perform the same function. Some principally increase solids concentration; others improve clarification or recover water through a different separation mechanism. Consequently, their reported efficiencies cannot be ranked without considering feed characteristics, operating conditions, and measurement definitions.

The comparison uses five criteria: concentration of the recovered solids, retention of valuable particles, quality and quantity of recovered water, operational requirements, and strength of the supporting evidence. Where direct trials on gold-bearing flotation concentrate are unavailable, the proposed application is identified as an engineering inference requiring verification.

2. Settling behaviour and the distinction between thickening and clarification

Particle settling provides the physical basis of gravity separation. Under dilute conditions, the terminal velocity of an isolated spherical particle in the Stokes regime is expressed as:

$$v_s = (\rho_s - \rho_l) g d^2 / 18\mu$$

where v_s is settling velocity, ρ_s and ρ_l are particle and liquid densities, ρ_l is particle diameter, g is gravitational acceleration, and μ is liquid viscosity. The relationship explains the strong influence of particle size on settling. Its direct application to concentrated, irregular, or flocculated suspensions is limited by the assumptions of isolated particles and creeping flow.

Thickening and clarification should therefore be assessed as related but distinct objectives. The former concerns the concentrated underflow; the latter concerns particles remaining in the overflow. A rapidly moving settling interface does not, by itself, establish that fine particles have been captured effectively. Feedwell modelling has demonstrated that large aggregates can coexist with inadequate fines capture when portions of the feed receive insufficient contact with flocculant.

For gold-bearing material, this distinction creates an additional analytical requirement: overflow solids should be assayed for gold. Their economic significance cannot be inferred from water appearance or suspended-solids concentration alone.

Analysis and Results

3. Conventional and high-rate thickening

Conventional gravity thickeners provide a baseline against which enhanced processes can be assessed. High-rate systems combine effective aggregation with equipment designed to accommodate increased throughput per unit area. Their development reflects the integration of chemical conditioning and improved hydraulic design. Conventional equipment may also employ flocculants; reagent use alone does not define the distinction between thickener categories. FLS, Thickeners and Water Stewardship.

For a specific concentrate, the relevant question is whether an enhanced design can meet both underflow and overflow requirements under variable feed conditions. A nominally higher processing capacity should not be interpreted as superior overall

performance if it increases valuable-solids carryover or produces unstable discharge conditions.

Comparative trials should therefore maintain a common feed and report dry-solids throughput, overflow solids, underflow concentration, and reagent consumption together. This approach avoids favouring equipment merely because its performance was measured under less demanding conditions.

4. Flocculation and feedwell optimisation

Nguyen et al. (2012) developed a coupled population-balance and computational-fluid-dynamics model to examine thickener feedwell performance. Their design separated the functions of incoming-stream energy dissipation and flocculation, allowing aggregate formation to occur before discharge into a lower-shear environment. A full-scale installation in platinum processing provided evidence of improved operating stability, although changing feed conditions complicated quantitative attribution of the benefits.

The implication for gold-concentrate treatment is that reagent selection and hydraulic conditions should be investigated jointly. A comparison of flocculants under one mixing condition may not identify the most effective combination for another feedwell.

A proposed test programme should vary polymer type, dosage, dilution, addition point, and mixing intensity while measuring settling, overflow solids, and sediment consolidation. The preferred condition should satisfy the complete separation objective rather than maximise a single response.

5. Enhanced bed drainage and dense-underflow production

Research on tailings provides evidence that sediment-bed behaviour can be modified mechanically. Chen et al. (2020) investigated pore connectivity during deep-cone thickening using continuous tests and computed tomography. At a feed concentration of 10 wt.% solids, the reported underflow concentrations reached 58.5 wt.% with shear and 55.8 wt.% without shear under the tested conditions. The study associated drainage behaviour with changes in the pore network.

These results support investigating bed drainage when initial settling is satisfactory but final concentration remains inadequate. They do not establish a corresponding concentration increase for gold-bearing flotation concentrate: the experimental material was tailings.

For concentrate applications, enhanced compression should be evaluated alongside rheological measurements and the solids requirement of the next operation. Producing the densest possible underflow is not necessarily an appropriate objective if additional dilution is subsequently required or if transport becomes more demanding. This is a process-design inference, not a performance result demonstrated for the concentrate considered here.

6. Inclined-plate clarification

Lamella settlers increase the available settling surface and shorten the distance particles travel before collection. Liu et al. (2020) tested synthetic sediment suspensions at 500, 1,000, and 5,000 mg/L. Their experimental programme demonstrated that settling distance, residence time, and feed characteristics influenced turbidity reduction.

This evidence supports considering inclined plates for clarification, but the tested suspensions were not gold concentrates. A reasonable application to investigate is treatment of a relatively dilute overflow requiring additional solids removal. Direct use on concentrated flotation slurry requires separate assessment of solids loading, flow distribution, and sediment removal.

The comparison should also distinguish clarification from bulk dewatering. A unit that produces a clearer liquid may still require a separate arrangement for concentrating and recovering the captured solids.

7. Superabsorbent-assisted dewatering

Joseph-Soly et al. (2020) directly investigated superabsorbent polymers using refractory gold flotation concentrate, bio-oxidation product, and cyanide-leach residue. The polymers absorbed more than 94 wt.% of water from dilute slurries within 30 minutes. After 60 minutes, the authors reported 45–76 wt.% more recovered water than with gravity settling under their experimental conditions.

The distinction between water absorption and recovery of reusable liquid is important. An industrial comparison must include polymer separation, regeneration, water release, and repeated reuse. The reported laboratory improvement should not be treated as proof of superiority over an optimised continuous flocculant-assisted thickener.

8. Clarified-water suitability for reuse

Water-recycling performance must be tested within the intended circuit. Björkqvist (2017) conducted ten consecutive flotation cycles using pyrite-bearing tailings and reused water from the preceding experiment. Grade and recovery remained broadly stable for the tested material despite the accumulation of chemical species. This primary study demonstrates that recycling need not impair flotation under all conditions, while its material-specific results cannot establish universal compatibility.

Accordingly, this review proposes defining recovered-water quality through both physical and process-response measurements. Suspended solids and turbidity should be accompanied by water-chemistry measurements relevant to the plant and by flotation or downstream-treatment tests using the recovered liquid.

“Clarified process water” is therefore the appropriate description for a low-solids overflow. The expression does not imply that dissolved substances have been removed or that the water is suitable for every use.

9. Research needs

The selected literature does not provide a controlled comparison of all reviewed technologies on the same gold-bearing flotation concentrate. This prevents a defensible numerical ranking.

Future work should use representative concentrate samples and actual process water, include feed variability, and progress from batch screening to continuous operation. Measurements should cover gold distribution, water recovery, overflow solids, underflow rheology, reagent consumption, and downstream performance.

Economic assessment should use a common functional basis, such as cost per tonne of dry concentrate treated while satisfying defined solids-recovery and water-quality requirements. For emerging processes, all auxiliary stages should be included in that boundary.

10. Comparative synthesis

Table 1 presents an interpretive comparison of the reviewed approaches. The suggested applications are candidates for testing, rather than a universal equipment ranking.

Table 1. Comparative assessment of separation approaches

Approach	Principal objective	Evidence considered	Priority in concentrate-specific testing
Conventional thickening	Bulk water removal and solids concentration	Established industrial practice	Baseline solids capture and concentration
High-rate thickening	Increased processing capacity	Industrial technical documentation	Throughput at acceptable overflow quality
Feedwell optimisation	Effective conditioning and controlled discharge	Modelling and platinum-plant application	Fines capture under changing feed conditions
Enhanced bed drainage	Greater sediment consolidation	Experimental tailings research	Underflow concentration and handling
Lamella clarification	Additional suspended-solids removal	Synthetic-sediment experiments	Overflow treatment and solids withdrawal

Conclusion and Recommendations

The reviewed evidence supports treating gold-concentrate thickening as a combined problem of solids recovery, sediment concentration, and process-water management. No single reported indicator is sufficient to establish technological superiority.

Conventional and high-rate thickening provide practical reference cases. Feedwell optimisation addresses conditioning and flow distribution, while enhanced bed drainage targets consolidation. Inclined plates are a candidate for supplementary clarification, and superabsorbent polymers have shown promising results directly on gold-processing slurries.

The principal limitation is the absence, within the selected literature, of comparable continuous trials using the same concentrate. Technology selection should therefore rely on material-specific testing and complete process balances. The most effective arrangement will be the one that retains valuable particles, produces a usable underflow, and recovers water compatible with the receiving process at an acceptable overall cost.

References

[1]. Joseph-Soly, S., Asamoah, R. K., Skinner, W., & Addai-Mensah, J. (2020). Superabsorbent dewatering of refractory gold concentrate slurries. Advanced Powder Technology, 31(8), 3168–3176. https://doi.org/10.1016/j.apt.2020.06.010.

[2]. Nguyen, T. V., Farrow, J. B., Smith, J., & Fawell, P. D. (2012). Design and development of a novel thickener feedwell using computational fluid dynamics. Journal of the Southern African Institute of Mining and Metallurgy, 112(11), 939–948. Full text.

[3]. Chen, X., Jin, X., Jiao, H., Yang, Y., & Liu, J. (2020). Pore connectivity and dewatering mechanism of tailings bed in raking deep-cone thickener process. Minerals, 10(4), 375. https://doi.org/10.3390/min10040375.

[4]. Liu, L., Perez, M. A., & Whitman, J. B. (2020). Evaluation of lamella settlers for treating suspended sediment. Water, 12(10), 2705. https://doi.org/10.3390/w12102705.

[5]. Björkqvist, A. (2017). Water recycling in flotation [Master's thesis, Aalto University]. Institutional repository.

[6]. FLS. (n.d.). Thickeners—Water stewardship. Manufacturer technical information. Accessed September 14, 2026. Technical webpage.

[7]. Мирзавалиев Достонбек Баходир Угли, Парманов Сарвар Тошпутович, Улугов Голибжон Давлатович Переработка Вольфрамсодержащих Отходов И Получение Раствора Вольфрамата Натрия // Universum: технические науки. 2023. №10-2 (115). URL: https://cyberleninka.ru/article/n/pererabotka-volframsoderzhaschih-othodov-i-poluchenie-rastvora-volframata-natriya (дата обращения: 19.07.2026).

[8]. Mizavaliyev D., Karshiboyev S. The Main Problems Of Obtaining Highpure Selenium In The Industry And Ways To Solve Them //Innovations in Technology and Science Education. – 2023. – Т. 2. – №. 9. – С. 106-113.

Section 3. ACTUAL PROBLEMS OF HISTORY, PHILOSOPHY AND SOCIOLOGY

THE PHILOSOPHY OF INTELLECTUALISM: A PHILOSOPHICAL INTERPRETATION OF REASON, KNOWLEDGE AND HUMAN PERFECTION

Rakhimov Gayrat Buvakhanovich
Doctor of Philosophy (PhD) in Pedagogical Sciences, Acting Associate Professor,
Vice-Rector for Academic Affairs, Urgench State University named after Abu Rayhon Beruniy
gayratraximov941@gmail.com

Annotatsiya. Maqolada intellektualizm insonning borliqni anglashida aql va bilimga bosh o‘rin beruvchi falsafiy pozitsiya sifatida talqin qilinib, uning shakllanishi, tushunchaviy tuzilishi va bugungi ahamiyati ko‘rib chiqiladi. Muammo shunday vaziyatda qo‘yiladiki, bunda bilishga to‘sqinlik qiluvchi omil axborot tanqisligi emas, uning haddan ziyodligidir; shu sababli falsafiy jihatdan inson qancha bilishi emas, bilimni qanday o‘zlashtirishi, tekshirishi va qo‘llashi muhim. Tadqiqot Aflotun, Arastu, Forobiy, Ibn Sino, Dekart, Leybnits, Kant va Popper asarlariga tayanadi; tarixiy-falsafiy rekonstruksiya, qiyosiy tahlil, tushunchalarni farqlash va germenevtik talqin usullaridan foydalaniladi. Tadqiqotda aniqlandiki, intellektualizm bilimdonlikka tenglashmaydi: uni bilimni ongli o‘zlashtirish, asosini esa talab qilish, tanqidiy tekshirish va xulosalarni qayta ko‘rib chiqishga tayyorlik tashkil etadi.

Kalit so‘zlar: *intellektualizm, intellekt, aql, tafakkur, bilim, haqiqat, ratsionalizm, tanqidiy tafakkur, refleksiya, intellektual madaniyat, erkinlik, mas’uliyat, inson kamoloti.*

Аннотация. В статье интеллектуализм рассматривается как философская позиция, отводящая разуму и знанию главное место в постижении человеком бытия; прослеживаются его становление, понятийная структура и современное значение. Проблема ставится в ситуации, когда познание затруднено не нехваткой, а избытком информации, ввиду чего философски значимо не то, сколько человек знает, а то, как он усваивает, проверяет и применяет знание. Исследование опирается на тексты Платона, Аристотеля, Фараби, Ибн Сины, Декарта, Лейбница, Канта и Поппера и использует историко-философскую реконструкцию, сравнительный анализ, понятийное разграничение и герменевтическую интерпретацию. Установлено, что интеллектуализм не сводится к эрудиции: его образуют осознанное усвоение знания, требование оснований, критическая проверка и готовность пересматривать выводы.

Ключевые слова: *интеллектуализм, интеллект, разум, мышление, знание, истина, рационализм, критическое мышление, рефлексия, интеллектуальная культура, свобода, ответственность, совершенство человека.*

Abstract. The article interprets intellectualism as a philosophical position that gives reason and knowledge the leading place in the human comprehension of

being, and traces its formation, its conceptual structure and its present-day meaning. The problem is posed in a situation where cognition suffers from the excess of information rather than its scarcity, so that what matters philosophically is not how much a person knows but how knowledge is appropriated, examined and used. The study draws on the primary texts of Plato, Aristotle, al-Farabi, Ibn Sina, Descartes, Leibniz, Kant and Popper, using historical-philosophical reconstruction, comparative analysis, conceptual delimitation and hermeneutic interpretation. It is established that intellectualism is not erudition: it consists in the conscious assimilation of knowledge, the demand for grounds, critical examination and readiness to revise conclusions.

Key words: *intellectualism, intellect, reason, thinking, knowledge, truth, rationalism, critical thinking, reflection, intellectual culture, freedom, responsibility, human perfection.*

Introduction

Reason and knowledge have long been regarded as the capacities through which the human being secures a place in nature and in society. The boundary separating humanity from the rest of the living world has rarely been drawn along biological lines alone; it has been sought in the ability to make reality an object of deliberate study, to look for the causes standing behind events, to plan beyond the immediate situation and to pass accumulated experience on in symbolic form. Each of these capacities presupposes an intellectual relation to the world, one in which what is given is not simply undergone but interpreted and reconstructed in thought. Intellect therefore belongs to the fundamental problems of philosophy, and not to psychology alone.

Intellectualism names the philosophical recognition of the primacy of reason and knowledge in this process. Everyday usage narrows the word to erudition or to a large stock of retained information, and in doing so replaces a qualitative criterion with a quantitative one.

Taken philosophically, the position concerns the manner in which knowledge is appropriated: consciously rather than mechanically, with an account of grounds rather than by deference to authority, and with a real openness to conclusions that were not prescribed in advance. The urgency of the question has grown with the changed informational conditions of contemporary life. What once required years of search is now obtained in seconds, while the labour of verification has become harder and is often abandoned altogether; contradictory assertions circulate side by side, the line between an argued judgement and an unsupported opinion is blurred, and much cognitive work is delegated to systems whose criteria of selection remain invisible. The shortage of information has ceased to be the principal difficulty. The difficulty is the inability to distinguish the reliable from the merely plausible, to grasp what an assertion actually claims and to reach a conclusion that can be defended before others.

The aim of this article is to disclose the philosophical essence of intellectualism, to reconstruct the main stages of its formation in Eastern and Western thought, and to determine what it means today. Four tasks follow: to clarify the conceptual content of intellect; to trace the emergence of the intellectualist principle in antiquity, its development in the East and its transformation in Modern rationalism; to delimit

knowledge, thinking and intellect from one another; and to interpret the position through critical thinking, freedom, culture and responsibility. Its novelty lies in reading intellectualism as a unity of cognitive and moral dimensions, in which the Eastern and Western traditions appear as complementary rather than opposed.

Materials and Methods

The study works with primary texts that pose the relation between reason, knowledge and human perfection directly: the *Apology* and the *Republic* of Plato and the *Nicomachean Ethics* of Aristotle; the treatise of Abu Nasr al-Farabi on the virtuous city, the *Metaphysics of the Healing* of Ibn Sina and the scholarly legacy of Abu Rayhon Beruniy; the *Meditations on First Philosophy* of René Descartes and the *Philosophical Essays* of Leibniz; Kant's answer to the question of enlightenment and Popper's *Conjectures and Refutations*. Each of them states explicitly what reason is held to be capable of and what a conviction must satisfy in order to count as knowledge.

Four procedures are combined. Historical-philosophical reconstruction restores the order in which the intellectualist principle took shape, so that it appears as a developing position rather than a series of unconnected opinions. The comparative method sets the Eastern and Western readings of reason side by side and brings out both their common core and the difference in the horizon within which each places knowledge. Conceptual and logical analysis is applied wherever knowledge, thinking and intellect must be told apart, since much of the confusion surrounding intellectualism arises from substituting one of these for another; the sources themselves are read hermeneutically, with attention to the problem that gave rise to each text. Historicism and objectivity are observed throughout.

The argument moves in three stages: from the concepts to their history, and from their history to their present significance.

Results

1. The conceptual content of intellect and intellectualism

The term "intellect" derives from the Latin *intellectus* – apprehension, perception, and understanding. Even in its original semantic field the word denotes the act of grasping rather than the storing of what has been received. Philosophically, intellect signifies the capacity to master reality through concepts: to isolate what is essential in a phenomenon, to break a problem into its components, to establish dependencies between events and to reach conclusions that go beyond the given. Intellectualism took shape as the position acknowledging the special significance of reason in human activity, and its central thesis can be put in a single proposition: reality is in principle intelligible, and reason is a reliable, though not infallible, instrument of its disclosure.

Identifying intellectual activity with the accumulation of knowledge is nevertheless an error, and a persistent one. Someone may retain hundreds of facts and still be unable to establish the relations between them, to say which is cause and which consequence, or to derive from what is known a proposition not stated before; however impressive the store, this falls short of developed thinking. What is decisive is not the quantity of information but the operations to which it is subjected – analysis and synthesis, comparison, generalisation, abstraction, argumentation, methodical doubt, inference. Intellect is precisely the system of capacities that allows these operations to

be performed, and its growth is measured by the difficulty of the tasks a person can resolve.

From this follows a further trait. A person of developed intellect does not take ready-made judgments on trust: he looks for the ground on which a claim rests, distinguishes what has been demonstrated from what has merely been asserted, and is prepared to reconsider his own view when new knowledge requires it. Such readiness is not instability but its opposite, since it presupposes a commitment to truth stronger than attachment to one's earlier formulations.

2. The formation of the intellectualist principle in ancient philosophy

The earliest roots of the position lie in ancient Greek thought, where the essence of being was first explained outside the framework of myth. That transition involved more than a change of vocabulary: it required that an explanation justify itself before those who heard it, and that the authority of tradition give way to the force of an argument. Reason thereby acquired the standing of an independent instrument of cognition.

Socrates insisted on a firm connection between knowledge and moral perfection, holding that a person matures spiritually through self-knowledge and that wrongdoing is inseparable from a defective understanding of the good. His method of question and answer was never meant to hand a finished truth from teacher to pupil; it was designed to bring the interlocutor nearer to a truth that no one can receive ready-made.[1] Two ideas established here would remain with intellectualism throughout its history. Understanding cannot be delegated. Moreover, the admission of one's own ignorance, far from being a defeat, is the condition under which inquiry can begin at all.

Plato gave this insight a systematic epistemological form, distinguishing knowledge from opinion and separating the changeable things given to the senses from the essence apprehended by reason. In the allegory of the cave the prisoner who turns towards the light undergoes not an addition to what he already possessed but a reorientation of his whole way of seeing.[2] Intellectual development is thus a transformation of the person rather than an enlargement of his store of information. Aristotle analyzed the same domain more systematically and created the instruments by which reasoning could be examined in its own right: his logical writings founded the study of concept, judgment and inference, and established what a demonstration must satisfy if it is to count as knowledge rather than persuasion. In his ethics, rational activity stands among the highest human possibilities, and the intellectual virtues prove indispensable to the perfection of character, since practical wisdom governs the choice of means and ends in a life that can be called well.[3]

Antiquity produced no intellectualism in the modern sense, and it would be an anachronism to look for one there. What it did accomplish was the elevation of the constitutive ideas – the intelligibility of being, the requirement of argument, knowledge as achievement rather than transfer, the bond between cognitive and moral perfection – to the centre of philosophical attention.

---

[1]Plato. *Apology*. In: Plato. *Complete Works* / Ed. J. M. Cooper. Indianapolis: Hackett Publishing, 1997. P. 17–36.

[2]Plato. *Republic*. Trans. G. M. A. Grube, rev. C. D. C. Reeve. Indianapolis: Hackett Publishing, 1992. Book VII, 514a–521b.

[3]Aristotle. *Nicomachean Ethics*. Trans. T. Irwin. Indianapolis: Hackett Publishing, 1999. Book VI, pp. 87–106.

3. Reason, knowledge and perfection in the philosophical thought of the East

A history of intellectualism confined to Western philosophy would be seriously incomplete. The thinkers of the East did not merely preserve the Greek heritage; they interpreted it, criticized it and set it within a horizon in which the theory of knowledge was never separated from the doctrine of the good life.

In the philosophy of Abu Nasr al-Farabi reason appears among the capacities that determine the essence of the human being, and genuine happiness is bound to the joint operation of knowledge, virtue and reasonable activity. In his account of the virtuous society, the educated and spiritually mature person is a condition of social progress, so that the perfection of the individual and that of the community form a single task.[4] He does not reduce the development of reason to the gathering of information: knowledge is to serve the perfection of the self and activity beneficial to others, and it therefore never stands apart from the moral virtues. The move is philosophically consequential, for it blocks in advance the reading of intellectualism as a technical competence indifferent to its ends. Reason severed from virtue remains an instrument without direction.

Cognition occupies a comparable place in the philosophy of Abu Ali ibn Sina, who describes knowing as a graded process advancing from sensation towards rational generalisation. Particular objects reach us through the senses, but what they have in common cannot itself be sensed: the universal is grasped by the intellect, which abstracts the essential from the accidental.[5] Knowledge in the proper sense is thus shown to be an active work of the mind, not a passive registration of impressions.

Abu Rayhon Beruniy contributed a rigorous methodological ethos to the same tradition. In his study of peoples, natural phenomena and scientific problems the first place belongs to observation, comparison and experience, and the conclusion must follow from what has been established rather than from what the scholar would prefer to be true. His practice of presenting the beliefs of other communities accurately, in the terms in which they understood themselves, before proceeding to evaluation, is an early and remarkably consistent form of intellectual honesty. What distinguishes the Eastern contribution, taken as a whole, is the harmony of reason and knowledge with spiritual maturity. Where the exercise of reason is itself open to ethical assessment, intellectualism becomes the capacity to direct acquired knowledge towards worthy ends – a point of immediate relevance today, when considerable intellectual resources serve aims that will not withstand moral scrutiny.

4. Reason in the rationalism of the Modern era

In Modern philosophy, the standing of reason rose further, driven as much by the practice of the new sciences as by argument. Nature proved describable in exact terms, hypotheses could be tested by experiment, and received authority could be overturned by evidence available to any competent observer. Philosophy answered by placing the knowing subject, rather than transmitted doctrine, at the centre of inquiry.

---

[4]Абу Наср Фаробий. *Фозил одамлар шаҳри*. Тошкент: Янги аср авлоди, 2016. 37–45-б.

[5]Ibn Sina. *The Metaphysics of The Healing*. Trans. M. E. Marmura. Provo: Brigham Young University Press, 2005. P. 1–15.

Descartes expresses this turn in its most concentrated form. Seeking knowledge on which one could genuinely rely, he converts doubt from a skeptical result into a method, suspending every conviction that admits of the least uncertainty, and finds in the act of thinking the one position that cannot be doubted without being confirmed: "I think, therefore I am" makes the thinking subject the supporting point of cognition.[6] Doubt here is not the rejection of knowledge but the road towards it, and the obligation it imposes is personal – to examine one's convictions, to abandon foundations that will not bear examination, to accept only what reason has made distinct. Spinoza develops the same conviction differently, treating the rational comprehension of reality as the condition of freedom itself: freedom consists not in release from the passions, which would be an impossible demand, but in understanding their causes and the necessity by which they work. Leibniz turned to the logical principles operative in all knowing. His principle of sufficient reason requires that every phenomenon and every judgement have a ground explaining why it is so and not otherwise, so that nothing may be accepted merely because it has been asserted with confidence.[7] The demand passes directly from metaphysics into intellectual practice as a prohibition on unfounded conclusions. Modern rationalism thereby supplied the position with its methodological apparatus, even if its confidence in the finality of rational knowledge would later have to be moderated.

5. Intellect, thinking and knowledge: a conceptual delimitation

The three notions stand close together without being identical, and much confusion in the assessment of intellectual development comes from failing to separate them. Knowledge is what a person has understood about reality and can to some degree justify – a result, fixed in propositions and available for communication. Thinking is the process by which knowledge is produced, reworked, generalised and carried to new conclusions. Intellect is the system of abilities that makes this activity possible at all.

Measuring intellectual growth by the increase of knowledge is therefore unsound. Other questions carry the weight: can a person apply what he knows in an unfamiliar situation, compare competing accounts of the same subject, detect an error in an argument presented persuasively, defend a position when it is challenged?

Memorising the definition of a philosophical theory may be a legitimate first form of knowledge. Explaining how that theory differs from its rivals, showing which problems it resolves and which it leaves open, and applying it to a contemporary question belong to another level entirely – a difference not of volume but of function, and no accumulation of the first produces the second by itself.

Knowledge, on this reading, is never a finished product; it is continually verified, enriched and thought through again. What converts information into an intellectual possession is reflection: the ability to say not only what one knows, but also how one came to know it and what would count as a reason to revise it?

---

[6]Descartes R. *Meditations on First Philosophy*. Trans. J. Cottingham. Cambridge: Cambridge University Press, 1996. P. 12–24.

[7]Leibniz G. W. *Philosophical Essays*. Ed. and trans. R. Ariew, D. Garber. Indianapolis: Hackett Publishing, 1989. P. 149–155.

Discussion

1. Critical thinking as a safeguard of the position

Critical thinking carries a weight in contemporary intellectualism that it did not have in earlier formulations, and the reason lies in the environment in which knowledge now circulates. It is not the denial of everything, nor the habit of taking the contrary side for its own sake; that disposition is merely another form of passivity, since it replaces assessment with an automatic reaction. Its work is to examine information and judgments against criteria that can themselves be defended: the consistency of the claim, the quality of the evidence, the reliability of the source, the existence of alternative explanations covering the same facts. Several qualities are needed at once – separating evidence from opinion, tracing where information came from and in whose interest it was produced, reconstructing the strongest version of an opposing view before criticising it, admitting an error without treating the admission as a personal defeat, and changing a conclusion when the evidence has changed. These are dispositions of character as much as cognitive skills, which is why intellectual culture cannot be reduced to techniques, transmitted independently of the person who is to use them.

Karl Popper placed exactly this attitude at the centre of his account of scientific growth. A theory, on his view, is not final truth but an explanation deliberately exposed to criticism and testing, and its value is tied to the seriousness of the attempts made to refute it.[8] Fallibility thereby ceases to be a defect of knowledge and becomes a condition of its development. Intellectual maturity shows itself less in the capacity to say, “I know” than in the willingness to add that one’s own view may prove mistaken — the disposition that allows a position to be corrected before its errors have done their work. In this sense, critical thinking is the protective mechanism of intellectualism: it keeps knowledge from hardening into dogma and preserves the difference between a conviction examined and a conviction inherited.

2. Intellectual freedom and the responsibility that accompanies it

Intellectual work cannot develop without freedom, since raising questions, examining received views and proposing alternatives all presuppose that such acts are permitted and that dissent as such carries no penalty. Freedom of this kind is not, however, a licence to assert anything at all without evidence, and confusing the two has done real damage to public discussion, where the language of freedom is often used to shield claims their authors never intended to defend. Genuine intellectual freedom is inseparable from responsibility: whoever advances a position owes an account of its grounds, owes a fair hearing to the views he opposes, and owes the community the refusal to circulate what he knows to be false. Kant gave this connection its classical expression when he tied enlightenment to the courage to use one’s own reason without the guidance of another, describing the immaturity from which enlightenment delivers us as self-incurred, since its cause lies not in a want of understanding but in the lack of resolution to use it; his “Sapere aude!” – dare to know – remains among the decisive formulations of intellectual independence.[9]

---

[8] Popper K. R. *Conjectures and Refutations: The Growth of Scientific Knowledge*. London: Routledge, 2002. P. 43–78.

[9] Kant I. *An Answer to the Question: What Is Enlightenment?* In: *Kant: Political Writings*. Cambridge: Cambridge University Press, 1991. P. 54–60.

An intellectually free person accepts no judgement automatically on account of the standing its author enjoys, and rejects none automatically either, since a reflexive rejection of authority is no more rational than a reflexive submission to it. The criterion lies elsewhere: in the evidence supporting a claim and in the coherence of the reasoning that defends it. Applied impartially to institutions, to specialists and to one's own convictions alike, this is what makes it an intellectual criterion rather than an expression of loyalty or resentment.

3. Intellectual culture as the social form of reason

Intellectual culture designates the qualities in which a person's relation to knowledge becomes visible to others: how knowledge is acquired, what habits govern thinking, how a discussion is conducted, and what attitude is taken to a truth that proves inconvenient. Someone possessing it knows the boundaries of his own competence and does not regard the admission of not knowing as a weakness – marking that limit is itself an achievement of knowledge. The same culture shows in the conduct of disagreement, where the aim is to clarify the question rather than to defeat the interlocutor.

Responsibility weighs most heavily on scholars, teachers, journalists, civil servants and the intelligentsia, because the judgments they express shape the worldview of many people who cannot verify them independently. An error made in these fields does not stay private: it is repeated, cited and in time treated as established, and the cost of correcting it rises at every stage. The purpose of intellectualism therefore extends beyond the rational capacities of individuals to the formation of an environment in which arguments are expected, sources are examined, errors are acknowledged without disgrace, and the authority of a claim comes from its grounds.

Conclusion and Recommendations

The philosophy of intellectualism investigates human reason, knowledge, thinking and understanding, and its development shows a continuity that crosses the boundary between traditions. Socrates joined knowledge to moral perfection and established that understanding cannot be transferred but must be achieved; Plato clarified the difference between knowledge and opinion and presented intellectual ascent as a transformation of the whole person; Aristotle created the systematic foundations of logical thought and secured a place for the intellectual virtues in the perfection of character. Al-Farabi bound the exercise of reason to virtue and to the good of the community, Ibn Sina showed that knowledge proper is produced by the intellectual work of abstraction, and Beruniy established in practice that conclusions must follow evidence rather than preference. Descartes, Spinoza and Leibniz raised the standing of rational thought to a new level, supplying methodical doubt, the ideal of self-examined foundations and the demand for sufficient grounds.

Contemporary intellectualism enriches that inheritance with critical thinking, intellectual freedom, reflection, intellectual culture and responsibility. A person of developed intellect is not simply one who knows a great deal: he analyses information rather than merely receiving it, tells evidence from opinion, justifies his views before others, acknowledges an error without counting it a loss, and reconsiders a position when new knowledge makes reconsideration necessary. These capacities do not appear of themselves as learning grows; they are formed, and forming them is among the principal

tasks of education. The contemporary essence of intellectualism may therefore be expressed through the principle of a transition from the possession of knowledge to a responsible life with knowledge. Intellectual superiority is manifested not in the quantity of information mastered, but in the ability to place knowledge at the service of truth, human dignity, spiritual maturity and the progress of society. In a culture that produces information far faster than it does produces understanding, this ability is not one intellectual quality among others; the rest keep their value under the condition.

References

[1]. Aristotle. *Nicomachean Ethics*. Trans. T. Irwin. Indianapolis: Hackett Publishing, 1999. Book VI, pp. 87–106.
[2]. Descartes R. *Meditations on First Philosophy*. Trans. J. Cottingham. Cambridge: Cambridge University Press, 1996. Pp. 12–24.
[3]. Ibn Sina. *The Metaphysics of The Healing*. Trans. M. E. Marmura. Provo: Brigham Young University Press, 2005. Pp. 1–15.
[4]. Kant I. An Answer to the Question: What Is Enlightenment? In: *Kant: Political Writings*. Cambridge: Cambridge University Press, 1991. Pp. 54–60.
[5]. Leibniz G. W. *Philosophical Essays*. Ed. and trans. R. Ariew, D. Garber. Indianapolis: Hackett Publishing, 1989. Pp. 149–155.
[6]. Plato. Apology. In: Plato. *Complete Works* / Ed. J. M. Cooper. Indianapolis: Hackett Publishing, 1997. Pp. 17–36.
[7]. Plato. *Republic*. Trans. G. M. A. Grube, rev. C. D. C. Reeve. Indianapolis: Hackett Publishing, 1992. Book VII, 514a–521b.
[8]. Popper K. R. *Conjectures and Refutations: The Growth of Scientific Knowledge*. London: Routledge, 2002. Pp. 43–78.
[9]. Абу Наср Фаробий. *Фозил одамлар шаҳри*. Тошкент: Янги аср авлоди, 2016. 37–45-б.

UDC: 070:930.85(575.144)

TRANSFORMATION OF PRINT MEDIA IN NAVOI REGION: HISTORICAL STAGES AND DEVELOPMENT TRENDS (1992-2025)

Abduraxmonov Mirsaid Muzaffarovich
Doctoral Researcher, Navoi State University
abduraxmonovmirsaid854@gmail.com

Annotatsiya. Mazkur maqolada 1992-2025-yillarda Navoiy viloyatida bosma ommaviy axborot vositalarining tarixiy transformatsiyasi tahlil qilinadi. Arxiv materiallari, mahalliy davriy nashrlar, statistik ma’lumotlar va tegishli tarixiy manbalar asosida hududiy matbuot rivojlanishining asosiy bosqichlari aniqlanadi. Bosma nashrlar soni va tirajidagi o‘zgarishlar, ularning institutsional rivojlanishi, moddiy-texnik modernizatsiyasi hamda o‘zgarib borayotgan ijtimoiy-iqtisodiy sharoitlarga moslashuviga alohida e’tibor qaratiladi. Shuningdek, raqamli texnologiyalarning mahalliy gazetalarga ta’siri va hududiy axborot muhitida bosma hamda raqamli media shakllarining bosqichma-bosqich integratsiyasi tahlil qilinadi.

Kalit so‘zlar: *bosma ommaviy axborot vositalari, Navoiy viloyati, mahalliy matbuot, hududiy gazetalar, tarixiy davrlashtirish, tiraj, institutsional rivojlanish, raqamli transformatsiya, axborot muhiti.*

Аннотация. В статье анализируется историческая трансформация печатных средств массовой информации в Навоийской области в 1992-2025 годах. На основе архивных материалов, местных периодических изданий,

статистических данных и соответствующих исторических источников определяются основные этапы развития региональной прессы. Особое внимание уделяется изменениям количества и тиражей печатных изданий, их институциональному развитию, материально-технической модернизации и адаптации к меняющимся социально-экономическим условиям. Также анализируется влияние цифровых технологий на местные газеты и постепенная интеграция печатных и цифровых форм медиа в региональное информационное пространство.

Ключевые слова: *печатные СМИ, Навоийская область, местная пресса, региональные газеты, историческая периодизация, тираж, институциональное развитие, цифровая трансформация, информационное пространство.*

Abstract. This article examines the historical transformation of print media in Navoi Region between 1992 and 2025. Drawing on archival materials, local periodicals, statistical data, and relevant historical sources, the study identifies the main stages in the development of the regional press. Particular attention is paid to changes in the number and circulation of print publications, their institutional development, material and technical modernization, and adaptation to changing socio-economic conditions. The article also analyzes the impact of digital technologies on local newspapers and highlights the gradual integration of print and digital forms of media within the regional information environment.

Key words: *print media, Navoi Region, local press, regional newspapers, historical periodization, circulation, institutional development, digital transformation, information environment.*

Introduction

During the years of independence, new legal and institutional foundations for the functioning of mass media were formed in Uzbekistan, while their role and significance in society, as well as their functions within the information space, gradually changed. Ensuring freedom of speech and the press, supporting mass media, and strengthening their participation in public oversight came to be regarded as priority areas of state policy. As President of the Republic of Uzbekistan Shavkat Mirziyoyev emphasized, Uzbek media companies are also striving to secure a worthy place in the global information space and to participate actively in global political and social processes; to achieve this, it is necessary to work continuously, master advanced foreign experience, modern information technologies and multifaceted analytical methods, remain in constant pursuit of new knowledge, and train a new generation of national journalists. The President also noted that strengthening the role and influence of mass media in creating favorable opportunities for citizens in the information sphere and exercising public oversight over the activities of state authorities and administration is another priority task [1]. This approach demonstrates the growing importance of mass media not only as a means of disseminating information but also as an institution that facilitates communication between the state and society and contributes to the formation of public opinion. Studying these processes at the local level makes it possible to identify how regional, district and city newspapers adapted to new socio-political and technological

conditions. In the twenty-first century, the large-scale development of information and communication technologies has generated major structural and technological changes in the activities of mass media. The expansion of the Internet, social networks and digital platforms has transformed the ways information is created, processed and delivered to audiences. This process has directly affected traditional print media, particularly regional newspapers. Therefore, the history of print media should not be studied solely through the number of publications or their circulation, but rather as a historical process interconnected with political-legal, socio-economic and technological changes. Despite these developments, the formation, institutional development, material and technical modernization, and adaptation of print mass media in Navoi Region to the digital information environment during 1992-2025 have not yet been sufficiently studied as an integrated historical process. Accordingly, the purpose of this study is to analyze the development dynamics of print mass media in Navoi Region on the basis of historical sources and statistical data, identify its principal stages, and reveal the specific features of the institutional and technological transformations that occurred within the regional press system.

Literature Review

From the early years of independence, new legal and institutional foundations for the functioning of mass media began to take shape in Uzbekistan. Researchers assess the formation and development of the media system during the independence period in connection with the political and legal reforms carried out in the country, efforts to ensure freedom of information, and the development of civil society [2]. In particular, A. Rasulov draws attention to the source value of mass-media materials in the study of the history of the independence period and identifies them as important historical sources reflecting political and social processes in society [3].

The changes that took place in the Uzbek press during the independence period were not limited to nationwide publications. The activities of regional, district and city newspapers also adapted to the new political, economic and informational environment. In addition to covering local socio-economic processes, such regional publications are important sources documenting the everyday life, public opinion and historical memory of particular territories. Studies conducted in other regions of Uzbekistan likewise demonstrate the need to examine the formation, development and thematic orientation of local newspapers and journals of the independence period within the framework of regional history [4].

Research Methodology

This study employed the principles of historicity, objectivity and systematic analysis to examine the formation and transformation of print mass media in Navoi Region during 1992-2025. The source base consisted of archival documents concerning the Republic of Uzbekistan and Navoi Region, normative and legal documents, official statistical data, issues of regional and district-city newspapers published in different years, and scholarly literature on the topic. In using print-media materials as historical sources, attention was paid to the period in which the information was produced, the territorial affiliation of the publication, the nature of its founding institution, and the content of the events reported.

In studying the local press, newspaper materials were treated not merely as carriers of information but as historical sources recording regional socio-political and economic processes during a particular historical period. In line with methodological approaches concerning the source potential of mass-media materials in studying the history of Uzbekistan during the independence period, materials published in “Do‘stlik bayrog‘i,” “Знамя дружбы,” and district and city newspapers were analyzed as important sources for reconstructing regional processes of the respective periods.

Another important direction of the research methodology was periodization. Alongside quantitative changes in the number of publications, the study jointly examined the political and legal environment, institutional development of publications, modernization of the material and technical base, circulation dynamics, and the penetration of digital technologies. From this perspective, the history of print mass media in Navoi Region was divided into three stages: 1992-2000, 2001-2016, and 2017-2025. This periodization was not treated as a predetermined methodological assumption but as a research result derived from a comparative analysis of historical and statistical sources. Thus, the methods employed demonstrated that changes in the history of print media cannot be adequately explained solely by increases or decreases in the number of publications. The study revealed the importance of institutional, socio-economic and technological transformations during the independence period.

Analysis and Results

The research results show that the development of print mass media in Navoi Region during 1992-2025 was not uniform; rather, it passed through distinct historical stages under the influence of political and legal, socio-economic and technological changes in the country. Comparative analysis of archival documents, periodicals and statistical indicators makes it possible to distinguish three principal stages.

The first stage: 1992-2000 - the period of formation and adaptation to new socio-political conditions. While some local newspapers established during the Soviet period continued to operate, their content, founding relations and social functions gradually changed under the influence of the new conditions. At the same time, the emergence of new sectoral and organizational publications led to the structural expansion of the print information space in Navoi Region. From the 1990s onward, a regional press system consisting of regional, district-city and sectoral publications was formed, and in subsequent periods its quantitative composition, material and technical base, circulation and methods of information dissemination underwent significant changes. For example, while 11 newspapers operated in the region in 1992-1993 [5], by 1997 there were 19 newspapers, including the two regional newspapers “Do‘stlik bayrog‘i” and “Знамя дружбы,” one city newspaper, and eight district newspapers [6].

The second stage: 2001-2016 - the period of development, institutional stabilization and material and technical modernization. An important feature of this stage was the renewal of newspaper preparation and printing technologies. The use of computer equipment, electronic page layout and modern printing equipment changed production processes in editorial offices and printing houses. At the same time, the number of newspapers continued to increase. For example, in 2004 the region had 34 newspapers and 2 journals [7], in 2011 there were 37 periodicals [8], and in 2014 there were 39 periodicals [9].

These indicators show that the formative process of the 1990s continued in the following period through relatively stable institutional development. The establishment of a “Press House” for journalists in Navoi city and the creation of a modern printing house under the state enterprise housing the editorial offices of “Do‘stlik bayrog‘i” and “Знамя дружбы” strengthened the material and technical base of the regional press. According to official information, the launch of this modern printing house in 2010 marked the beginning of a new period in the regional printing system [10]. The third stage: 2017-2025 - the period of digital transformation and adaptation to the new media environment. This stage is characterized by the active adaptation of print mass media in Navoi Region to the digital information environment. As online publications and social networks increasingly occupied an important place in information consumption, the traditional information-distribution model of newspapers began to change. Alongside preparing print issues, editorial offices started distributing materials electronically and using the Internet and social networks. As a result, the integration of print and digital media forms became evident. During the transition to a digital environment, the number of periodicals tended to decline. For example, in 2021, Navoi Region had 30 newspapers and 3 journals [11], while by 2025 their number had decreased to 19 [12]. A significant decline in the circulation of print publications was also observed. The results indicate that the reduction in the number and circulation of publications during 2017-2025 should not be interpreted solely as a crisis of the print press. Rather, during this period, information production and distribution channels became diversified, and traditional newspapers and Internet platforms began operating in parallel. Therefore, the third stage should be characterized not as a period of disappearance of the regional press in Navoi Region, but as a stage of adaptation to a new information environment based on the integration of print and digital media forms. The results of the study show that the development of print mass media in Navoi Region during 1992-2025 was closely connected with the political, economic and technological changes taking place in the country. The three identified stages demonstrate that the history of the regional press should be evaluated not only through increases or decreases in the number of publications but also in conjunction with its institutional formation, modernization of its material and technical base, and changes in the forms of information dissemination. During the first stage, the increase in the number of publications from 11 to 25 indicates that the regional information space was undergoing institutional formation in the early years of independence. At the same time that publications inherited from the Soviet period adapted to the new political and legal environment, new sectoral publications also emerged. Therefore, the quantitative growth of the 1990s should be understood not simply as the establishment of new newspapers, but as a process through which the local press adapted to a new socio-political system.

The results of the second stage show that quantitative development was accompanied by material and technical modernization. Computerization, electronic page layout and the introduction of modern printing equipment transformed the technological foundations of newspaper production. In particular, the establishment of a modern printing house in Navoi in 2010 was one of the important indicators of this process.

During the third stage, the decline in the number of print publications and in the circulation of some leading newspapers in Navoi Region occurred in parallel with a

broader nationwide trend. According to official statistical data, the number of newspapers in Uzbekistan decreased from 649 in 2010 to 366 in 2020 and to 219 in 2025 [13]. This makes it possible to interpret the process in Navoi Region not as an isolated regional phenomenon but as a regional manifestation of a broader structural transformation taking place in the Uzbek print-press system.

However, it would be incorrect to equate the decline in the number of publications and circulation with the complete loss of the social significance of the print press. The expansion of digital information consumption is changing the ways audiences obtain information. According to the National Statistics Committee of the Republic of Uzbekistan, the share of the population aged 10 and over using the Internet to read or download online newspapers, journals and electronic books is increasing. Household sample survey data from the National Statistics Committee show that the share of Internet users aged 10 and above increased from 76.6% in 2021 to 83.9% in 2022 and 89.0% in 2023 [14]. This dynamics indicates the expanding role of digital channels in the population's information environment.

These findings are also broadly consistent with international research on the digital transformation of local media. A study by the Reuters Institute based on the experience of local and regional newspapers shows that the transition to the digital environment changes not only editorial channels of information dissemination but also production processes, audience relations and economic strategies [15]. Recent studies of regional media in Uzbekistan likewise assess the transition from post-independence development to digital transformation as a distinct stage in the history of regional press. Thus, the research results demonstrate that the quantitative decline observed in the print-media system of Navoi Region after 2017 was accompanied less by institutional disappearance than by structural changes in the forms of information dissemination. While the traditional form of print publications has been preserved, the penetration of the Internet and social networks into editorial activities has led to the integration of print and digital media forms. In this respect, the experience of Navoi Region demonstrates the historical evolution of regional press during the independence period from formation to modernization and from modernization to digital transformation.

Conclusion and Recommendations

The results of the study demonstrate that the development of print mass media in Navoi Region during the independence period has been a historical process closely interconnected with political, socio-economic and technological changes. Initially, the regional press adapted to new conditions and underwent institutional formation; subsequently, its material and technical base improved, while modern printing technologies and electronic page-layout capabilities expanded. In recent years, the decline in the number of print publications and the circulation of some newspapers has been accompanied by a growing role for the Internet and social networks in editorial activities. As a result, methods of preparing and disseminating information have changed, producing greater integration between print and digital media forms. Therefore, the quantitative decline in print publications should not be interpreted solely as a crisis, but rather as a structural transformation taking place within the regional information environment. Based on the findings, the following recommendations are

proposed: (1) regional newspapers should systematically develop integrated print-and-digital distribution models so that traditional publications can maintain their historical and social functions while expanding their digital reach; (2) the material and technical modernization of regional editorial offices and printing facilities should be continued, with particular attention to digital production, online distribution and multimedia content; (3) systematic preservation and digitization of local newspaper archives should be strengthened to ensure the long-term availability of regional historical sources and support further scholarly research on the history of Navoi Region.

References

[1] Mirziyoyev Sh.M. Holiday Greeting from the President of the Republic of Uzbekistan Shavkat Mirziyoyev to Mass Media Workers. [Electronic resource]. URL: https://www.gazeta.uz/oz/2022/06/27/congratulation/
[2] Khalilova, A. Mass Media of Uzbekistan: Development from the First Years of Independence and Current Condition. International Journal of African and Asian Studies, Vol. 36, 2017.
[3] Rasulov, A.M. The Role of Mass Media in the System of Sources for the History of the Independence Period of Uzbekistan. Actual Problems of the History of Uzbekistan, 2023, pp. 633-640.
[4] Yuldosheva, Z. Classification of Newspapers and Magazines Operating in Surkhandarya During the Independence Period of Uzbekistan. Oriental Journal of Social Sciences, 5(11), 2025, pp. 357-362.
[5] National Archive of Uzbekistan, Fund M. 56, Inventory 1, Collection 20, fols. 184-192.
[6] Qambarov O. Spirituality Is the Mirror of Life // Do‘stlik Bayrog‘i, June 27, 1997.
[7] State Archive of Navoi Region, Fund M. 59, Inventory 1, Collection 230, fol. 1.
[8] Umirzakov J. Mass Media - a Window to the World of News // Znamya Druzhby, June 25, 2013.
[9] Editorial Board. Only Facts // Znamya Druzhby, June 27, 2014.
[10] Qirqinchi Bekat [The Fortieth Station]. Collection. Responsible editor: Boboqand Umarov. Tashkent, 2023, p. 7.
[11] Gulyamova D. Regional Media Space: Demand and Relevance // Znamya Druzhby, June 23, 2021.
[12] Certificate from the Navoi Regional Branch of the Union of Journalists of Uzbekistan. Date of data acquisition: July 18, 2026.
[13] National Statistics Committee of the Republic of Uzbekistan. [Electronic resource]. URL: https://siat.stat.uz/reports-filed/1021/table-data
[14] National Statistics Committee of the Republic of Uzbekistan. [Electronic resource]. URL: https://stat.uz/uz/matbuot-markazi/qo-mita-yangiliklar/52572-10-va-undan-katta-yoshlilar-orasidan-internetdan-foydalanuvchi-aholi-ulushi-oshgan?
[15] The Digital Transition of Local News. [Electronic resource]. URL: https://reutersinstitute.politics.ox.ac.uk/our-research/digital-transition-local-news

Section 4. ACTUAL PROBLEMS OF NATURAL SCIENCES

UDC: 548.73:546.56

SYNTHESIS AND SINGLE-CRYSTAL X-RAY DIFFRACTION STUDY OF A COPPER(II) COMPLEX WITH 2-AMINO-5-ETHYLTHIO-1,3,4-THIADIAZOLE AND 1,10-PHENANTHROLINE

Matmuratova Zulaykho Ikromboy qizi
Technician Laboratory Assistant, Urgench International Airport
zulayxomatmuratova1997@gmail.com
Karajanova Shakhnoza Daryabayevna
Doctaral candidate,National University of Uzbekistan
Torambetov Batirbay Smetovich
Associate Professor, Faculty of Chemistry, National University of Uzbekistan

Annotatsiya: Ushbu maqolada mis nitratning 2-amino-5-etiltio-1,3,4-tiadiazol va 1,10-fenantrolin bilan yangi monoyadroli kompleks birikmasining sintezi hamda tuzilishini o‘rganish natijalari keltirilgan. Kompleksning tuzilishi rentgen-difraksion tahlil usuli yordamida o‘rganildi. Mis(II) nitratning 2-amino-5-etiltio-1,3,4-tiadiazol va 1,10-fenantrolin molekulalari bilan buzilgan tetragonal piramidal tuzilishga ega besh koordinatsiyalangan kompleks hosil qilishi aniqlandi. Kompleksning ichki koordinatsion sferasida uchta tiadiazol ligandi va bitta 1,10-fenantrolin molekulasi markaziy mis(II) ioniga koordinatsiyalangan. Tiadiazol ligandlari endosiklik azot atomi orqali monodentat tarzda, 1,10-fenantrolin esa bidentat tarzda koordinatsiyalangan. Nitrat anionlari tashqi sferada joylashib, kation kompleks hosil qiladi.

Kalit so‘zlar: *kompleks birikma, bidentat, rentgen-difraksion tahlil, 2-amino-5-etiltio-1,3,4-tiadiazol, 1,10-fenantrolin.*

Аннотация: В данной статье представлены результаты синтеза и исследования структуры нового моноядерного комплексного соединения нитрата меди с 2-амино-5-этилтио-1,3,4-тиадиазолом и 1,10-фенантролином. Структура комплекса исследована методом рентгенодифракционного анализа. Установлено, что нитрат меди(II) образует пятикоординационный комплекс с искажённой тетрагонально-пирамидальной структурой с молекулами 2-амино-5-этилтио-1,3,4-тиадиазола и 1,10-фенантролина. Во внутренней координационной сфере комплекса к центральному иону меди(II) координированы три лиганда тиадиазола и одна молекула 1,10-фенантролина. Лиганды тиадиазола координируются монодентатно через эндоциклический атом азота, а 1,10-фенантролин - бидентатно. Нитрат-анионы располагаются во внешней сфере, образуя катионный комплекс.

Ключевые слова: *комплексное соединение, бидентатный лиганд, рентгенодифракционный анализ, 2-амино-5-этилтио-1,3,4-тиадиазол, 1,10-фенантролин.*

Annotation: This paper presents the results on the synthesis and study of the structure of a new mononuclear complex of copper nitrate with 2-amino-5-ethylthio-1,3,4-thiadiazole and 1,10-phenanthroline. Using the method X-ray

diffraction analysis, the structure of the complex was studied. It was shown that copper (II) nitrate forms a five-coordinated complex with a distorted tetragonal pyramidal structure with 2-amino-5-ethylthio-1,3,4-thiadiazole and 1,10-phenanthroline molecules, in the inner sphere of which three thiadiazole ligands and an 1,10-phenanthroline molecules are coordinated to the complexing agent; thiadiazole ligands are bonded as a monodentate through endocyclic nitrogen, the 1,10-phenanthroline is bonded as a bidentate, the nitrate anions are located in the outer sphere forming a cationic complex.

Key words: *complex, bidentate, X-ray diffraction analysis, 2-amino-5-ethylthio-1,3,4-thiadiazole, 1,10-phenanthroline.*

Introduction

Coordination compounds of 3d-metal ions with nitrogen- and sulfur-containing heterocyclic ligands represent an important area of coordination chemistry. In particular, the ability of Cu(II) ions to adopt different coordination numbers and geometries provides broad opportunities for the design and synthesis of coordination compounds with diverse structural features. 1,3,4-Thiadiazole derivatives are of particular interest because their donor centers can readily participate in coordination with metal ions and form stable metal–ligand bonds. The combination of 2-amino-5-ethylthio-1,3,4-thiadiazole and 1,10-phenanthroline is of special interest for the construction of the Cu(II) coordination environment. 1,10-Phenanthroline can act as a bidentate chelating ligand, whereas the thiadiazole derivative can coordinate through a nitrogen donor atom in a monodentate mode. Determination of the precise molecular and crystal structures of such mixed-ligand complexes is important for understanding their coordination behavior and structural characteristics. In the present work, the $CuL_3(phen)_2$ complex was synthesized and investigated by single-crystal X-ray diffraction (SC-XRD)**.** The complex crystallizes in the monoclinic crystal system with the $P2_1/c$ space group and is characterized by the crystallographic parameters a = 12.8570(4), b = 13.1208(4), c = 21.2206(7) Å, β = 98.483(3)°, V = 3540.6(2) Å^3, and Z = 4**.** The SC-XRD study provided detailed information on the molecular structure and coordination environment of the Cu(II) ion.

Literature Review

Coordination compounds of transition metals, particularly copper(II) complexes with heterocyclic ligands, represent an important area of modern coordination chemistry due to their distinctive molecular structures and diverse magnetic, catalytic, and biological properties [1,2]. Copper(II) is an essential biogenic metal ion that plays an important role in numerous biochemical processes and serves as an active center in several metalloenzymes [3]. Therefore, the synthesis of mixed-ligand copper(II) complexes and the investigation of their coordination environments and crystal structures are of considerable scientific interest. 1,3,4-Thiadiazole derivatives, particularly 2-amino-5-ethylthio-1,3,4-thiadiazole, are promising heterocyclic ligands because the nitrogen and sulfur atoms in their molecular framework provide potential donor sites for coordination to metal ions [4,5]. Previous studies have demonstrated that thiadiazole derivatives can coordinate to metal centers in monodentate, bidentate, or bridging modes, leading to the formation of both mononuclear and polynuclear

coordination compounds [6]. The coordination mode of these ligands may vary depending on the nature of the metal ion, the electronic structure of the ligand, and the surrounding coordination environment. In addition, metal complexes containing 2-amino-5-ethylthio-1,3,4-thiadiazole and structurally related ligands have been reported to exhibit antibacterial, antifungal, and other biologically relevant activities [7,8].

The incorporation of aromatic bidentate nitrogen-donor ligands, such as 1,10-phenanthroline, is of particular interest in the design of mixed-ligand coordination compounds [9]. 1,10-Phenanthroline is capable of forming a stable chelate with metal ions through its two nitrogen donor atoms. Its rigid and planar aromatic framework can also promote intermolecular interactions within the crystal lattice, including π···π stacking and C–H···π interactions [10,11]. Consequently, the presence of 1,10-phenanthroline can substantially influence both the molecular geometry and the crystal packing of coordination compounds. Single-crystal X-ray diffraction (SC-XRD) is one of the most reliable techniques for determining the molecular and crystal structures of coordination compounds [12].

This method provides accurate information on metal–ligand bond lengths, bond angles, coordination geometry, ligand coordination modes, and intermolecular interactions within the crystal lattice. In mixed-ligand copper(II) systems containing phenanthroline and thiadiazole derivatives, the Cu(II) center may exhibit square-pyramidal or distorted octahedral coordination geometries [13,14]. Hydrogen-bonding interactions, including N–H···O, N–H···S, and C–H···X contacts, as well as other weak intermolecular interactions, may play an important role in determining the three-dimensional organization and stability of the crystal structure [15].

In this context, the synthesis and structural characterization of Cu(II) complexes containing both 2-amino-5-ethylthio-1,3,4-thiadiazole and 1,10-phenanthroline are of considerable scientific interest. The aim of the present study is to synthesize a new copper(II) complex based on 2-amino-5-ethylthio-1,3,4-thiadiazole and 1,10-phenanthroline and to characterize its molecular and crystal structure in detail using single-crystal X-ray diffraction (SC-XRD).

Particular attention is given to the coordination environment of the Cu(II) center, the coordination modes of the ligands, metal–ligand geometric parameters, and intermolecular interactions responsible for the stabilization of the crystal lattice.

Research Methodology

To synthesize the $[CuL_3(phen)_2]$ complex, 2-amino-5-ethylthio-1,3,4-thiadiazole (L) ligand (0.0483 g, 0.0003 mol) was initially weighed and dissolved in 5 mL of methanol. Copper(II) nitrate (0.018 g, 0.0001 mol) was dissolved separately in 3 mL of methanol. The prepared copper(II) nitrate solution was added to the methanolic solution of the L ligand, and the reaction mixture was stirred at room temperature for 30 min. During the reaction, the color of the solution changed to clear green**.** Subsequently, 1,10-phenanthroline (phen) (0.018 g, 0.0001 mol) was dissolved in 3 mL of methanol, and the resulting solution was added dropwise to the reaction mixture. Upon addition of 1,10-phenanthroline, the color of the solution changed to dark green**.** The reaction mixture was then stirred at room temperature for an additional 30 min and subsequently left undisturbed for crystallization [16,17]. After four days, small dark-green crystals

formed from the solution. The resulting crystals were filtered, washed with methanol, and dried at room temperature. The yield of the complex was 70%**.** Reaction equation. The synthesis reaction can be represented schematically as follows:

$$Cu(NO_3)_2+3L+phen \rightarrow [CuL_3(phen)](NO_3)_2$$

L – 2-amino-5-ethylthio-1,3,4-thiadiazole; phen – o-phenanthroline (1,10-phenanthroline); $Cu(NO_3)_2$ – copper(II) nitrate.

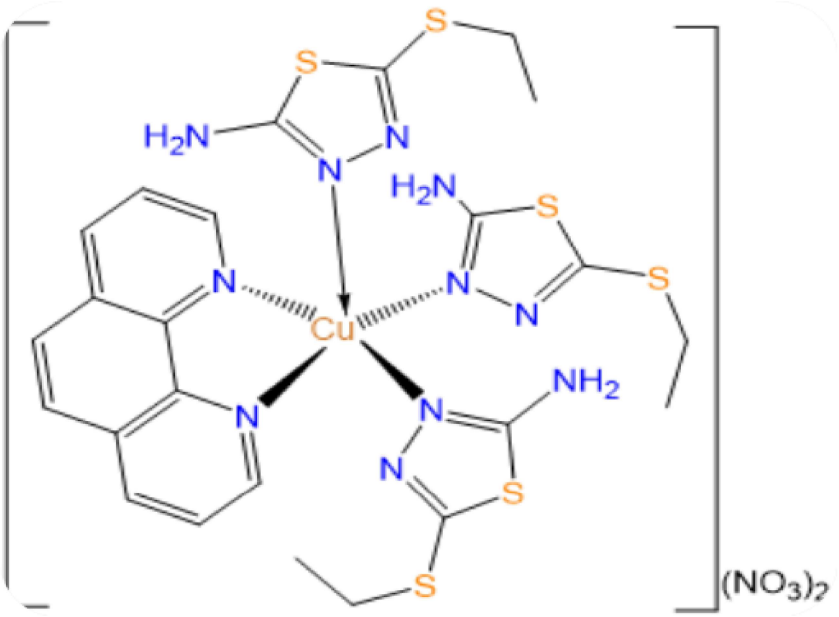

Figure 1. Crystal structure of the $[CuL_3(phen)](NO_3)_2$ complex.

Analysis and Results

To investigate the structure and properties of coordination compounds of 3d metals with thiadiazole derivatives, a new mixed-ligand $[CuL_3(phen)](NO_3)_2$ complex was synthesized. The composition and crystal structure of the synthesized complex were confirmed by elemental analysis and single-crystal X-ray diffraction (SC-XRD) analysis [18].

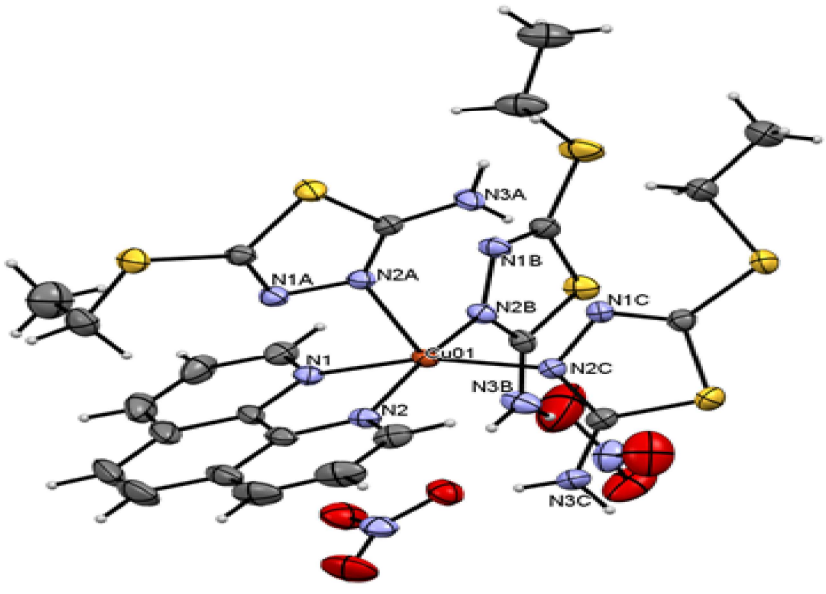

Figure 2. Structure of the $[CuL_3(phen)](NO_3)_2$ complex.

Table 1. Crystallographic data and structure refinement details for $[CuL_3(phen)](NO_3)_2$

Crystal data	
Chemical formula	$C_{24}H_{29}CuN_{11}S_6 \cdot 2(NO_3)$
M_r	851.50
Crystal system, space group	Monoclinic, $P2_1/c$
Temperature (K)	293
a, b, c (Å)	12.8570 (4), 13.1208 (4), 21.2206 (7)
β (°)	98.483 (3)
V (Å^3)	3540.6 (2)
Z	4
Radiation type	Mo $K\alpha$
μ(mm^{-1})	1.03
Crystal size (mm)	0.22;0.18;0.12
Data collection	
Diffractometer	Xcalibur, Atlas
Absorption correction	Multi-scan *CrysAlis PRO* 1.171.41.121a (Rigaku Oxford Diffraction, 2021) Empirical absorption correction using spherical harmonics, implemented in SCALE3 ABSPACK scaling algorithm.
T_{min}, T_{max}	0.907, 1.000
No. of measured, independent and observed [$I > 2\sigma(I)$] reflections	40564, 6231, 4533
R_{int}	0.053
(sin θ/λ)$_{max}$ (Å^{-1})	0.595
Refinement	
$R[F^2 > 2\sigma(F^2)]$, $wR(F^2)$, S	0.045, 0.128, 1.04
No. of reflections	6231
No. of parameters	454
H-atom treatment	H-atom parameters constrained
Δρ_{max}, Δρ_{min} (e Å^{-3})	1.06, -0.53

Table 2. Bond lengths (Å) and valence angles (°) in the crystal structure of $[CuL_3(phen)](NO_3)_2$

Bond	Bond lengths (Å)	Bond angles	Valence angles (°)
C(1)-H(1)	0.9300	C(2)-C(1)-H(1)	118.7
C(1)-C(2)	1.386 (6)	N(2)-C(1)-H(1)	118.7
C(1)-N(2)	1.329 (5)	N(2)-C(1)-C(2)	122.5 (5)
Cu(1)-N(1)	2.041 (3)	N(1)-Cu(1)-N(2A)	93.25 (12)
Cu(1)-N(2)	2.023 (3)	N(2)-Cu(1)-N(1)	81.39 (13)
Cu(1)-N(2A)	2.273 (3)	N(2)-Cu(1)-N(2A)	85.25 (11)
Cu(1)-N(2B)	2.004 (3)	N(2)-Cu(1)-N(2C)	95.02 (13)
Cu(1)-N(2C)	2.041 (3)	N(2B)-Cu(1)-N(1)	92.44 (13)
N(1)-C(10)	1.333 (5)	N(2B)-Cu(1)-N(2)	168.72 (12)
N(1)-C(12)	1.361 (5)	N(2B)-Cu(1)-N(2A)	104.62 (12)

Table 3. Hydrogen-bond geometry (Å,°) for the $[CuL_3(phen)](NO_3)_2$complex.

D-H···*A*	*D*-H	H···*A*	*D*···*A*	*D*-H···*A*
N3*A*-H3*AD*···O3^{i}	0.86	2.11	2.891 (5)	151
N3*B*-H3*BC*···O1	0.86	2.03	2.877 (5)	169
N3*B*-H3*BD*···O4	0.86	2.10	2.942 (6)	165
N3*C*-H3*CC*···O1	0.86	2.10	2.801 (5)	139
N3*C*-H3*CD*···O6^{ii}	0.86	2.02	2.875 (5)	171

Symmetry codes: (i) *x*, -*y*+1/2, *z*+1/2; (ii) -*x*, *y*+1/2, -*z*+1/2.

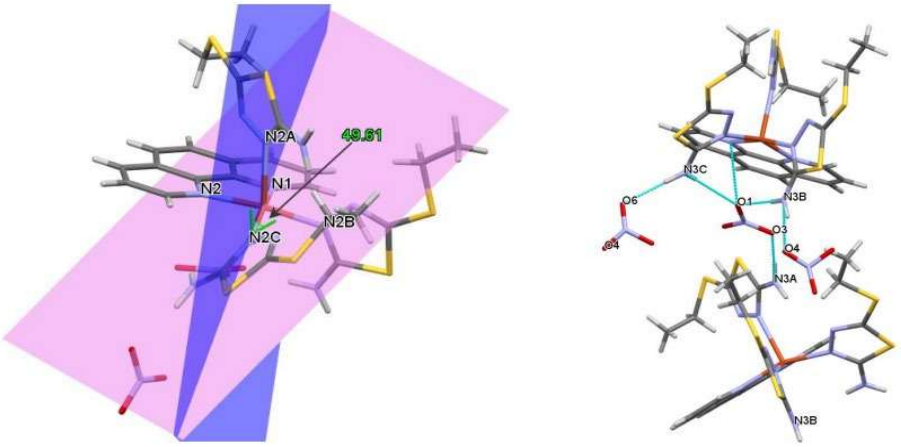

Figure 3. Hydrogen-bond parameters in the crystal structure of the $[CuL_3(phen)](NO_3)_2$ complex.

The complex compound 1,10-phenanthroline-tris(2-amino-5-ethylthio-1,3,4-thiadiazole)copper(II) dinitrate, according to elemental analysis, has the composition $[CuL_3(phen)](NO_3)_2$, where L denotes 2-amino-5-ethylthio-1,3,4-thiadiazole. The composition and structure of the synthesized complex were investigated based on the results of elemental analysis and X-ray diffraction analysis [19] (Figure 1). The product yield was 90%. The experimental/calculated elemental analysis results were as follows: C, 33.85/33.84%; H, 3.43/3.41%; O, 11.27/11.28%; Cu, 7.46/7.52%; N, 21.39/21.38%; and S, 22.59/22.56%. The crystals of $[CuL_3(phen)](NO_3)_2$ exhibit an ionic molecular structure. The Cu(II) ion is coordinated by the nitrogen atoms of three thiadiazole rings and two nitrogen atoms of the bidentate 1,10-phenanthroline ligand, forming the inner coordination sphere of the complex, while two nitrate anions are located in the outer sphere. The crystal structure is additionally stabilized by hydrogen-bonding interactions. The Cu–N bond lengths involving Cu(1)–N(2B), Cu(1)–N(2C), Cu(1)–N(2A), Cu(1)–N(1), and Cu(1)–N(2) are 2.003(3), 2.041(3), 2.273(3), 2.040(3), and 2.024(3) Å, respectively [20]. The Cu(1)–N(2A) bond is significantly elongated by 0.232 Å compared with the other Cu–N bonds. This elongation is attributed to the Jahn–Teller effect characteristic of Cu(II) complexes and corresponds to the nitrogen atom of the thiadiazole ligand occupying the axial position of the distorted tetragonal-pyramidal coordination environment.

The angles of the distorted coordination polyhedron also exhibit different values: 85.2(1)° (N2A–Cu1–N2), 93.3(1)° (N2A–Cu1–N1), 104.6(1)° (N2A–Cu1–N2B), and

104.7(1)° (N2A–Cu1–N2C). The L (C) ligand is oriented with a deviation of 49.61° relative to the meridional plane of the coordination polyhedron. This rotation around the ligand axis contributes to the formation of both intra- and intermolecular hydrogen-bonding interactions within the crystal structure.

Conclusion and Recommendations

A new mixed-ligand $[CuL_3(phen)](NO_3)_2$ complex was synthesized from copper(II) nitrate with 2-amino-5-ethylthio-1,3,4-thiadiazole (L) and 1,10-phenanthroline (phen), and its crystal structure was determined by single-crystal X-ray diffraction (SC-XRD). The complex crystallizes in the monoclinic crystal system with the **$P2_1/c$** space group and exhibits a five-coordinate, distorted tetragonal-pyramidal geometry around the Cu(II) ion. In the crystal structure, three 2-amino-5-ethylthio-1,3,4-thiadiazole ligands coordinate to the Cu(II) ion in a monodentate mode, whereas 1,10-phenanthroline acts as a bidentate ligand. The Cu–N bond lengths range from 2.004(3) to 2.273(3) **Å,** with the relatively elongated axial Cu–N bond being consistent with the Jahn–Teller distortion characteristic of Cu(II) complexes. The crystal packing is stabilized by the presence of outer-sphere nitrate anions and N–H···O hydrogen bonds**.**

References:

[1]. Sigel H., Sigel A. (eds.). Metal Ions in Biological Systems. Vol. 40: Copper and Its Complexes in Biology and Medicine. – CRC Press, 2018.

[2]. Haas K.L., Franz K.J. Application of metal coordination chemistry to explore and manipulate cell biology // Chemical Reviews. – 2009. – Vol. 109, No. 10. – P. 4921–4960.

[3]. Denoyer D., Masaldan S., La Fontaine S., Cater M.A. Targeting copper in cancer therapy: “Copper Worth” investigation // Metallomics. – 2015. – Vol. 7, No. 11. – P. 1459–1476.

[4]. Yusuf M., Khan S.A. Synthetic and biological significance of 1,3,4-thiadiazole derivatives: A review // Journal of Saudi Chemical Society. – 2014. – Vol. 18, No. 1. – P. 1–18.

[5]. Hu Y., Li C.Z., Shi W.N., Zhou E.L., Dong W.X. Synthesis, crystal structures and luminescence of copper(II) complexes based on functionalized thiadiazole ligands // Polyhedron. – 2018. – Vol. 141. – P. 120–127.

[6]. Altintop M.D., Capan E.R., Kaplancikli Z.A. Synthesis and structural characterization of copper(II) complexes containing 1,3,4-thiadiazole derivatives // Inorganica Chimica Acta. – 2020. – Vol. 502. – Art. No. 119364.

[7]. Plech T., Wujec M., Majewska M., Kosikowska U., Malm A. Microbiological activity of 1,3,4-thiadiazole derivatives and their copper(II) complexes // Medicinal Chemistry Research. – 2013. – Vol. 22, No. 5. – P. 2531–2537.

[8]. Zhang S., Chu T., Wang Y. Crystal structure, Hirshfeld surface analysis and antitumor activity of a copper(II) complex bearing ethylthio-thiadiazole moiety // Journal of Molecular Structure. – 2021. – Vol. 1245. – Art. No. 131050.

[9]. Bencini A., Lippolis V. 1,10-Phenanthroline: A versatile building block for the synthesis of functional ligands and coordination complexes // Coordination Chemistry Reviews. – 2010. – Vol. 254, No. 17–18. – P. 2096–2180.

[10]. Janiak C. A critical account on π···π stacking in metal complexes with aromatic nitrogen-containing ligands // Journal of the Chemical Society, Dalton Transactions. – 2000. – No. 21. – P. 3885–3896.

[11]. Patel R.N., Singh N., Shukla K.K., Gundla V.L. Synthesis, crystal structure and biological studies of mixed ligand copper(II) complexes with 1,10-phenanthroline // Spectrochimica Acta Part A: Molecular and Biomolecular Spectroscopy. – 2012. – Vol. 92. – P. 180–187.

[12]. Spek A.L. Structure validation in chemical crystallography // Acta Crystallographica Section E: Crystallographic Communications. – 2020. – Vol. 76, No. 1. – P. 1–11.

[13]. Addison A.W., Rao T.N., Reedijk J., van Rijn J., Verschoor G.C. Synthesis, spectral, and magnetic properties of copper(II) complexes with chelating ligands // Journal of the Chemical Society, Dalton Transactions. – 1984. – No. 7. – P. 1349–1356.

[14]. Starosta R., Kampfe A. Structural diversity and Jahn–Teller distortion in mixed-ligand copper(II) complexes // CrystEngComm. – 2017. – Vol. 19, No. 15. – P. 2045–2058.

[15]. Steiner T. The hydrogen bond in the solid state // Angewandte Chemie International Edition. – 2002. – Vol. 41, No. 1. – P. 48–76.

[16]. Kadirova Sh.A., Torambetov B.S., Toshmurodov T.T., Ziyaev A.A., Azimova D.A. Synthesis and investigation of zinc and copper nitrates with 2-ethylthio-5-acetamido-1,3,4-thiadiazole // Austrian Journal of Technical and Natural Sciences. – Vienna, 2019. – № 3–5. – P. 45–50.

[17]. Deng Y., Liu J., Zhang Q., Li F., Yang Y., Li P., Ma J. Transition metal-induced reductive coupling of 2-amino-1,3,4-thiadiazole with acetonitrile: Synthesis and structural characterization of two Co(III) complexes with amidine // Inorganic Chemistry Communications. – 2008. – Vol. 11, № 4. – P. 433–437.

[18]. Bharati P., Bharti A., Bharty M.K., Kashyap S., Singh U.P., Singh N.K. Synthesis, spectral and structural characterization of Ni(II), Cu(II), Zn(II), Cd(II) and Hg(II) complexes with 2-mercapto-5-methyl-1,3,4-thiadiazole: A Zn(II) complex acting as a new sensitive and selective fluorescent probe for the detection of Hg^{2+} in H_2O–MeOH medium // Polyhedron. – 2013. – Vol. 63, № 9. – P. 222–231.

[19]. Суворов Э.В. Методы исследования структуры и состава материалов. – М.: Юрайт, 2019. – 180 с.

[20]. Кривовичев С.В. Практические вопросы рентгеноструктурного анализа. Ч. 2. Расшифровка и уточнение кристаллических структур в комплексе SHELIX: учебное пособие. – СПб.: СПГУ, 2007. – 112 с.

Section 5. ACTUAL PROBLEMS IN MODERN AGRICULTURE

UDC 633.174:631.8

EFFECT OF MINERAL FERTILIZER RATES ON THE GROWTH, GRAIN YIELD, AND ECONOMIC EFFICIENCY OF SORGHUM

Latipova Ruzajon Shavkatovna
PhD Student in Plant Science, Urgench State University named after Abu Rayhan Beruni
ruza.shavkatovna@gmail.com

Annotatsiya. Tadqiqotda mineral o‘g‘it me’yorlarining “Daulet” oq jo‘xori navida barg yuzasi indeksi, don hosildorligi va iqtisodiy samaradorlikka ta’siri baholandi. Eng yuqori barg yuzasi indeksi (5,21 m²/m²) $N_{240}P_{140}K_{120}$ kg/ga variantida qayd etildi. Biroq eng yuqori don hosildorligi (6,12 t/ga), sof foyda (18 131 380 so‘m/ga) va rentabellik (108,12%) $N_{200}P_{120}K_{100}$ kg/ga me’yorida olindi. Shu sababli mazkur me’yor agronomik va iqtisodiy jihatdan eng samarali variant sifatida belgilandi.

Kalit so‘zlar: *“Daulet” navi, mineral o‘g‘itlar, azot, fosfor, kaliy, barg Ruza sathi indeksi, don hosildorligi, sof foyda, rentabellik.*

Аннотация. В исследовании оценено влияние норм минеральных удобрений на индекс листовой поверхности, урожайность зерна и экономическую эффективность сорта сорго “Даулет”. Наибольший индекс листовой поверхности (5,21 м²/м²) отмечен при внесении $N_{240}P_{140}K_{120}$ кг/га. Однако максимальная урожайность зерна (6,12 т/га), чистая прибыль (18 131 380 сум/га) и рентабельность (108,12%) получены при норме $N_{200}P_{120}K_{100}$ кг/га. Следовательно, эта норма признана наиболее эффективной в агрономическом и экономическом отношении.

Ключевые слова: *сорт “Даулет”, минеральные удобрения, азот, фосфор, калий, индекс листовой поверхности, урожайность зерна, чистая прибыль, рентабельность.*

Abstract. This study evaluated the effects of mineral fertilizer rates on the leaf area index, grain yield, and economic efficiency of the “Daulet” sorghum cultivar. The highest leaf area index of 5.21 m²/m² was recorded with $N_{240}P_{140}K_{120}$ kg/ha. However, the highest grain yield of 6.12 t/ha, net profit of 18 131 380 UZS/ha, and profitability of 108.12% were obtained with $N_{200}P_{120}K_{100}$ kg/ha. Therefore, this fertilizer rate was identified as the most agronomically and economically efficient treatment.

Key words: *“Daulet” cultivar, mineral fertilizers, nitrogen, phosphorus, potassium, leaf area index, grain yield, net profit, profitability.*

Introduction

In sorghum (Sorghum bicolor (L.) Moench), mineral nutrient supply directly influences leaf area development, photosynthetic activity, biomass accumulation, and grain yield. Nitrogen promotes canopy expansion and chlorophyll formation, whereas phosphorus and potassium support root development, water regulation, assimilate transport, and reproductive growth. However, increasing fertilizer rates beyond crop

requirements may not provide additional yield and can reduce nutrient-use efficiency and increase fertilizer losses.

Information on the combined effects of NPK fertilizer rates on leaf area index, grain yield, and economic efficiency of the “Daulet” cultivar under the irrigated conditions of the Khorezm region remains limited. Therefore, this study aimed to evaluate these responses and identify the agronomically and economically optimal mineral fertilizer rate for the “Daulet” grain sorghum cultivar.

Literature review

Previous studies have demonstrated that mineral fertilizer application can substantially influence sorghum canopy development, photosynthetic activity, and grain yield. Addai and Alimiyawo [1] reported that fertilizer application improved sorghum growth parameters and leaf area index, particularly during the later stages of plant development. Muchow [8] also showed that leaf area development in sorghum was highly responsive to nitrogen supply. Zhao et al. [9] found that nitrogen deficiency restricted plant growth, leaf area formation, and photosynthetic activity. These findings confirm that adequate nitrogen availability is essential for establishing and maintaining a photosynthetically active canopy.

Sorghum yield responses to fertilizer application vary depending on nutrient rate, application timing, genotype, soil properties, and environmental conditions. Buah et al. [2] observed that NPK fertilizer application increased grain yield, although the response became limited at higher nutrient rates. Gebremariam and Assefa [3] obtained the highest grain yield at a nitrogen rate of 150 kg/ha. Temeche et al. [6] recorded a grain yield of 5.84 t/ha when 138 kg N/ha was applied in two split doses, compared with 4.29 t/ha in the unfertilized control. These results emphasize that both fertilizer rate and application timing influence the agronomic effectiveness of nitrogen.

The response of sorghum to nitrogen fertilization is also strongly affected by genotype. Mahama et al. [10] reported differences in growth and grain yield responses among sorghum hybrids and inbred lines under different nitrogen rates. Bollam et al. [12] identified substantial genotypic variation in grain yield, biomass production, and nitrogen-use efficiency under contrasting nitrogen regimes. Similarly, Trotsenko et al. [7] showed that the effects of mineral fertilizers on grain yield differed among sorghum cultivars and hybrids. Therefore, a fertilizer rate identified as optimal for one genotype or production environment cannot be applied universally.

The combined effects of nitrogen, phosphorus, and potassium must also be considered when developing fertilizer recommendations. Kaizzi et al. [11] demonstrated that sorghum responded to nitrogen and phosphorus application, but the economically optimal nutrient rates varied among experimental sites. Long-term research by Schlegel and Havlin [13] showed that the productivity of irrigated grain sorghum was influenced by the combined application of nitrogen, phosphorus, and potassium. Atique-ur-Rehman et al. [14] also reported that phosphorus and potassium application improved sorghum growth and fodder productivity under arid soil conditions. These findings indicate that balanced nutrient application is more appropriate than considering nitrogen alone.

Agronomic yield is insufficient as the sole criterion for identifying the optimal fertilizer rate. Mahama et al. [4] demonstrated the importance of evaluating fertilizer

treatments in relation to both grain yield and economic return. Kaizzi et al. [11] similarly assessed economically optimal nutrient rates and showed that the most profitable fertilizer rate may differ from the rate producing the maximum biological yield. Moreover, Ostmeyer et al. [5] emphasized that improving nitrogen-use efficiency is necessary for increasing sorghum productivity while limiting unnecessary fertilizer inputs. Rowlings et al. [15] showed that environmental conditions, particularly rainfall distribution, strongly affected nitrogen recovery, nitrogen-use efficiency, and fertilizer losses in sorghum production.

Although previous studies have provided valuable information on sorghum responses to mineral fertilizers, most have focused on individual nutrients, single yield components, or environmental conditions different from those of the Khorezm region. Information integrating leaf area index development, grain yield, and economic efficiency under combined NPK fertilizer application remains insufficient for the "Daulet" cultivar. Therefore, the present study aimed to evaluate the effects of different mineral fertilizer rates on leaf area index, grain yield, and economic returns and to identify the optimal fertilizer rate for the "Daulet" grain sorghum cultivar under the irrigated conditions of the Khorezm region.

Research Methodology

The field experiment was conducted in 2025 at the Khorezm Cotton Research Station of the Research Institute of Cotton Breeding, Seed Production and Agrotechnologies, Khorezm region, Uzbekistan.

Four fertilizer treatments were evaluated: $N_0P_0K_0$, $N_{160}P_{100}K_{80}$, $N_{200}P_{120}K_{100}$, and $N_{240}P_{140}K_{120}$ kg/ha. The rates were expressed as N, P_2O_5, and K_2O. Before sowing, 25% of the nitrogen and the full rates of phosphorus and potassium were applied during soil preparation. The remaining nitrogen was divided equally between the S2 and S4 growth stages. Urea (46% N), ammophos (11% N and 46% P_2O_5), and potassium chloride (60% K_2O) were used as fertilizer sources. The crop was sown with 60 cm between rows and 15 cm between plants, with one plant per hill.

Plant development was monitored from emergence (S0) to physiological maturity (S9). Leaf area was measured at the S2, S3, S4, S5, S6, and S8 stages using a LI-COR 3100 area meter. The leaf area index was calculated as the ratio of total green leaf area to the ground area occupied by the plants and expressed as m^2/m^2 [1].

Grain yields were determined from two 16.67-m row sections in each subplot. Economic efficiency was evaluated using 2025 market prices. Gross revenue was calculated from grain and stalk sales, net profit as the difference between gross revenue and total production costs, and profitability as the ratio of net profit to total production costs expressed as a percentage.

Analysis and results

The leaf area index (LAI) is an important ecological indicator of the photosynthetically active leaf area of a plant and is defined as the ratio of total green leaf area to the ground area occupied by the plants. This study evaluated the effects of mineral fertilizer rates on LAI development in the "Daulet" cultivar (Table 1).

At the S2 growth stage, LAI values were relatively low, ranging from 0.09 to 0.14 m^2/m^2 across the treatments. LAI increased consistently with increasing mineral

fertilizer rates. At the S3 stage, it ranged from 0.27 to 0.42 m²/m². By the S4 stage, rapid leaf area development had increased LAI almost threefold compared with the previous stage, reaching 0.87–1.32 m²/m².

Table 1. Effect of mineral fertilizer rates on leaf area index development in the "Daulet" cultivar, 2025.

Mineral fertilizer rate, kg/ha	Leaf area index at different growth stages, m²/m²					
	S2	S3	S4	S5	S6	S8
$N_0P_0K_0$	0.09	0.27	0.87	2.85	2.78	2.50
$N_{160}P_{100}K_{80}$	0.12	0.37	1.10	3.53	3.95	3.75
$N_{200}P_{120}K_{100}$	0.13	0.40	1.24	4.27	5.01	4.36
$N_{240}P_{140}K_{120}$	0.14	0.42	1.32	4.64	5.21	4.75

At the S5 stage, the photosynthetically active leaf area continued to expand, and LAI ranged from 2.85 to 4.64 m²/m². These values were 3.2–3.5 times higher than those recorded at the S4 stage, indicating that the period between S4 and S5 was a critical phase of rapid leaf area development in the "Daulet" cultivar.

At the S6 stage, LAI in the unfertilized control decreased slightly from the S5 value to 2.78 m²/m². In the fertilized treatments, however, LAI continued to increase, reaching 3.95, 5.01, and 5.21 m²/m² under $N_{160}P_{100}K_{80}$, $N_{200}P_{120}K_{100}$, and $N_{240}P_{140}K_{120}$ kg/ha, respectively. The highest LAI was recorded in the $N_{240}P_{140}K_{120}$ kg/ha treatment.

The increase in LAI up to the S6 stage with increasing fertilizer rates indicated improved nutrient availability and greater development of the photosynthetically active leaf area. Similarly, Addai and Alimiyawo [1] reported higher growth parameters and LAI at later developmental stages in NPK-fertilized sorghum plants than in the unfertilized control. At the S8 stage, LAI declined in all treatments because of natural leaf senescence, yellowing, and a reduction in photosynthetically active leaf area. This finding is consistent with previous reports on the relationships among nitrogen-use efficiency, maintenance of leaf greenness, and leaf senescence [5]. Nevertheless, LAI remained higher as the fertilizer rate increased, ranging from 2.50 m²/m² in the control to 3.75, 4.36, and 4.75 m²/m² under $N_{160}P_{100}K_{80}$, $N_{200}P_{120}K_{100}$, and $N_{240}P_{140}K_{120}$ kg/ha, respectively.

The results showed that mineral fertilizer rates had a significant effect on the grain yield of the "Daulet" cultivar. In the unfertilized control treatment ($N_0P_0K_0$), grain yield was 2.53 t/ha (Figure 1). When mineral fertilizers were applied at $N_{160}P_{100}K_{80}$ kg/ha, grain yield increased to 5.01 t/ha, representing an increase of 2.48 t/ha or 98.0% compared with the control.

When the fertilizer rate was increased to $N_{200}P_{120}K_{100}$ kg/ha, the highest grain yield of 6.12 t/ha was recorded. This was 3.59 t/ha or 141.9% higher than the control. At $N_{240}P_{140}K_{120}$ kg/ha, grain yield was 6.08 t/ha, which was 0.04 t/ha lower than that obtained with $N_{200}P_{120}K_{100}$ kg/ha. Thus, increasing the fertilizer rate above $N_{200}P_{120}K_{100}$ kg/ha did not provide any additional grain yield in the "Daulet" cultivar.

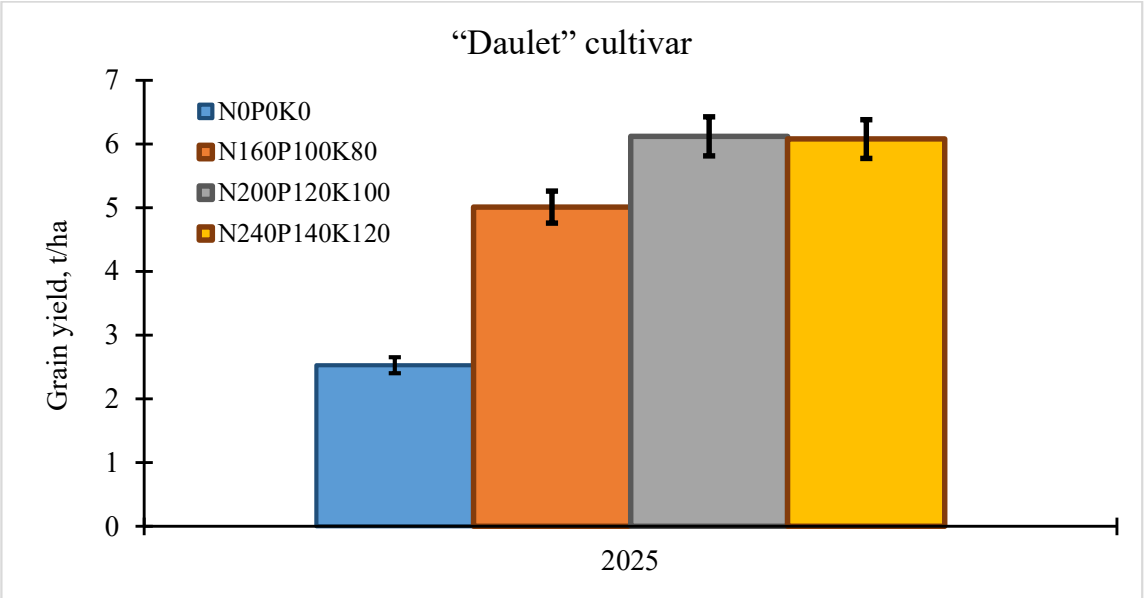

Figure 1. Effect of mineral fertilizer rates on the grain yield of the "Daulet" cultivar

These results indicate that the grain yield response of sorghum to mineral fertilizers continued only up to a certain level. Buah et al. [2] reported that nitrogen rates of 40, 80, and 120 kg/ha increased grain yield by 47%, 60%, and 69%, respectively, compared with the control. However, the yield difference between the nitrogen rates of 80 and 120 kg/ha was not statistically significant, while nitrogen-use efficiency declined as the fertilizer rate increased. This finding is consistent with the results of the present study, in which grain yields of 6.12 and 6.08 t/ha were obtained with $N_{200}P_{120}K_{100}$ and $N_{240}P_{140}K_{120}$ kg/ha, respectively.

Trotsenko et al. [7] also reported that $N_{35}P_{35}K_{35}$ and $N_{70}P_{70}K_{70}$ kg/ha fertilizer rates increased sorghum grain yield, although fertilizer efficiency depended on the characteristics of the cultivar or hybrid. These findings demonstrate that the optimal mineral fertilizer rate should be determined separately for each cultivar and specific soil and climatic conditions. Evaluating the economic efficiency of mineral fertilizer rates is essential for determining their optimal level of application. This assessment considers the effects of fertilizer rates on yield, gross revenue from product sales, net profit, and profitability. In 2025, the unfertilized control treatment ($N_0P_0K_0$) generated the lowest gross revenue of 14 562 148 UZS/ha from the sale of grain and stalk yield of the "Daulet" cultivar. Gross revenue increased to 28 515 966 UZS/ha with $N_{160}P_{100}K_{80}$ kg/ha and reached its highest value of 34 900 638 UZS/ha with $N_{200}P_{120}K_{100}$ kg/ha. Net profit was 1 032 021 UZS/ha in the control and increased to 12 368 447 UZS/ha with $N_{160}P_{100}K_{80}$ kg/ha. The highest net profit of 18 131 380 UZS/ha was obtained with $N_{200}P_{120}K_{100}$ kg/ha. When the fertilizer rate was increased to $N_{240}P_{140}K_{120}$ kg/ha, net profit declined to 17 439 233 UZS/ha, which was 692 147 UZS/ha lower than that obtained with $N_{200}P_{120}K_{100}$ kg/ha. The highest profitability rate of 108.12% was also recorded with $N_{200}P_{120}K_{100}$ kg/ha, while the net profit-to-gross revenue ratio was 0.520. Increasing the fertilizer rate to $N_{240}P_{140}K_{120}$ kg/ha reduced profitability to 100.28% and the net profit-to-gross revenue ratio to 0.501. Therefore, under the conditions of 2025, $N_{200}P_{120}K_{100}$ kg/ha was the most economically efficient fertilizer rate for the "Daulet" cultivar. The highest fertilizer rate does not always provide the greatest economic return.

Although Temeche et al. [6] obtained the highest biological grain yield at a nitrogen rate of 138 kg/ha, applying 46 kg/ha nitrogen in two split applications was recommended as the most economically efficient treatment. Mahama et al. [4] also reported that relatively low and moderate fertilizer rates were more economically sustainable. Similarly, the absence of further increases in grain yield and net profit at $N_{240}P_{140}K_{120}$ kg/ha in the present study confirms that $N_{200}P_{120}K_{100}$ kg/ha was the economically optimal rate for the "Daulet" cultivar.

Conclusion and Recommendations

Based on the results obtained under the experimental conditions of 2025, the following conclusions and recommendations were formulated:

1. Mineral fertilizer application considerably improved leaf area development and grain yield of the "Daulet" sorghum cultivar. The highest leaf area index of 5.21 m^2/m^2 was recorded with $N_{240}P_{140}K_{120}$ kg/ha.
2. The $N_{200}P_{120}K_{100}$ kg/ha treatment produced the highest grain yield of 6.12 t/ha, net profit of 18,131,380 UZS/ha, and profitability of 108.12%, making it the most agronomically and economically efficient treatment.
3. For the "Daulet" cultivar grown under comparable irrigated conditions of the Khorezm region, $N_{200}P_{120}K_{100}$ kg/ha is recommended as the optimal mineral fertilizer rate. Increasing the rate to $N_{240}P_{140}K_{120}$ kg/ha is not economically justified because it provides no additional grain yield or economic benefit.

References

[1] Addai I.K., Alimiyawo M. Graphical determination of leaf area index and its relationship with growth and yield parameters of sorghum (Sorghum bicolor L. Moench) as affected by fertilizer application // Journal of Agronomy. – 2015. – Vol. 14, No. 4. – P. 272–278. DOI: https://doi.org/10.3923/ja.2015.272.278

[2] Buah S.S.J., Kombiok J.M., Abatania L.N. Grain sorghum response to NPK fertilizer in the Guinea Savanna of Ghana // Journal of Crop Improvement. – 2012. – Vol. 26, No. 1. – P. 101–115. DOI: https://doi.org/10.1080/15427528.2011.616625

[3] Gebremariam G., Assefa D. Nitrogen fertilization effect on grain sorghum (Sorghum bicolor L. Moench) yield, yield components and witchweed (Striga hermonthica (Del.) Benth) infestation in Northern Ethiopia // International Journal of Agricultural Research. – 2015. – Vol. 10, No. 1. – P. 14–23. DOI: https://doi.org/10.3923/ijar.2015.14.23

[4] Mahama G.Y., Prasad P.V.V., Roozeboom K.L., Nippert J.B., Rice C.W. Cover crops, fertilizer nitrogen rates, and economic return of grain sorghum // Agronomy Journal. – 2016. – Vol. 108, No. 1. – P. 1–16. DOI: https://doi.org/10.2134/agronj15.0135

[5] Ostmeyer T.J., Bahuguna R.N., Kirkham M.B., Bean S., Jagadish S.V.K. Enhancing sorghum yield through efficient use of nitrogen: Challenges and opportunities // Frontiers in Plant Science. – 2022. – Vol. 13. – Article 845443. DOI: https://doi.org/10.3389/fpls.2022.845443

[6] Temeche D., Getachew E., Hailu G. Effects of nitrogen fertilizer quantity and time of application on sorghum (Sorghum bicolor (L.) Moench) production in lowland areas of North Shewa, Ethiopia // International Journal of Agronomy. – 2021. – Vol. 2021. – Article 3019528. DOI: https://doi.org/10.1155/2021/3019528

[7] Trotsenko V., Zhatova H., Kovalenko M. Yield of grain sorghum depends on fertilizer and varietal characteristics // Bulletin of Sumy National Agrarian University. The Series: Agronomy and Biology. – 2025. – Vol. 58, No. 4. – P. 9–15. DOI: https://doi.org/10.32782/agrobio.2024.4.2

[8]Muchow R.C. Effect of nitrogen supply on the comparative productivity of maize and sorghum in a semi-arid tropical environment. I. Leaf growth and leaf nitrogen // Field Crops Research. – 1988. – Vol. 18, No. 1. – P. 1–16. DOI: https://doi.org/10.1016/0378-4290(88)90055-X

[9] Zhao D., Reddy K.R., Kakani V.G., Reddy V.R. Nitrogen deficiency effects on plant growth, leaf photosynthesis, and hyperspectral reflectance properties of sorghum // European Journal of Agronomy. – 2005. – Vol. 22, No. 4. – P. 391–403. DOI: https://doi.org/10.1016/j.eja.2004.06.005

[10] Mahama G.Y., Prasad P.V.V., Mengel D.B., Tesso T.T. Influence of nitrogen fertilizer on growth and yield of grain sorghum hybrids and inbred lines // Agronomy Journal. – 2014. – Vol. 106, No. 5. – P. 1623–1630. DOI: https://doi.org/10.2134/agronj14.0092

[11] Kaizzi K.C., Byalebeka J., Semalulu O., Alou I., Zimwanguyizza W., Nansamba A., Musinguzi P., Ebanyat P., Hyuha T., Wortmann C.S. Sorghum response to fertilizer and nitrogen use efficiency in Uganda // Agronomy Journal. – 2012. – Vol. 104, No. 1. – P. 83–90. DOI: https://doi.org/10.2134/agronj2011.0182

[12] Bollam S., Romana K.K., Rayaprolu L., Vemula A., Das R.R., Rathore A., Gandham P., Chander G., Deshpande S.P., Gupta R. Nitrogen use efficiency in sorghum: Exploring native variability for traits under variable N-regimes // Frontiers in Plant Science. – 2021. – Vol. 12. – Article 643192. DOI: https://doi.org/10.3389/fpls.2021.643192

[13] Schlegel A.J., Havlin J.L. Irrigated grain sorghum response to 55 years of nitrogen, phosphorus, and potassium fertilization // Agronomy Journal. – 2021. – Vol. 113, No. 1. – P. 464–477. DOI: https://doi.org/10.1002/agj2.20453

[14] Atique-ur-Rehman, Qamar R., Altaf M.M., Alwahibi M.S., Al-Yahyai R., Hussain M. Phosphorus and potassium application improves fodder yield and quality of sorghum in Aridisol under diverse climatic conditions // Agriculture. – 2022. – Vol. 12, No. 5. – Article 593. DOI: https://doi.org/10.3390/agriculture12050593

[15] Rowlings D.W., Lester D.W., Grace P.R., Scheer C., De Rosa D., De Antoni Migliorati M., Friedl J., Bell M.J. Seasonal rainfall distribution drives nitrogen use efficiency and losses in dryland summer sorghum // Field Crops Research. – 2022. – Vol. 283. – Article 108527. DOI: https://doi.org/10.1016/j.fcr.2022.108527

Section 6. ACTUAL PROBLEMS OF MATHEMATICS, PHYSICS AND MECHANICS

UDK: 539.23

A COMPREHENSIVE STUDY OF THE STRUCTURE, MORPHOLOGY, AND WORK FUNCTION OF MoO_3 THIN FILMS DEPOSITED BY MAGNETRON SPUTTERING

Sharopov Utkirjon Bahodirovich
Doctor of Physical and Mathematical Sciences (DSc)
Institute of Physics and Technology, Academy of Sciences of Uzbekistan, Tashkent
utkirstar@gmail.com
Kuryozov Furqat Odilbekovich
Urgench RANCH Technological University, Department of Engineering, Urgench
kuryozovfurkat22@gmail.com

Annotatsiya. Ushbu ishda kremniy taglik ustida magnetron changitish usulida shakllantirilgan molibden oksidi MoO_3 yupqa pardalarining faza tarkibi, sirt morfologiyasi va chiqish ishi kompleks tarzda o‘rganildi. Rentgen difraktsiyasi (XRD) usuli bilan pardalarning amorf tuzilishga ega ekanligi aniqlandi; qalinlik ikki mustaqil usul – kvars mikrotarozilar va 2θ/θ geometriyasidagi reflektometriya bilan tasdiqlandi. Atom-kuch mikroskopiyasi (AKM) yordamida pardalar 5×5 mkm maydonda yaxlit qoplama hosil qilishi va sirt g‘adir-budirligi 2 nm dan oshmasligi ko‘rsatildi. Ultrabinafsha fotoelektron spektroskopiyasi (UFES) yordamida chiqish ishi 5,8±0,2 eV ekanligi aniqlandi; bu qiymat 10, 30 va 150 nm qalinlikdagi pardalar uchun deyarli o‘zgarmas bo‘lib qoldi. Olingan natijalar amorf, silliq va yuqori chiqish ishiga ega MoO_3 pardalari organik elektronika qurilmalarida kovak injeksiya qiluvchi qatlam sifatida istiqbolli ekanligini ko‘rsatadi.

Kalit so‘zlar: *Molibden oksidi; Magnetron changitish; Amorf parda; Atom-kuch mikroskopiyasi; Chiqish ishi; UFES; Organik elektronika.*

Аннотация. В работе комплексно изучены фазовый состав, морфология поверхности и работа выхода тонких плёнок оксида молибдена MoO_3, сформированных магнетронным распылением на кремниевой подложке. Методом рентгеновской дифракции (XRD) установлено, что плёнки имеют аморфную структуру; толщина подтверждена двумя независимыми методами – кварцевыми микровесами и рефлектометрией в геометрии 2θ/θ. С помощью атомно-силовой микроскопии (АСМ) показано, что плёнки формируют сплошное покрытие на участках 5×5 мкм с шероховатостью не более 2 нм. Методом ультрафиолетовой фотоэлектронной спектроскопии (УФЭС) определена работа выхода 5,8±0,2 эВ, остающаяся практически неизменной для плёнок толщиной 10, 30 и 150 нм. Результаты показывают, что аморфные, гладкие плёнки MoO_3 с высокой работой выхода перспективны в качестве дырочного инжектирующего слоя в устройствах органической электроники.

Ключевые слова: *Оксид молибдена; Магнетронное распыление; Аморфная плёнка; Атомно-силовая микроскопия; Работа выхода; УФЭС; Органическая электроника.*

Abstract. In this study, the phase composition, surface morphology, and work function of molybdenum oxide (MoO_3) thin films deposited on silicon substrates by magnetron sputtering were comprehensively investigated. X-ray diffraction (XRD) analysis revealed that the films exhibited an amorphous structure. The film thickness was independently verified using two methods: a quartz crystal microbalance and reflectometry in the 2θ/θ geometry. Atomic force microscopy (AFM) demonstrated that the films formed a continuous coating over an area of 5×5 μm, with a surface roughness not exceeding 2 nm. Ultraviolet photoelectron spectroscopy (UPS) measurements showed that the work function was 5.8±0.2 eV, remaining nearly unchanged for films with thicknesses of 10, 30, and 150 nm. The obtained results indicate that amorphous, smooth MoO_3 films with a high work function are promising as hole-injection layers in organic electronic devices.

Key words: *Molybdenum oxide; Magnetron sputtering; Amorphous film; Atomic force microscopy; Work function; Ultraviolet photoelectron spectroscopy (UPS); Organic electronics.*

Introduction

The efficiency of organic electronic devices–including organic light-emitting diodes (OLEDs), organic photovoltaic cells, and transistors–depends largely on the injection of charge carriers at the interface between the electrode and the organic layer [1], [2]. To achieve efficient hole injection, the work function of the contact layer should be close to the HOMO level of the organic material, which is typically in the range of 5–5.5 eV [3], [6]. Since conventional metal and silicon electrodes generally have work functions below 4.8 eV, a significant energy barrier arises at the interface.

Molybdenum oxide (MoO_3) has been extensively investigated as a hole-injection layer due to its high work function (up to 6 eV) and deeply located electronic states [3], [5]. However, the formation of an efficient injection contact depends not only on the work function but also on the phase composition, crystallinity, and surface roughness of the film. Low surface roughness of the underlying layer facilitates accurate control of the thickness of the subsequently deposited organic layer and promotes the formation of a uniform interface [11]. Amorphous films, in turn, generally exhibit smoother surfaces and more homogeneous morphology due to the absence of grain boundaries [4], [14]. The aim of this study is to comprehensively characterize the phase composition, thickness, surface morphology, and work function of MoO_3 films deposited by magnetron sputtering. To this end, X-ray diffraction (XRD), atomic force microscopy (AFM), and ultraviolet photoelectron spectroscopy (UPS) techniques were employed in combination. The structural state of MoO_3 films, whether amorphous or crystalline, is of significant importance for their practical applications. Crystalline MoO_3 typically exhibits a layered orthorhombic α-phase structure with anisotropic properties, whereas amorphous films are isotropic, smooth, and homogeneous, making them preferable for thin-film device applications [4], [8]. During the magnetron sputtering process, the substrate temperature, pressure, and oxygen flow rate determine the structural state of

the deposited film. Under low substrate temperature conditions, the formation of an amorphous phase is generally observed, which is considered advantageous for organic electronic devices [14], [15].

Research Methodology

MoO_3 films were deposited onto silicon Si(100) substrates by magnetron sputtering using a molybdenum target with a purity of 99.99% in a gas mixture consisting of 95% Ar and 5% O_2 in a Kepler 450 system. The working pressure was maintained at $(2–3) \times 10^{-2}$ mbar, and the film thickness was varied from 10 to 150 nm and monitored during deposition using a quartz crystal microbalance.

The phase composition and film thickness were investigated using a D8 Discover diffractometer (Bruker, Cu Kα, λ = 0.15406 nm) in both θ/2θ and 2θ/θ geometries. Surface topography and roughness were characterized by atomic force microscopy (AFM) using an Ntegra Spectra system (NT-MDT). The work function and electronic states of the valence band were investigated by ultraviolet photoelectron spectroscopy (UPS) using an Escalab 250Xi spectrometer equipped with a He I radiation source (21.2 eV). The measurements were performed without removing the samples from the vacuum chamber. The work function was determined from the cutoff position in the high-binding-energy region. The research methods employed and their respective purposes are summarized in Table 1.

Table 1. *Methods used to characterize MoO_3 films.*

Method	Instrument	Parameter determined
XRD	D8 Discover (Cu Kα)	phase composition, thickness
AKM	Ntegra Spectra	morphology, surface roughness
UFES	Escalab 250Xi (He I)	work function, valence band

Results and Discussions

No distinct diffraction peaks were observed in the diffractograms obtained in the θ/2θ geometry over the 2θ =20-60° range (Figure 1), indicating that the deposited MoO_3 layers possess an amorphous structure. This result is consistent with literature reports on the formation of an amorphous phase during magnetron sputtering under relatively low substrate-temperature conditions [8], [15]. Reflectometry measurements in the 2θ/θ geometry confirmed the thickness values determined using the quartz crystal microbalance during the deposition process. Thus, over the entire thickness range of 10-150 nm, the film thickness was determined by two independent methods with an accuracy of up to 10%. The surface roughness of the underlying silicon substrate did not exceed 1 nm, providing favorable conditions for the growth of the MoO_3 film. According to the AFM measurements, the MoO_3 films formed a continuous coating over areas of 5×5 μm and larger at all investigated thicknesses (Figure 2). Within these areas, the surface roughness did not exceed 2 nm, while the lateral dimensions of the features protruding above the mean surface level were predominantly 100-200 nm. The low surface roughness, combined with the amorphous structure, facilitates the formation of a uniform interface with the organic layer and represents an advantage for device fabrication [11]. To determine the work function, UPS spectra were measured. In the

valence-band spectrum of the 10 nm thick film, a broad maximum (shoulder) was observed in the energy range from −7.5 to −2.5 eV relative to the Fermi level, which is associated with Mo–O states of molybdenum atoms in MoO_3 [9], [10].

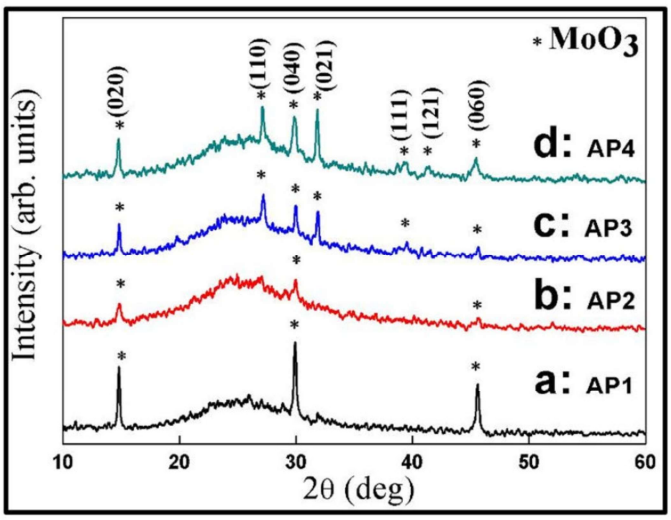

Figure 1. X-ray diffraction patterns of MoO_3 films with different thicknesses obtained in the θ/2θ geometry (amorphous halo).

The work function was determined from the cutoff position in the high-binding-energy region (Fig. 3). For the 10 nm-thick films, the work function was determined to be 5.8±0.2 eV. Similar results were obtained for the films with thicknesses of 30 and 150 nm: the work function remained at 5.8 eV within the stated experimental uncertainty (Figure 4). These results indicate that the work function is not significantly dependent on film thickness, suggesting the stability of the surface electronic states and the homogeneity of the deposited layer.

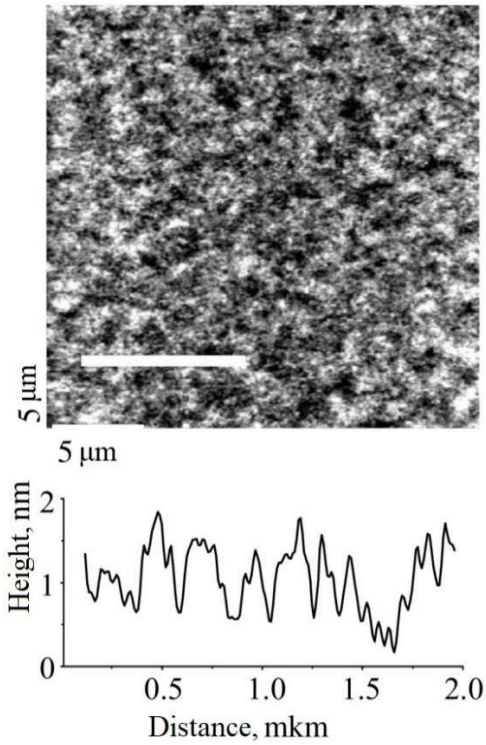

Figure 2. Atomic force microscopy (AFM) image of the MoO_3 film surface; surface roughness $R_a < 2$ nm.

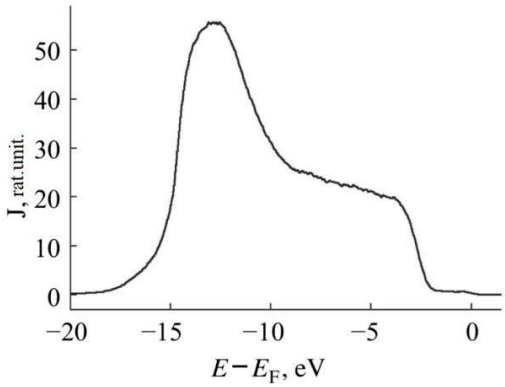

Figure 3. Valence-band UPS spectrum of the MoO_3 film (left) and the cutoff edge used to determine the work function (right), Φ=5.8±0.2 eV.

The work function values obtained for films of different thicknesses are presented in Table 2.

Table 2. Work function values of MoO_3 films.

Thickness (nm)	Work function Φ (eV)
10	5,8 ± 0,2
30	5,8 ± 0,2
150	5,8 ± 0,2

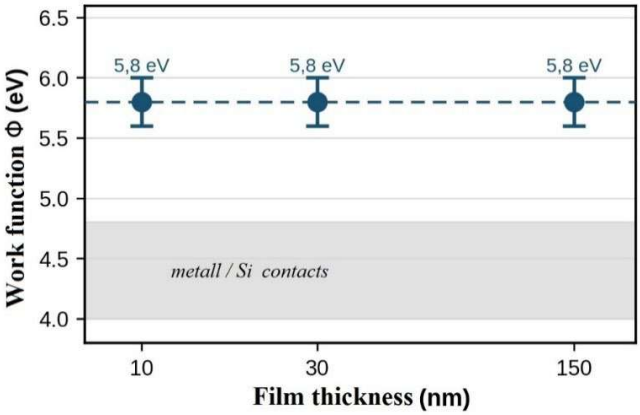

Figure 4. Dependence of the MoO_3 film work function, Φ, on film thickness; the gray region indicates the typical values for metal/Si contacts.

The measured work function values, ranging from 5.6 to 6.0 eV, are significantly higher than those of conventional metal and silicon contacts (below 4.8 eV) and are consistent with the values reported by other authors for magnetron-sputtered MoO_3 films [3], [5], [9]. Such a high work function is associated with the deep-lying electronic states of MoO_3 and provides favorable energetic alignment with the HOMO level of the organic material, thereby reducing the energy barrier for hole injection (Figure 5). Thus, comprehensive investigations confirmed that MoO_3 films deposited by magnetron sputtering exhibit an amorphous structure, low surface roughness (R_a < 2 nm), and a high work function (5.8 eV). Taken together, these properties make the films suitable for use as efficient hole-injection layers in organic electronic devices.

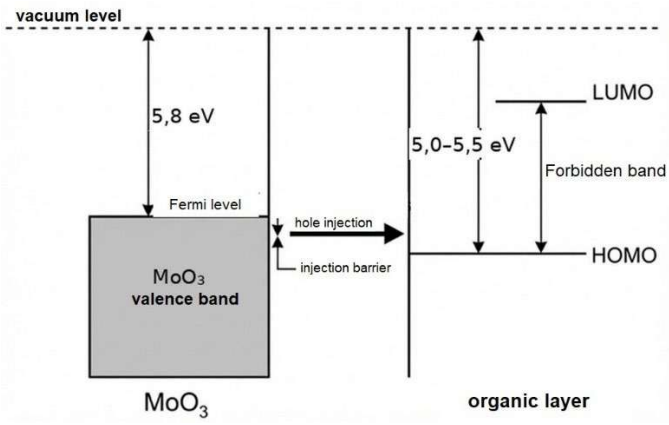

Figure 5. Energy-level diagram at the MoO_3/organic semiconductor interface and schematic representation of hole injection.

Conclusion and Recommendations

The structure, morphology, and work function of MoO_3 thin films deposited on silicon substrates by magnetron sputtering were comprehensively investigated. X-ray diffraction analysis revealed that the films possess an amorphous structure, while the film thickness was confirmed using two independent methods. Atomic force microscopy demonstrated that the films form a continuous coating over an area of 5×5 μm, with a surface roughness not exceeding 2 nm.

Ultraviolet photoelectron spectroscopy (UPS) measurements revealed a work function of 5.8±0.2 eV, which remained nearly unchanged over the 10-150 nm thickness range. The obtained results demonstrate that amorphous, smooth MoO_3 films with a high work function are promising for use as hole-injection layers in organic electronic devices. Future studies will focus on the direct evaluation of the injection properties of these films in actual OLED structures.

References:

[1] M. T. Greiner, Z. H. Lu, “Thin-film metal oxides in organic semiconductor devices,” NPG Asia Mater., vol. 5, p. e55, 2013, doi: 10.1038/am.2013.29.
[2] J. Meyer, S. Hamwi, M. Kröger, et al., “Transition metal oxides for organic electronics,” Adv. Mater., vol. 24, no. 40, pp. 5408–5427, 2012, doi: 10.1002/adma.201201630.
[3] M. Kröger, S. Hamwi, J. Meyer, et al., “Role of the deep-lying electronic states of MoO3 in the enhancement of hole injection,” Appl. Phys. Lett., vol. 95, p. 123301, 2009, doi: 10.1063/1.3231928.
[4] A. L. F. Cauduro, R. dos Reis, G. Chen, et al., “Crystalline molybdenum oxide thin-films for application as interfacial layers,” ACS Appl. Mater. Interfaces, vol. 9, no. 8, pp. 7717–7724, 2017, doi: 10.1021/acsami.6b14228.
[5] R. T. White, E. S. Thibau, Z. H. Lu, “Universal energy-level alignment of molecules at metal oxide interfaces,” Sci. Rep., vol. 6, p. 21109, 2016, doi: 10.1038/srep21109.
[6] I. G. Hill, A. Kahn, J. Cornil, et al., “Charge-separation energy in films of conjugated organic molecules,” Chem. Phys. Lett., vol. 317, pp. 444–450, 2000, doi: 10.1016/S0009-2614(99)01384-6.
[7] Z. Bin, H. Guo, Z. Liu, F. Li, et al., “Hole transporting materials,” ACS Appl. Mater. Interfaces, vol. 10, no. 5, pp. 4882–4886, 2018, doi: 10.1021/acsami.7b18261.
[8] N. Sharma, R. Kumar, J. Jayabalan, “Optical and structural properties of magnetron-sputtered MoO3 thin films,” Curr. Appl. Phys., vol. 21, pp. 58–65, 2021, doi: 10.1016/j.cap.2020.10.004.

[9] C. V. Ramana, V. V. Atuchin, V. G. Kesler, et al., “Electronic structure and chemical bonding in molybdenum-oxide films,” Appl. Surf. Sci., vol. 253, no. 12, pp. 5368–5374, 2007, doi: 10.1016/j.apsusc.2006.12.012.
[10] D. O. Scanlon, G. W. Watson, D. J. Payne, et al., “Theoretical and experimental study of the electronic structures of MoO3 and MoO2,” J. Phys. Chem. C, vol. 114, no. 10, pp. 4636–4645, 2010, doi: 10.1021/jp9093172.
[11] A. S. Komolov, E. F. Lazneva, N. B. Gerasimova, et al., “Conduction band electronic states of ultrathin layers of thiophene/phenylene co-oligomers,” J. Electron Spectrosc. Relat. Phenom., vol. 235, pp. 40–45, 2019, doi: 10.1016/j.elspec.2019.07.001.
[12] H. Lee, S. W. Cho, K. Han, et al., “The origin of the hole injection improvements at ITO/MoO3 interfaces,” Appl. Phys. Lett., vol. 93, p. 043308, 2008, doi: 10.1063/1.2965120.
[13] S. Tokito, K. Noda, Y. Taga, “Metal oxides as a hole-injecting layer for an organic EL device,” J. Phys. D: Appl. Phys., vol. 29, pp. 2750–2753, 1996, doi: 10.1088/0022-3727/29/11/004.
[14] U. B. Sharopov, K. Samiev, A. To‘raev, et al., “Surface defect formation studied by total current spectroscopy,” Vacuum, vol. 227, p. 113395, 2024, doi: 10.1016/j.vacuum.2024.113395.
[15] T. S. Sian, G. B. Reddy, “Optical, structural and photoelectron spectroscopic studies on amorphous and crystalline molybdenum oxide thin films,” Sol. Energy Mater. Sol. Cells, vol. 82, pp. 375–386, 2004, doi: 10.1016/j.solmat.2003.12.007.
[16] K. Jacobi, G. Zwicker, A. Gutmann, “Work function, electron affinity and band bending of zinc oxide surfaces,” Surf. Sci., vol. 141, pp. 109–125, 1984, doi: 10.1016/0039-6028(84)90199-7.

UDK: 662.997

ANALYSIS OF FLUID TEMPERATURE CHANGES DURING DISCHARGE IN HEAT ACCUMULATORS AND VALIDATION OF THE MATHEMATICAL MODEL

Mirzaev Mirfayz Salimovich
Associate Professor, PhD, Bukhara State University
m.s.mirzaev@buxdu.uz
Hikmatov Behzod Amonovich
PhD student, Bukhara State University
behzodhikmatov1996@gmail.com

Annotatsiya. Issiqlik akkumulyatorlari orasida issiq suv saqlash baklari arzonligi, soddaligi va ishlash rejimi qulayligi, atrof-muhitga zarari kamligi uchun eng ko’p qo’llaniladi. Issiq suv saqlash idishi ichidagi harorat taqsimoti tizimning issiqlik xususiyatlari va issiq suv yetkazib berish samaradorligini boshqaruvchi asosiy omil hisoblanadi. Bu taqsimotga bir qator ish va dizayn parametrlari ta'sir qiladi. Bularga suv kirish oqimi tezligi, kirish harorati, saqlash idishi ichidagi suvning boshlang'ich harorati, idish geometriyasi, idish diametrining balandlikka nisbati va kirish va chiqish quvurlarining joylashuvi kiradi. Bu parametrlarning o'zgarishi harorat tabaqalanishiga va natijada issiq suv saqlash idishining issiqlik samaradorligiga sezilarli darajada ta'sir qilishi mumkin. Issiq suv saqlash baklarining samaradorligining bu kabi ko‘plab parametrlarga bog‘liqligi matematik modellashtirish va raqamli simulyatsiyalardan foydalanishning ahamiyatini oshiradi. Ushbu tadqiqotda issiq suv saqlash baklari uchun bir o‘lchovli matematik model ishlab chiqilgan va eksperimental natijalar asosida tekshirilgan. Tadqiqot

natijalariga ko‘ra model va eksperiment orasidagi o‘rtacha kvadrat xatolik ildizi 1.85°C ga va determinatsiya koeffitsiyenti R^2=0.94 ga teng ekanligi aniqlandi. Issiq suv saqlash bakining to‘la razryadlanish vaqti 1980 soniya yoki 33 minutga teng.

Kalit so’zlar: *issiqlik akkumulyatori, issiqlik taqsimlanishi, o‘rtacha kvadrat xatolik ildiz, determinatsiya koeffitisiyenti, razryadlanish, razryadlanish vaqti.*

Аннотация. Среди теплоаккумуляторов наиболее широко используются накопительные баки с горячей водой благодаря их низкой стоимости, простоте конструкции и эксплуатации, а также низкому воздействию на окружающую среду. Термальная стратификация в баке горячего водоснабжения является важным фактором, влияющим на выдачу горячей воды. На термическую стратификацию воздействуют многие параметры: расход подаваемой жидкости, температура на входе, начальная температура в баке горячего водоснабжения, геометрическая конфигурация бака, его диаметр и отношение диаметра к высоте, а также положение входного и выходного патрубков. Зависимость эффективности баков-аккумуляторов горячей воды от большого количества подобных параметров повышает значимость применения математического моделирования и численного моделирования. В данной работе разработана одномерная математическая модель бака горячего водоснабжения, верифицированная на основе экспериментальных данных. По результатам исследования среднеквадратическая ошибка (RMSE) между моделью и экспериментом составила 1,85 °C, а коэффициент детерминации (максимальный коэффициент корреляции) - R^2 = 0,94. Полное время разряда бака горячей воды составляет 1980 с или 33 минуты.

Ключевые слова: *теплоаккумулятор, термическая стратификация, среднеквадратическая ошибка, коэффициент детерминации, разряд, время разряда.*

Abstract. Among heat accumulators, hot water storage tanks are the most widely used due to their low cost, simplicity, and ease of operation, as well as their low environmental impact. The temperature distribution within a hot water storage tank is a key factor governing the thermal behavior and hot water delivery performance of the system. This distribution is influenced by a number of operating and design parameters. These include the water inlet flow rate, inlet temperature, initial temperature of the water inside the storage tank, tank geometry, the tank diameter-to-height ratio, and the locations and arrangement of the inlet and outlet pipes. Variations in these parameters can significantly affect the temperature stratification and, consequently, the thermal performance of the hot water storage tank. The dependence of the efficiency of hot water storage tanks on many such parameters increases the importance of using mathematical modeling and numerical simulations. In the present study, a one-dimensional mathematical model was established to describe the thermal behavior of a hot water storage tank and subsequently validated against experimental data. The comparison between the numerical predictions and experimental measurements yielded an RMSE of 1.85

°C, while the coefficient of determination was calculated as R^2=0.94, demonstrating a strong agreement between the model results and experimental observations. The analysis also showed that the storage tank could be completely discharged within 1980 s, equivalent to 33 min.

Key words: *heat accumulator, thermal stratification, root mean square error, coefficient of determination, discharging, discharging time.*

Introduction

Due to the gradual depletion of traditional fossil fuel reserves and the increasing environmental impact, global efforts to conserve, store and develop renewable energy sources are increasing [1]. Despite the availability of various high-energy-density thermal storage technologies, including latent heat storage systems employing phase change materials (PCMs), hot water storage tanks remain among the most commonly applied solutions because of their relatively low cost, simple construction, and advantageous thermophysical characteristics [2]. In solar water heating systems, the thermal behavior of the hot water storage tank plays a significant role in determining the overall efficiency and performance of the system. One of the key factors governing the thermal performance of such tanks is temperature stratification, which influences the mixing behavior and heat storage characteristics of the stored water. Consequently, the phenomenon of thermal stratification in hot water storage tanks has received considerable attention in previous research studies [3].

Literature Review

Researchers have conducted many experimental studies and analytical simulations on temperature stratification in a hot water storage tank in a hot water system. The studies show that thermal stratification can effectively improve energy storage performance. Studies on the thermal stratification of hot water storage tanks mainly focus on the following aspects [4]: inlet flow parameters – liquid inlet flow [5, 6], inlet temperature, initial temperature in the hot water storage tank [7] and operating mode of the hot water storage tank [8-10]; geometric structure of the hot water storage tank: many literatures have studied the effect of geometric structure on thermal stratification, which is mainly reflected in the ratio of the diameter of the water tank to its height, the installation position of the liquid inlet and outlet pipes [11, 12], the structure of the barriers inside the water tank and other factors [13-15].

Considering the above, mathematical modeling and numerical simulations are of great importance due to the fact that the efficiency of hot water storage tanks depends on many parameters and the increasing number of experimental studies. In this study, the thermal stratification in the liquid layers of a hot water storage tank, determined by the studies of Y. Karlina [16] and A.L. Nash [17], was investigated using a one-dimensional mathematical model. Based on the model results and the research results of Y. Karlina [16], the root mean square error and the coefficients of determination were determined. Based on the mathematical model, the discharge time of the hot water storage tank was determined.

Research Methodology

A cylindrical hot water storage tank with an external heat exchanger is heated by hot water entering from the first layer above (Figure 1). In developing a one-dimensional

model of a hot water storage tank, the liquid inside the tank is divided into 20 equal layers, numbered from top to bottom. For the discharge process of a hot water storage tank, it is assumed that cold water enters from the 20th layer at the bottom of the tank and hot water leaves from the 1st layer.

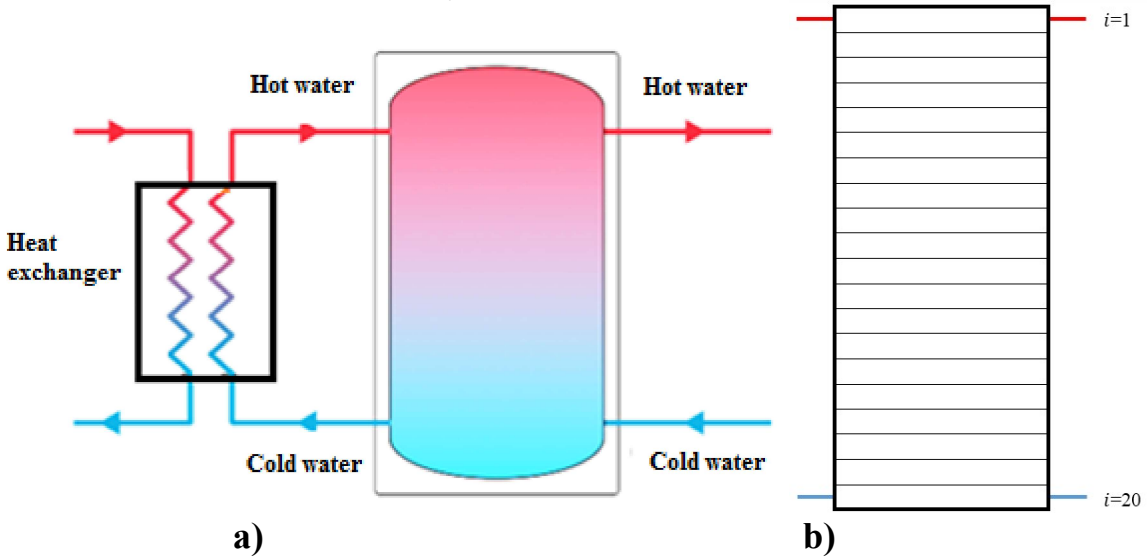

Figure 1. Schematic representation of a hot water storage tank: a) general configuration; b) liquid layers.

To develop and validate a one-dimensional mathematical model of a hot water storage tank, the geometric parameters of a hot water storage tank from an experimental study by A.L. Nash [17] were used (Table 1).

Table 1. Geometric parameters of the hot water storage tank.

Parameters of hot water storage tank	**Dimension**
Height (external/internal)	1.42 m / 1.30 m
Diameter (outer/inner)	0.51 m / 0.38 m
Wall thickness	0.0065 m
Volume	151 liter

Heat balance equations. Energy balance equations have been developed for the hot water storage tank configuration shown in Figure 1 [16].

$$C_w m_{w_i} \frac{dT_{w_i}}{dt} = \dot{Q}_{c,w_i} + \dot{Q}_{cf,w_i} - \dot{Q}_{loss_i} - \dot{Q}_{hwc} \quad (1)$$

here C_w - specific heat capacity of water; m_{w_i}- mass of water in each layer; $\dot{Q}_{c,w_i}$ - convective heat transfer rate between liquid layers; $\dot{Q}_{cf,w_i}$ - forced convective heat transfer rate due to direct addition and withdrawal of water to the hot water storage tank; $\dot{Q}_{loss_i}$ - rate of heat loss to the environment; $\dot{Q}_{hwc}$ - forced convective heat transfer rate due to hot water withdrawal and cold water addition; i - denotes the liquid layers in the tank and i takes values from 1 to 20, respectively.

The convective heat transfer rate $\dot{Q}_{c,w_i}$ between fluid layers is determined by the following expression:

$$\dot{Q}_{c,w_i} = \left(\frac{\left(T_{w_{i+1}} - T_{w_i}\right) k_w \Delta_{i+1}}{L_w} + \frac{\left(T_{w_{i-1}} - T_{w_i}\right) k_w \Delta_{i-1}}{L_w} \right) A_w \quad (2)$$

here A_w - cross-sectional area of the tank; Δ - Flexible Grid Multiplier; k_w - thermal conductivity coefficient of water.

The heat transfer rate between layers $\dot{Q}_{c,w_i}$ was calculated using the Adaptive Grid approach presented by K. Powell et al. [18], which enhances heat transfer by increasing the interference between layers when there is a temperature difference. In this work, based on experimental results, it was assumed that a more realistic placement of natural convection effects at a value of Δ=1/400 would allow for more efficient heat distribution in the hot water storage tank [16].

The forced convective heat transfer rate $\dot{Q}_{cf,w_i}$ due to the direct addition and withdrawal of water to the hot water storage tank is determined by the following expression:

$$\dot{Q}_{cf,w_i} = \dot{m}C_w(T_{w_{i-}} - T_{w_i}) \quad (3)$$

here $\dot{m}$ - mass flow rate of incoming water.

Due to the direct addition and withdrawal of water to the hot water storage tank, the forced convective heat transfer rate $\dot{Q}_{cf,w_i}$ represents the rate of temperature change in the upper layers due to the incoming hot water, increasing thermal efficiency by eliminating heat loss to the environment through the walls of the hot water storage tank.

The rate of heat loss to the environment $\dot{Q}_{loss_i}$ is determined by the following expression:

$$\dot{Q}_{loss_i} = \frac{A_{wall_i} k_{ti}\left(T_{w_i} - T_{room}\right)}{L_{ti}} \quad (4)$$

here T_{room} - represents the temperature of the room where the hot water storage tank is located. The rate of heat loss to the environment is calculated for each layer individually based on the insulation characteristics of the hot water storage tank, including insulation thickness and exposed surface area. For intermediate layers ($2 \leq i \leq 18$), the surface A_{wall_i} represents the side surface of the hot water storage tank, and for the upper ($i = 1$) and lower ($i = 20$) layers, it includes the side surface of the hot water storage tank and the upper/lower base surfaces.

The forced convective heat transfer rate $\dot{Q}_{hwc}$ due to hot water withdrawal and cold water addition is determined by the following expression:

$$\dot{Q}_{hwc} = C_w(T_{w_{20}} - T_{cold})\dot{m}_{t,fraction} \quad (5)$$

where $\dot{m}_{t,fraction}$ is the relative flow rate of the liquid, which is found as follows:

$$\dot{m}_{t,fract} = \dot{m}_t \cdot fraction \quad (6)$$

$\dot{m}_t$ is the total consumption rate of hot water, and $fraction$ represents the share of hot water:

$$fraction = \frac{(T_{use} - T_{cold})}{(T_{w_0} - T_{cold})} \quad (7)$$

T_{use} - temperature required by the consumer, T_{w_0} - hot water storage tank water intake temperature, T_{col} - the temperature of the cold water entering the bottom layer of the hot water storage tank.

Therefore, the forced convective heat transfer rate $\dot{Q}_{hwc}$due to hot water withdrawal and cold water addition is necessary to assess the exact effect of water withdrawal from the bottom layer of the hot water storage tank on the heat distribution and depends on the incoming cold water temperature T_{cold}. $\dot{Q}_{hwc}$is usually considered to affect the bottom two layers of the hot water storage tank or only the last layer.

Using expressions (8)-(9), the Root Mean Square Error ($RMSE$) and the maximum correlation coefficient R^2 between the results obtained in the studies of Y. Karlina and A.L. Nash and the results obtained from the developed one-dimensional mathematical model were determined.

RMSE - Root Mean Square Error [19]:

$$RMSE = \sqrt{\frac{1}{N}\sum_{\tau=1}^{N}\left(T_{\tau,mod} - T_{\tau,exp}\right)^2} \quad (8)$$

R^2 - maximum correlation coefficient [19]:

$$R^2 = 1 - \frac{\sum_{\tau=1}^{N}\left(T_{\tau,model} - T_{\tau,ex}\right)^2}{\sum_{\tau=1}^{N}\left(T_{mean,model} - T_{\tau,exp}\right)^2} \quad (9)$$

where $T_{\tau,mode}$ and $T_{\tau,ex}$ represent the model and experimental fluid temperatures at time τ, respectively, and $T_{mean,model}$ represents the average temperature based on the model results.

Analysis and Results

The heat balance equation was solved numerically using the differential equation scheme method, and the following conditions were adopted for the discharge process when solving the heat balance equations:

- The initial temperatures of each layer in the hot water storage tank are the same and equal to 45°C.
- The mass flow rate of the liquid during the discharge process in the hot water storage tank is 330 kg/h.
- The temperature of the cold water entering the lower 20th layer during the discharge process in the hot water storage tank is 15°C, and the hot water exits from the 1st layer.
- In the calculations, the $fraction$ constant was assumed to be equal to 0.92.

During the discharge process of the hot water storage tank, the liquid is divided into 20 equal layers, and the temperature of each layer is assumed to be 45°C. For the complete discharge of the hot water storage tank, the full discharge point is taken as the time when the average temperature of the cold water entering the hot water storage tank reaches 110 percent (16.5°C).

Figure 2 illustrates the temperature change in the liquid layers of the hot water storage tank based on the model results.

Figure 3 shows the temperature change per minute from the start of discharge in the odd-numbered liquid layers of the hot water storage tank until the average temperature of all layers is 16.5° C. The red dashed lines indicate the temperature change in the study by Y. Karlina, while the solid red line indicates the results of the one-dimensional mathematical model.

At a mass flow rate of 330 kg/h, the hot water storage tank required 1980 s, corresponding to approximately 33 min, to complete the discharge process. This value agrees well with the findings reported by Y. Karlina and A. L. Nash. The root mean square error (RMSE) associated with the temperature prediction for each individual layer was calculated using Eq. (8). A comparison between the results obtained from the one-dimensional mathematical model and the experimental data reported by Y.

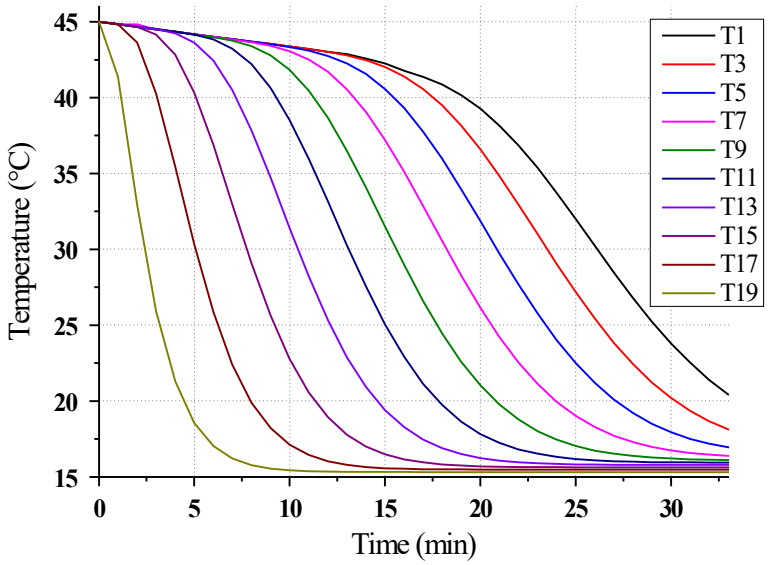

Figure 2. Temperature variation in the liquid layers of a hot water storage tank at a mass flow rate of 330 kg/h.

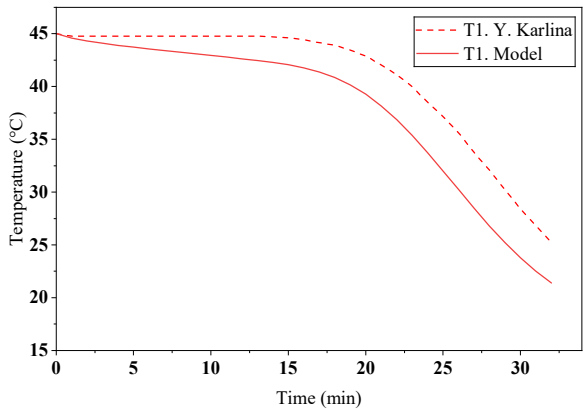

3a) Layer 1: RMSE=3.35°C

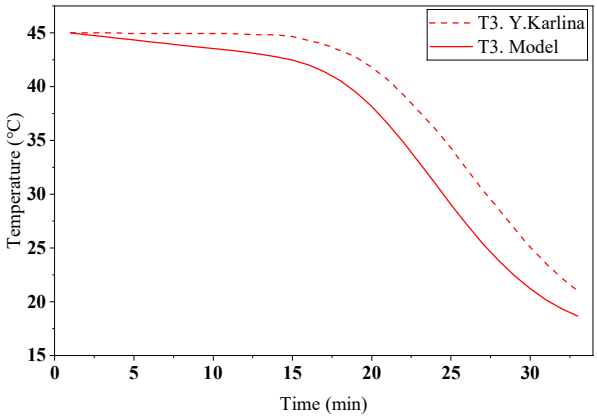

3b) Layer 3: RMSE=3.09°C

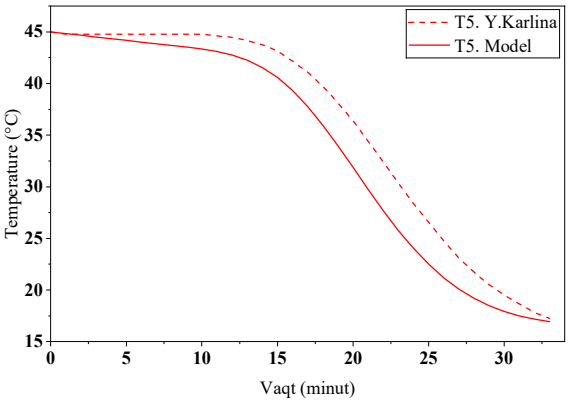

3c) Layer 5: RMSE=2.66°C

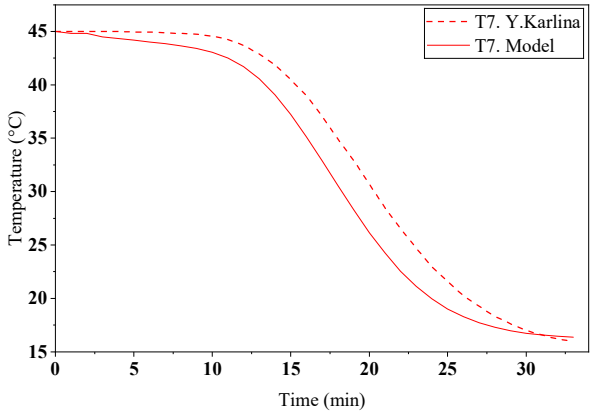

3d) Layer 7: RMSE=2.47°C

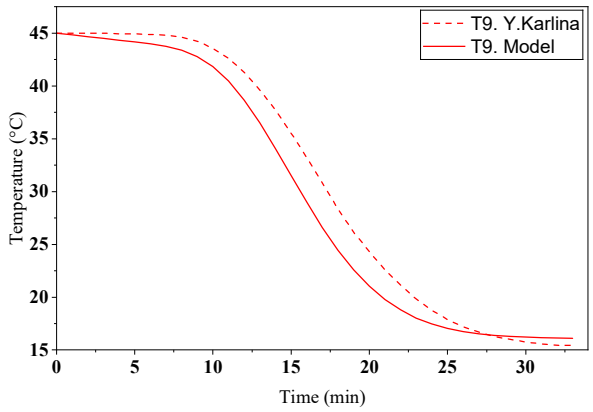

3e) Layer 9: RMSE=2.17°C

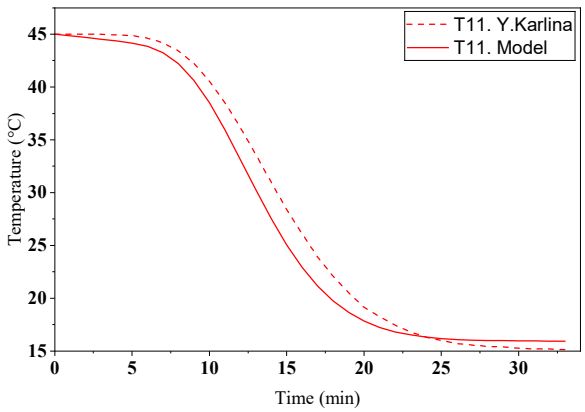

3f) Layer 11: RMSE=1.68°C

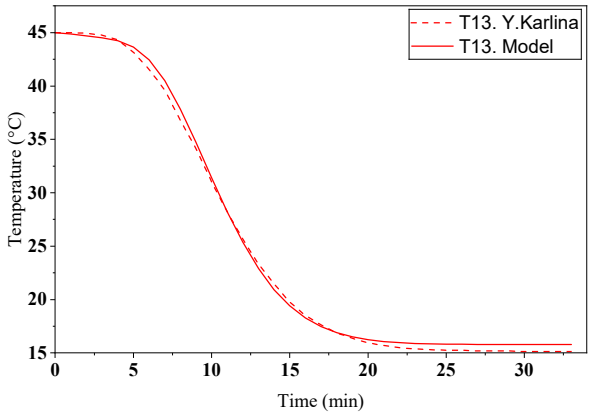

3g) Layer 13**:** RMSE=0.5°C

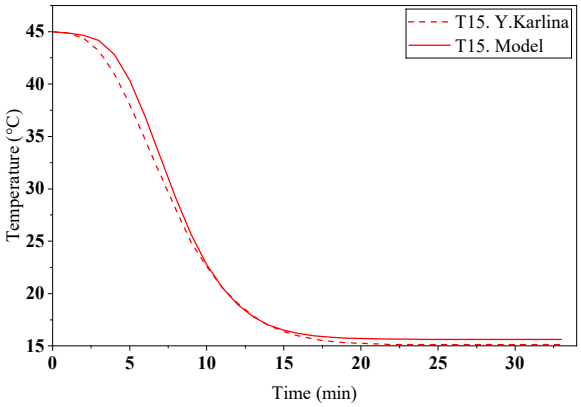

3h) Layer 15: RMSE=0.83°C

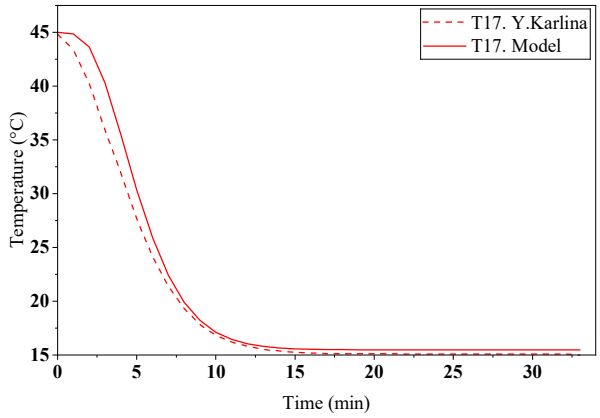

3i) Layer 17: RMSE=1.34°C

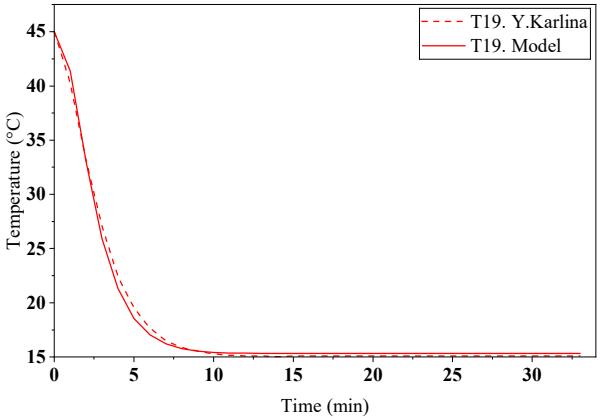

3j) Layer 19: RMSE=0.43°C

Figure 3. Assessment of the time dependence of temperature changes in an odd number of liquid layers of a hot water storage tank (based on Y. Karlina and model results) and Root Mean Square Error.

Karlina showed that the RMSE of the predicted temperature variation for all water layers throughout the discharge period was 1.85 °C. Furthermore, the calculated coefficient of determination was R^2 = 0.94, indicating a good agreement between the model predictions and the experimental results.

Conclusion and Recommendations

A one-dimensional mathematical model of a hot water storage tank was developed and validated using the experimental results reported by Y. Karlina. The governing

energy balance equations describing the thermal behavior of the storage tank were solved numerically by applying a differential equation-based solution approach. The model predictions were subsequently compared with the results presented by Y. Karlina to evaluate the accuracy of the developed model in terms of temperature prediction and tank discharge behavior.

The comparison demonstrated good agreement between the numerical and reference results. The RMSE calculated for the temperature variation of the water layers during the discharge process was 1.85 °C, while the coefficient of determination reached $R^2 = 0.94$. In addition, the calculated time required for complete discharge of the hot water storage tank was 33 min.

The developed one-dimensional model can be further employed to investigate the influence of different design and operating parameters on the thermal performance of hot water storage tanks. In particular, future numerical studies may consider the effects of water mass flow rate and inlet temperature, the initial water temperature, tank geometry, tank diameter-to-height ratio, and the locations of the inlet and outlet connections. Such analyses can provide a basis for optimizing the design and operating conditions of hot water storage systems.

References

[1] F. Alobaid, N. Mertens, R. Starkloff, et al., Progress in dynamic simulation of thermal power plants, Prog. Energy Combust. Sci. 59 (2017) 79-162.
[2] Iván De la Cruz-Loredo, Daniel Zinsmeister, Thomas Lickleder, Carlos E. Ugalde-Loo, Daniel A. Morales, Héctor Bastida, Vedran S. Perić, Arslan Saleem., Experimental validation of a hybrid 1-D multi-node model of a hot water thermal energy storage tank, Applied Energy 332 (2023) 120556.
[3] Y.M. Han, R.Z. Wang, Y.J. Dai, Thermal stratification within the water tank, Renew. Sustain. Energy Rev. 13 (5) (2009) 1014-1026.
[4] Y.P. Chandra, T. Matuska, Stratification analysis of domestic hot water storage tanks: a comprehensive review, Energy Build. 187 (2019) 110-131.
[5] A. Castell, M. Medrano, C. Sole, L.F. Cabeza, Dimensionless numbers used to characterize stratification in water tanks for discharging at low flow rates, Renew. Energy 35 (10) (2010) 2192-2199.
[6] Y.P. Chandra, T. Matuska, Numerical prediction of the stratification performance in domestic hot water storage tanks, Renew. Energy 154 (2020) 1165-1179.
[7] Y. Bai, M. Yang, Z. Wang, X. Li, L. Chen, Thermal stratification in a cylindrical tank due to heat losses while in standby mode, Sol. Energy 185 (2019) 222-234.
[8] S. ed-Dın Fertahi, A. Jamil, A. Benbassou, Review on solar thermal stratified storage tanks (STSST): insight on stratification studies and efficiency indicators, Sol. Energy 176 (2018) 126-145.
[9] A. Arteconi, N.J. Hewitt, F. Polonara, State of the art of thermal storage for demand-side management, Appl. Energy 93 (2012) 371-389.
[10] M.R. Assari, H.B. Tabrizi, M.J. Movahedi, Experimental study on destruction of thermal stratification tank in solar collector performance, J. Energy Storage 15 (2018) 124-132.
[11] J.D. Chung, S.H. Cho, C.S. Tae, H. Yoo, The effect of diffuser configuration on thermal stratification in a rectangular storage tank, Renew. Energy 33 (10) (2008) 2236-2245.
[12] Z. Wang, H. Zhang, B. Dou, H. Huang, W. Wu, Z. Wang, Experimental and numerical research of thermal stratification with a novel inlet in a dynamic hot water storage tank, Renew. Energy 111 (2017) 353-371.

[13] B. Kursun, K. Okten, Effect of rectangular hot water tank position and aspect ratio on thermal stratification enhancement, Renew. Energy 116 (2018) 639-646.
[14] Z. Yang, H. Chen, L. Wang, Y. Sheng, Y. Wang, Comparative study of the influences of different water tank shapes on thermal energy storage capacity and thermal stratification, Renew. Energy 85 (2016) 31e44.
[15] W. Yaïci, M. Ghorab, E. Entchev, S. Hayden, Three-dimensional unsteady CFD simulations of a thermal storage tank performance for optimum design, Appl. Therm. Eng. 60 (1-2) (2013) 152-163.
[16] Y. Karlina, Y. Yerdesh, A. Toleukhanov, Y. Belyayev, H. S. Wang, and O. Botella, "Numerical Simulation Study of Thermal Performance in Hot Water Storage Tanks with External and Internal Heat Exchangers," *Energies (Basel)*, vol. 17, no. 22, Nov. 2024, doi: 10.3390/en17225623.
[17] A. L. Nash, A. Badithela, and N. Jain, "Dynamic modeling of a sensible thermal energy storage tank with an immersed coil heat exchanger under three operation modes," *Appl Energy*, vol. 195, pp. 877–889, 2017, doi: 10.1016/j.apenergy.2017.03.092.
[18] K. M. Powell and T. F. Edgar, "An adaptive-grid model for dynamic simulation of thermocline thermal energy storage systems," *Energy Convers Manag*, vol. 76, pp. 865–873, 2013, doi: 10.1016/j.enconman.2013.08.043.
[19] Khikmatov Bekhzod Amonovich, Mirzaev Mirfayz Salimovich, Samiev Kamoliddin A'zamovich, A systematic review on greenhouse type solar dryers, Solar Energy 283 (2024) 113021, 1-43.

UDC: 539.537

INVESTIGATION OF SCATTERING Ne^+ AND Ar^+ IONS FROM BLACK PHOSPHORINE AT THE GLANCING INCIDENCE

Kutliev Uchkun Otoboevich
Professor DSc,Urgench State University named after Abu Rayhan Biruni
uchkunk@mail.ru
Sattarova Onaxon Abdurasulovna
Urgench State Medical institute,
ttaurgfil@umail.uz

Annotatsiya. Ushbu maqolada qora fosforin sirtini kichik burchaklar ostida bombardimon qilayotgan Ne^+ va Ar^+ ionlarining sochilish jarayoni ketma-ket to`qnashuvlar usuli asosida kompyuterda modellashtirilgan. Ushbu sirtdan sochilgan $Ne^+$ va $Ar^+$ ionlarining xarakteristik trayektoriyalari va energetik spektrlari hisoblangan. Sochilgan ionlarning trayektoriyalari qora fosforin sirtida kreslosimon yarim kanal mavjudligini ko`rsatdi. Olingan energiya spektrlarida dastlab ikkita intensiv cho'qqi kuzatildi; ular sirtning atom qatlami hamda yarim kanal tubidan sochilgan ionlarga mos kelishi aniqlangan. Ionlarning tushish burchagining ortishi ularni qo`shni yarim kanallardan socilishiga olib kelishi va ularga tegishli kichik intensivlikga ega bo`lgan cho`qqilar kuzatildi. Olingan natijalar sirt qatlami va uning tuzilishini o`rganishga imkon beradi.

Kalit so'zlar: *kompyuter modellashtirish, ionlarning sochilishi, ion trayektoriyasi, yarim kanal, energeti spektr.*

Аннотация. В данной статье методом последовательных столкновений на компьютере смоделирован процесс рассеяния ионов Ne^+ и Ar^+,

бомбардирующих поверхность чёрного фосфорина под малыми углами. Рассчитаны характеристические траектории и энергетические спектры ионов Ne^+ и Ar^+, рассеянных от этой поверхности. Траектории рассеянных ионов показали наличие на поверхности чёрного фосфорина полуканала типа «кресло» (armchair). В полученных энергетических спектрах изначально наблюдались два интенсивных пика; установлено, что они соответствуют ионам, рассеянным от атомного слоя поверхности и со дна полуканала. Увеличение угла падения ионов приводило к их рассеянию от соседних полуканалов, при этом наблюдались соответствующие им пики с малой интенсивностью. Полученные результаты позволяют изучить поверхностный слой и его структуру.

Ключевые слова: *компьютерное моделирование, рассеяние ионов, траектория иона, полуканал, энергетический спектр.*

Abstract. In this paper, the scattering process of Ne^+ and Ar^+ ions bombarding the surface of black phosphorene at grazing (small) angles is computer-simulated using the binary collision approximation method. The characteristic trajectories and energy spectra of the Ne^+ and Ar^+ ions scattered from this surface are calculated. The trajectories of the scattered ions revealed the presence of an armchair-like semichannel on the black phosphorene surface. Two intense peaks were initially observed in the obtained energy spectra; they were found to correspond to the ions scattered from the surface atomic layer and the bottom of the semichannel. An increase in the angle of incidence led to ion scattering from neighboring semichannels, and peaks with low intensity corresponding to them were observed. The obtained results allow for the characterization of the surface layer and its structure.

Key words: *computer simulation, ion scattering, ion trajectory, semichannel, energy spectrum.*

Introduction

In surface physics and computational materials science, small-angle (grazing incidence) ion scattering is a highly specialized technique used to determine the exact atomic topography, crystal structural configurations, and defect formations of 2D materials and single-crystal surfaces. When low-energy ions (such as Ne^+ or Ar^+) bombard a crystalline surface at small grazing angles (ψ=1-15^0), they do not penetrate deep into the material. Instead, they glide along the surface atomic rows, interacting via semichannels (like the armchair or zigzag tracks found in phosphorene allotropes). This behavior generates distinct energy spectra and trajectory focus shifts that map out the target's precise atomic layout[1-2].

Black phosphorene is a one-atom-thick layer of black phosphorus. Unlike flat graphene, it has a puckered or wrinkled structure. This unique shape creates small channels on its surface that look like the arms of a called armchair channels. Because of this wrinkled design, electricity and heat move through it at different speeds depending on the direction. Unlike graphene, black phosphorene has a natural bandgap, which means it can be turned on and off like a regular computer switch. Its bandgap changes depending on how many layers it has, allowing it to absorb a wide range of light. This

makes it perfect for fast electronics, infrared night-vision sensors, lasers, and next-generation batteries.Its main weakness is that it is highly unstable in air. It reacts quickly with oxygen and moisture, so scientists must protect it with special coatings to prevent it from breaking down[3-6].

In this paper, we presents the characteristic trajectories of scattered Ne^+ and Ar^+ ions from the black phosphorine surface at small angles of incidence.

Research Methodology

The method of binary collision approximation (BCA) method is widely used in plasma physics, physical chemistry, molecular dynamics, and related fields. It was used to analyze interactions between particles in complex systems where full modeling of all possible interactions is impossible due to computational limitations [7]. This method are based on the assumption that paired particle collisions play a key role in the dynamics of a multicomponent system. Instead of taking into account all interactions simultaneously, only collisions between two particles are considered, ignoring their interaction with the rest of the system during this collision. In this method, the forces, trajectories, and other parameters for each pair of particles are calculated based on the selected potential. Parameters describing collisions are averaged over the entire system to account for the contribution from a large number of particles. Paired collisions are used to obtain analytical or numerical results that approximate the dynamics of the entire system.

In this paper, we used the Ziegler-Birzak-Littmark potential. The Ziegler-Biersack-Littmark (ZBL) potential is a mathematical formula used in physics to describe how atoms repel each other when they collide. It is the most widely used formula in computer simulations for tracking how ions bounce off surfaces. It is called a "universal" potential because it works for almost any combination of atoms in the periodic table, at both low and high speeds. Inelastic energy losses were calculated using the equation of Kishinevsky [8-9].

Analysis and results

Figure 1 shows the scheme of semichannels formed on the surface black phosphorine. CdSe(001)<110> surface. The form this semichannel look like armchair.

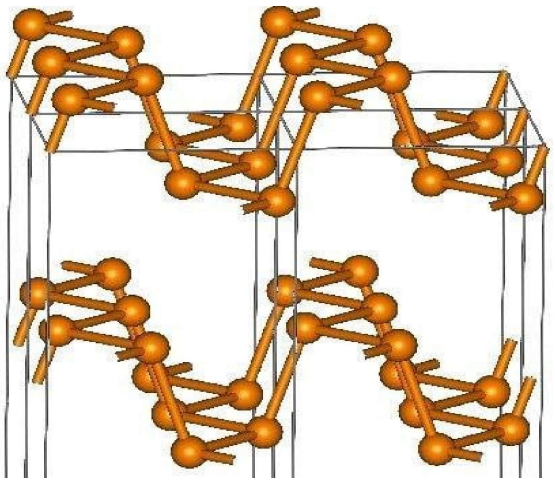

Figure 1. *Semichannel formed on the surface black phosphorine*

Figure 2 shows the energy spectra of Ne^+ ions scattered from the black phosphorene surface at an initial energy of **E_0 = 1 keV** and i at the angle of incidence **ψ = 3°–15°.** As mentioned above, at a relatively low initial energy **(E_0 = 1 keV)** and small incidence angles **(ψ = 3°–7°)**, the energy spectrum consists of a single peak. This indicates that only ions scattered from the surface atomic rows contribute to the observed peak (figure 2a).

Similarly, at the same initial energy and at the angle of incidence ψ = **9°–11°**, a single-peak energy spectrum is observed (figure 2b). However, the peak is shifted toward lower energies because the ions penetrate into the semichannel on the surface. At the **ψ = 9°–11°,** the energy spectrum covers a broader energy range, indicating that the ions penetrate not only between the surface atomic rows and into the semichannel, but also into the region between two adjacent atomic rows on the surface.

Figure 3 presents the trajectories of Ne^+ ions with an initial energy of **E_0 = 1 keV** at the angle of incidence **ψ = 3°, 7° and 15°**. At an incidence of angle **ψ = 3°**, the ions are scattered from the surface atomic rows and the walls of the semichannel, as can be seen in figure 3a. This explains the appearance of a single peak in the corresponding energy spectrum. When the angle of incidence increases to **ψ = 7°**, the trajectories indicate that the ions are also scattered from the atomic row located at the bottom of the semichannel (figure 3b).

a b

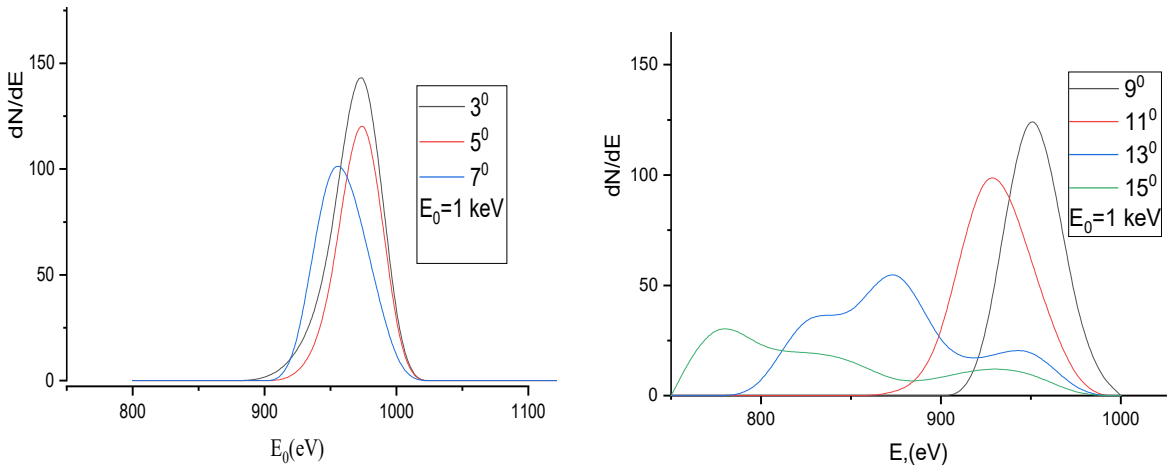

Figure 2. Energy spectra of Ne^+ ions with initial energy E_0=1 keV and at the angle of incidences ψ=3^0-15^0.

However, ions scattered from the surface atomic rows can also be clearly identified from the trajectories. It should be noted that we also observed ions penetrating into the very narrow space between two adjacent atomic rows on the surface. This is evidenced by the increased density of ion trajectories in this region. Consequently, at this incidence angle, the energy distribution of the scattered ions is slightly shifted toward lower energies. At the angle of incidence **ψ = 15°** (figure 3c), the ions exhibit more complex scattering behavior. In particular, the ions are scattered from two atomic rows on the surface, penetrate into the region between these two rows, undergo scattering from the wall of the semichannel, and are subsequently scattered from the atomic row at the bottom of the semichannel.

a b

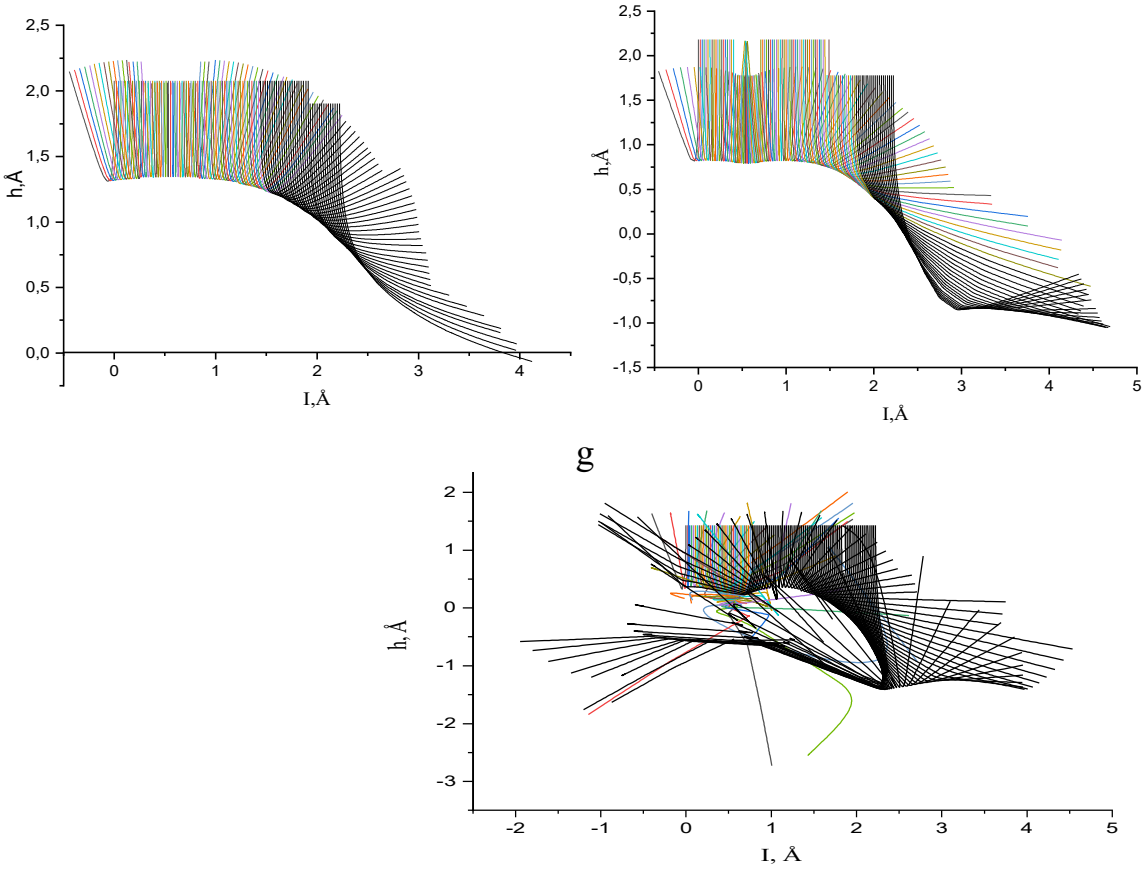

Figure 3. Trajectories of Ne^+ ions with initial energy E_0=1 keV and at the angle of incidences $\psi=3^0$, 7^0 and 15^0.

Some ions are backscattered from the atomic row at the bottom of the semichannel and subsequently enter the adjacent channel. As a result, the energy spectrum at this incidence angle exhibits a broad spectral feature extending over a relatively wide energy range at lower energies.

Figure 4 presents the energy spectra of Ar^+ ions scattered from the black phosphorene surface at an initial energy of **E_0 = 1 keV** and at the angle of incidence **ψ = 3° -15°**. At **ψ = 3°–7°** (figure 4a), the energy spectrum consists of a single peak. A single-peak spectrum is also observed at **ψ = 9°–11°** (figure 4b). However, at **ψ = 13°–15°**, a two-peak spectrum is observed, with the peak at lower energies extending over a broader energy range. **Figure 5** presents the trajectories of Ar^+ ions with an initial energy of **E_0 = 1 keV** at incidence angles of **ψ = 3°, 7° and 15°.** At the angle of incidence **ψ = 3°**, the ions are observed to be scattered from the surface atomic rows and the walls of the semichannel (figure 5a). No collisions with the atomic row located at the bottom of the semichannel are observed. At the **ψ = 7°** (figure 5b), the ion trajectories clearly reproduce the geometry of the semichannel on the black phosphorene surface. In this case, the ions are also scattered from the atomic row at the bottom of the semichannel. It should also be noted that Ar^+ ions are scattered from the atoms in the surface atomic rows at relatively larger distances compared with Ne^+ ions. Consequently, Ar^+ ions penetrate to a smaller extent into the region between the two surface atomic rows than the lighter Ne^+ ions.

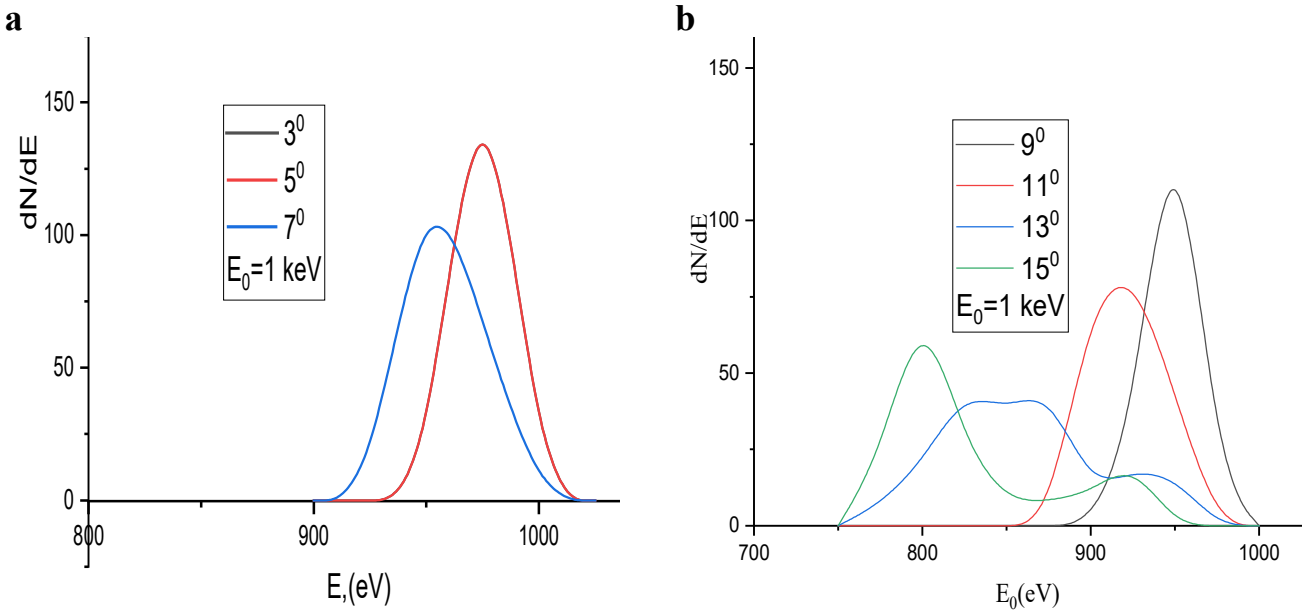

Figure 4. Energy spectra of Ar^+ ions with initial energy E_0=1 keV and at the angle of incidences $\psi=3^0$-15^0.

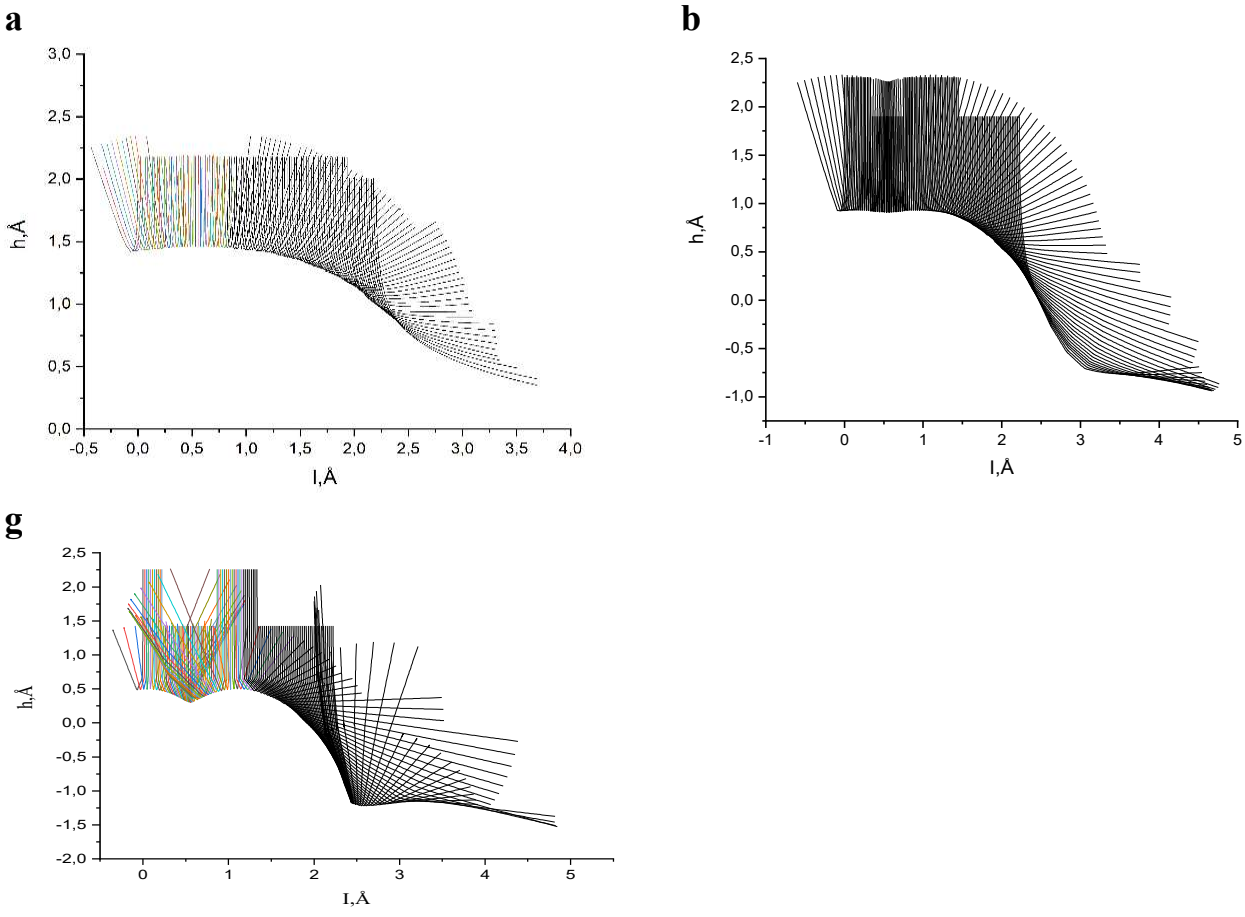

Figure 5. Trajectories of Ar^+ ions with initial energy E_0=1 keV and incidence angles $\psi=3^0$, 7^0 and 15^0.

Conclusion and Recommendations

We have studied the energy distributions and characteristic trajectories of scattered Ar^+ and Ar^+ ions from the surface black phophorine at the angles of incidence $\psi=3^0,5^0,7^0$ and at the initial energy E_0=1keV. The observation of a single peak in the energy spectrum is due to the scattering of ions from both the surface atomic row and the semichannel wall. With the increase in both the angle of incidence and energy, the full geometry of the surface semichannel can be resolved, leading to a multi-peak distribution in the spectrum. As the energy and incident angle increase, the light-mass ion is observed to penetrate between two adjacent atomic rows on the surface.

References

[1]. Niehus.H,Werner Heiland.W,Taglauer E. “Low-energy ion scattering at surfaces”,Surface Science Reports 17:213-304. 1993,pp.215-280. https://doi.org/10.1016/0167-5729(93)90024-J

[2]. Umirzakov. B.E, Tashmukhamedova. D.A, Ruzibaeva. M.K, Djurabekova F.G, Danaev S.B, “Investigation of change of the composition and structure of the CaF2/Si films surface at the low-energy bombardment”, Nuclear Instruments and Methods in Physics Research, Section B: Beam Interactions with Materials and Atoms, 2014. 326, pp. 322–325. https://doi.org/10.1016/j.nimb.2013.10.094

[3]. Han L, Neal A.T, Zhu Z, Xu L, and Ye P.D, “Phosphorene: An Unexplored 2D Semiconductor with a High Hole Mobility”, ACS Nano,2014, 8(4).pp 4033–4041. https://doi.org/10.1021/nn501226z

[4]. Liu H, Neal A.T, Zhu Z, Tomanek D, Ye P.D, “Phosphorene: A New 2D Material with High Carrier Mobility”, arXiv:1401.4133. https://doi.org/10.48550/arXiv.1401.4133

[5]. Ling X , Wang H, Huang Sh, Xia F, and Dresselhaus M.S, “I The renaissance of black phosphorus”, Proceedings of the National Academy of Sciences 2015.112(15) .pp.4523-4530. https://doi.org/10.1073/pnas.1416581112

[6]. Mishra M.R, Gadore V, Chavda V, PandaSh, Roy S, Sahoo P, Pradhan L, Rai H, Pandey Sh.S, Ahmaruzzaman M, “O Black phosphorene: A versatile allotrope revolutionizing environmental, energy, and biomedical applications”, Coordination Chemistry Reviews, 2024. 524. 216345. https://doi.org/10.1016/j.ccr.2024.216345

[7]. O‘connor. D.J, Biersack J.P, “Comparison of theoretical and empirical potentials”, Nuclear Instruments and Methods in Physics Research Section B: Beam Interactions with Materials and Atoms. 1986. 15(1-6). pp.14-17. https://doi.org/10.1016/0168-583X(86)90243-0

[8]. Biersack, J.P., Ziegler, J.F. (1982). The Stopping and Range of Ions in Solids. In: Ryssel, H., Glawischnig, H. (eds) Ion Implantation Techniques. Springer Series in Electrophysics, vol 10. Springer, Berlin, Heidelberg. https://doi.org/10.1007/978-3-642-68779-2_5

[9]. Kishinevsky L M 1962 Izv. Acad. Nauk SSSR Ser. Fiz. 26 1410.

UDK 533.9:546.11

NONTHERMAL PLASMA APPLICATION TO HYDROGEN PRODUCTION

Maftuna Madrimova
Physics Teacher, Secondary School No. 9, Yangibazar District, Khorezm Region
adilbekovnamaftuna360@gmail.com
Jakhongir Matyakubov
Institute of Material Sciences, Academy of Sciences of the Republic of Uzbekistan

Annotatsiya. Nothermal plazma (NTP — nonthermal plasma) vodorod ishlab chiqarishning elektr energiyasi asosida amalga oshiriladigan istiqbolli usullaridan biri sifatida tadqiq etilmoqda. Buning asosiy sababi shundaki, energetik elektronlar butun gaz fazasini termokimyoviy muvozanat holatiga keltirishni talab qilmagan holda metan, suv bug‘i va karbonat angidrid molekulalarini faollashtirish imkonini beradi. Mazkur maqolada dielektrik to‘siqli razryad (DBD — dielectric barrier discharge), sirpanma yoy (gliding arc) va mikroto‘lqinli plazma tizimlari metanning konversiya darajasi, vodorod chiqishi hamda elektr energiyasiga bo‘lgan ehtiyoj nuqtayi nazaridan qiyosiy tahlil qilingan. Nashr etilgan eksperimental natijalar umumiy ko‘rsatkichlar majmuasi, jumladan, xomashyoning konversiya darajasi, H_2 ning chiqishi va selektivligi, solishtirma energiya sarfi hamda vodorod olishning energiya samaradorligi asosida baholangan. Adabiyotlar tahlili reaktor turi va ish rejimi jarayon samaradorligini sezilarli darajada belgilashini ko‘rsatdi. DBD plazma-katalitik tizimlarni integratsiyalash uchun qulay bo‘lsa, sirpanma yoy nisbatan maqbul energiya sarfi sharoitida yuqori konversiya darajasini ta’minlashi mumkin. Mikroto‘lqinli plazma tizimlarida esa yuqori unumdorlikka ega vodorod ishlab chiqarish jarayonlari namoyish etilgan. Katalizatorlardan foydalanish konversiya darajasini oshirishi mumkin, biroq metan konversiyasidagi o‘sish har doim ham H_2 chiqishining mutanosib ravishda ortishiga olib kelmaydi. Shu sababli tahlil natijalari energiya samaradorligi, plazma–katalizator o‘zaro ta’siri, texnologiyani sanoat miqyosiga kengaytirish va mahsulotlarni ajratish jarayonlarini mazkur texnologiyaning asosiy muhandislik cheklovlari sifatida belgilaydi. Eng istiqbolli rivojlanish yo‘nalishi optimallashtirilgan razryad sharoitlari, selektiv katalizatorlar va kam uglerodli elektr energiyasidan foydalanishni yagona tizimga integratsiyalashdan iborat.

Kalit so‘zlar: *nothermal plazma, vodorod ishlab chiqarish, metan konversiyasi, DBD, sirpanma yoy, mikroto‘lqinli plazma, plazma katalizi, energiya samaradorligi.*

Аннотация. Неравновесная плазма (NTP — nonthermal plasma) рассматривается как перспективный способ производства водорода с использованием электрической энергии, поскольку высокоэнергетические электроны позволяют активировать молекулы метана, водяного пара и диоксида углерода без необходимости доведения всей газовой фазы до состояния термохимического равновесия. В статье проведён сравнительный анализ систем на основе диэлектрического барьерного разряда (DBD — dielectric barrier discharge), скользящей дуги (gliding arc) и микроволновой плазмы с особым вниманием к конверсии метана, выходу водорода и

потреблению электрической энергии. Опубликованные экспериментальные результаты оценивались с использованием единого набора показателей, включающего степень конверсии исходного сырья, выход и селективность по H_2, удельные энергетические затраты и энергетический выход водорода. Анализ научной литературы показывает, что тип реактора и режим его эксплуатации оказывают существенное влияние на эффективность процесса. DBD представляет значительный интерес для интеграции плазмы с каталитическими системами, скользящая дуга способна обеспечивать высокую степень конверсии при относительно благоприятных энергетических затратах, тогда как микроволновые плазменные системы продемонстрировали возможность высокопроизводительного производства водорода. Добавление катализаторов может повышать степень конверсии, однако увеличение конверсии метана не обязательно приводит к пропорциональному повышению выхода H_2. В связи с этим результаты анализа позволяют выделить энергетическую эффективность, взаимодействие плазмы с катализатором, масштабирование технологии и разделение продуктов как основные инженерные ограничения данной технологии. Наиболее перспективным направлением дальнейшего развития является интеграция оптимизированных условий разряда, селективных катализаторов и низкоуглеродной электроэнергии.

Ключевые слова: *неравновесная плазма, производство водорода, конверсия метана, DBD, скользящая дуга, микроволновая плазма, плазменный катализ, энергетическая эффективность.*

Abstract. Nonthermal plasma (NTP) is being investigated as an electrically driven route for hydrogen production because energetic electrons can activate methane, water vapour and carbon dioxide without requiring the entire gas phase to reach thermochemical equilibrium. This article compares dielectric barrier discharge (DBD), gliding arc and microwave plasma systems, with particular attention to methane conversion, hydrogen yield and electrical energy demand. Published experimental results were evaluated using a common set of indicators: feed conversion, H_2 yield/selectivity, specific energy input and hydrogen energy yield. The literature shows that reactor type and operating regime strongly determine performance. DBD is attractive for plasma-catalyst integration, gliding arc can provide high conversion at relatively favourable energy input, and microwave systems have demonstrated high-throughput hydrogen production. Catalyst addition can enhance conversion, but the gain in methane conversion does not necessarily translate proportionally into H_2 yield. The analysis therefore identifies energy efficiency, plasma-catalyst interaction, scale-up and product separation as the principal engineering constraints. The most promising development route is the integration of optimized discharge conditions, selective catalysts and low-carbon electricity.

Key words: *nonthermal plasma, hydrogen production, methane conversion, DBD, gliding arc, microwave plasma, plasma catalysis, energy efficiency*.

Introduction

Hydrogen is an important feedstock for ammonia synthesis, petroleum refining and emerging low-carbon energy systems. Its environmental value, however, is determined primarily by the production route. Conventional steam methane reforming is technologically mature, but it is energy intensive and produces carbon dioxide unless carbon capture is incorporated. This has stimulated research into electrically driven processes that can operate flexibly with renewable power.

Nonthermal plasma is a nonequilibrium ionized medium in which electrons can attain substantially higher energies than the bulk gas. Electron-impact excitation and dissociation generate radicals and excited species that initiate reactions at conditions different from conventional thermal chemistry. For methane, the first activation step can be represented schematically as $e^- + CH_4 \rightarrow CH_3\bullet + H\bullet + e^-$, followed by radical recombination and surface reactions leading to H_2. Water-containing systems additionally generate H• and OH• species. These pathways make NTP relevant to methane decomposition, steam reforming and dry reforming [2,3].

The principal reactor families investigated for hydrogen production include DBD, gliding arc and microwave plasma. DBD operates near atmospheric pressure and is readily combined with catalyst packing. Gliding arc provides a higher power density and often a larger conversion window, while microwave plasma can sustain high-density discharges without direct electrode contact. Recent work also emphasizes plasma-catalyst coupling, because catalyst surfaces can alter local electric fields and reaction pathways, while plasma-generated excited species can modify adsorption and surface kinetics [4,10].

The present study aims to compare these approaches using performance indicators that are directly relevant to hydrogen production. The central premise is that high feed conversion alone is insufficient: a practical process must also deliver favourable H_2 yield and selectivity at acceptable electrical energy consumption. Accordingly, the analysis focuses on conversion, hydrogen productivity, specific energy input, energy yield, catalyst effects and scale-up.

Research Methodology

The work was conducted as a comparative analysis of peer-reviewed experimental and review studies on plasma-assisted hydrogen production. Publications addressing methane decomposition, steam/dry reforming and plasma-catalytic conversion were selected, with emphasis on DBD, gliding arc and microwave systems. Because the literature uses different feed compositions, reactor volumes and power bases, numerical values were treated as representative results rather than as strictly equivalent measurements.

Four indicators were used. Methane conversion was defined as $XCH_4 = (Fin - Fout)/Fin \times 100$. Hydrogen yield was interpreted according to the definition used in each source. Specific energy input (SEI) was evaluated as electrical power divided by gas flow rate, while hydrogen energy yield was expressed as mass of H_2 produced per unit of electrical energy (g H_2/kWh). Where reported values were based on different definitions, they were not combined into a single normalized ranking.

The comparison also considered reactor configuration, catalyst compatibility, gas temperature, throughput and dominant engineering limitation. Particular attention was paid to Ni-based catalytic systems because nickel is widely used for C–H activation and reforming, although carbon deposition and deactivation remain important constraints.

To characterize the recent development tendency without presenting an unsupported database-wide bibliometric claim, a descriptive temporal evidence map was also prepared from the 25 peer-reviewed and scholarly sources included in the final reference set. Publication years were counted cumulatively for 2016–2026. This curve is therefore a visualization of the evidence base used in this article, not a Scopus or Web of Science publication-count series. The interpretation is cross-checked against recent reviews reporting intensified research activity and increasing attention to scale-up, energy efficiency and carbon valorization [23,25].

Table 1. Comparative characteristics of plasma systems used for hydrogen production

System	Operating feature	Main advantage	Catalyst integration	Main limitation
DBD	Nonequilibrium, often atmospheric	Low bulk-gas temperature; simple geometry	Excellent	Energy efficiency; discharge nonuniformity
Gliding arc	Transitional nonthermal/thermal regime	High conversion and power density	Moderate	Thermal management
Microwave plasma	High-density, electrode-free discharge	High throughput; rapid activation	Moderate	Power-system complexity
Plasma-catalyst hybrid	Discharge coupled with solid catalyst	Potential selectivity/conversion synergy	Intrinsic	Complex plasma-surface interaction

Sources for Table 1: [10]; [13]; [22]

Results

The reviewed studies show that plasma performance is strongly reactor- and condition-dependent. A recent nonthermal nanosecond plasma reformer reported maximum methane conversion of 60.1% and H_2 production of 33.42% under its optimized operating condition, illustrating that meaningful conversion can be achieved without a conventional catalyst [11]. In DBD systems, catalyst packing can increase or decrease conversion depending on dielectric properties, metal loading and placement; therefore, plasma-catalyst synergy cannot be assumed solely from catalyst addition [10].

Microwave plasma is notable for hydrogen productivity. Czylkowski et al. reported an energy yield of 42.9 g H_2/kWh in combined steam reforming at 2.45 GHz with absorbed power up to 6 kW [5]. A later commercial-scale microwave plasma steam methane reforming study reported an optimum hydrogen production rate of 2247 g H_2/h and an energy yield of about 70 g H_2/kWh [6]. The improvement is significant because it demonstrates that reactor and power-system design can shift the energy performance of the same broad plasma family. DBD remains particularly relevant to plasma catalysis. Reviews of dry reforming show that packing materials can reshape the local electric

field, alter electron energy and change product distribution. Ni/Al_2O_3 and related materials are frequently studied, but the outcome depends on support properties and whether the catalyst is positioned in the discharge or downstream [4,10]. Consequently, catalyst selection must be evaluated together with electrical characteristics rather than as an independent variable.

Table 2. Representative literature results relevant to plasma-assisted hydrogen production

Plasma/process	Reported condition	CH_4 conversion	H_2 performance	Interpretation
Nanosecond NTP reformer	21 W; 2.2 L/min at optimum	60.1%	33.42% H_2 production	Catalyst-free NTP can achieve substantial conversion [11]
Microwave combined steam reforming	2.45 GHz; ≤6 kW; ≤9000 NL/h	Source-specific	42.9 g H_2/kWh	Stable operation at high gas flow [5]
Microwave PSMR	915 MHz; commercial-scale torch	Source-specific	2247 g H_2/h; ~70 g H_2/kWh	Higher energy yield demonstrated at scale [6]
DBD + catalyst	Packed/in-plasma configurations	Highly variable	Highly variable	Packing can enhance or suppress performance [10]

Sources for Table 2: [5]; [6]; [10]; [11]

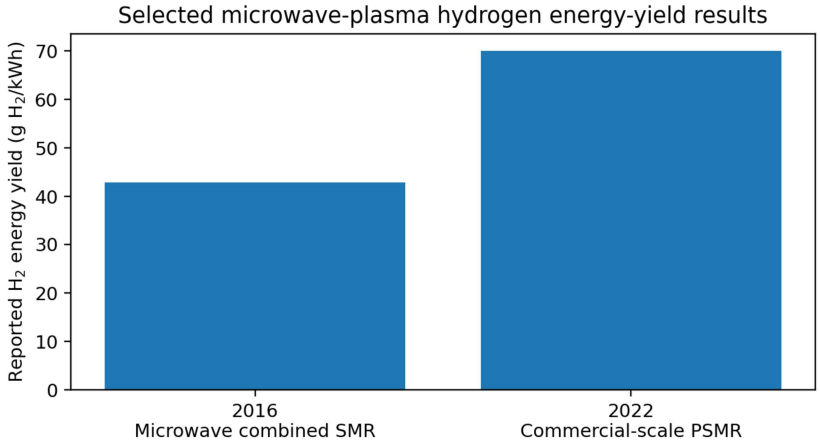

Figure 1. Reported hydrogen energy yield in two microwave plasma studies [5,6].

Sources for Figure 1: Czylkowski et al. (2016); Akande&Lee (2022)

Figure 1 should not be interpreted as a controlled head-to-head experiment because the two studies used different microwave frequencies, reactor designs and scales. It is nevertheless useful as an engineering comparison: published energy yield increased from 42.9 to approximately 70 g H_2/kWh, indicating that plasma-source design and process intensification materially affect hydrogen output per unit of absorbed electrical energy. Across the reactor classes, a recurring trade-off is observed between conversion and energy efficiency. Raising discharge power generally increases the probability of electron-impact activation and therefore conversion, but the additional energy may

increasingly be lost through gas heating, nonproductive excitation or secondary chemistry. The optimum operating point can therefore occur below the maximum attainable conversion. This is particularly important when plasma systems are compared with electrolysis or conventional reforming.

Temporal development of plasma-assisted hydrogen research

The chronology of the selected literature shows a clear broadening of plasma-assisted hydrogen research. Early work in the evidence set emphasized proof-of-concept microwave and DBD conversion, whereas later studies increasingly address catalyst synergy, commercial-scale microwave reforming, techno-economic assessment, process optimization, lifecycle performance and reactor scale-up. This development does not prove a universal year-by-year increase in global deployment, but it does document a transition from laboratory conversion studies toward engineering and systems-level evaluation [5,6,19,23–25].

Table 3. Selected development milestones in plasma-assisted hydrogen production, 2016–2026

Year	Representative development	Evidence/source
2016	High-flow microwave combined steam reforming; 42.9 g H_2/kWh reported	[5]
2017	DBD plasma-catalyst methane conversion and partial oxidation demonstrated	[15,20]
2020	DBD methane cracking and pulsed plasma-catalyst optimization expanded	[10,16,17]
2021	Microwave liquid-phase reforming and electron-beam plasma TEA/LCA-oriented assessment	[18,19]
2022	Commercial-scale distributed microwave PSMR;>70 g H_2/kWh reported	[6]
2023	Direct comparison of microwave and gliding-arc methane pyrolysis	[13]
2024	Rapid growth of reactor/catalyst optimization, process intensification and methane-pyrolysis reviews	[2–4,9,11,14]
2025	Detailed diagnostics, kinetic/catalyst-design studies and system trade-off analysis	[1,7,8,12,23]
2026	DBD reactor optimization and dedicated plasma-assisted methane-pyrolysis scale-up reviews	[24,25]

Sources for Table 3 (selected DOI links): [5]; [6]; [14]; [23]; [24]; [25]

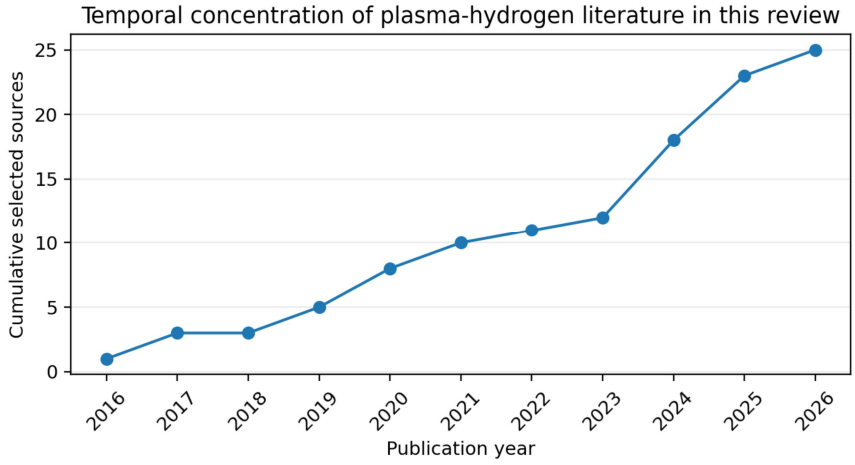

Figure 2. Temporal concentration of representative plasma-hydrogen literature included in this review (2016–2026).

Data basis and verification for Figure 2: 25-source reference set in this article; OpenAlex grouping methodology (for bibliometric context only)

Note. Figure 2 is a descriptive map of the publication years of the 25 sources selected for this article. It is not a Scopus, Web of Science or OpenAlex database-wide publication count and therefore should not be interpreted as a direct measure of industrial adoption. It shows increasing concentration of the reviewed evidence in 2024–2026; this interpretation is consistent with recent reviews describing intensified research, reactor optimization, scale-up and carbon valorization in plasma-assisted methane pyrolysis [23,25].

Discussion

The results indicate that NTP should be evaluated as an energy-conversion technology rather than simply as a chemical activation method. DBD offers a practical platform for plasma catalysis because catalyst particles can be placed directly in the discharge gap. At the same time, dielectric packing modifies the discharge itself; local field enhancement, microdischarge formation and surface charging may alter both electron kinetics and catalytic chemistry. This explains why apparently similar Ni-based systems can produce different outcomes [4,10].

Gliding arc and microwave systems address a different engineering objective. Their higher power density can support larger throughputs and stronger molecular activation. Microwave plasma, in particular, has demonstrated energy yields of 42.9 g H_2/kWh and approximately 70 g H_2/kWh in published steam-reforming systems [5,6]. These values show progress, but they do not remove the need to account for auxiliary power, feed preparation and downstream purification when evaluating overall process efficiency.

The choice of reaction route is equally important. Direct methane decomposition ($CH_4 \rightarrow C + 2H_2$) avoids direct CO_2 formation in the principal reaction and produces solid carbon as a coproduct. Steam reforming offers a higher stoichiometric H_2 potential but generates carbon oxides, whereas dry reforming converts CH_4 and CO_2 simultaneously and primarily produces syngas. Thus, the preferred plasma route depends on whether the target is pure hydrogen, syngas, carbon valorization or greenhouse-gas conversion [2,3,9].

Plasma-catalyst integration is promising but remains scientifically complex. Conventional catalysts were developed for thermal equilibrium conditions, while plasma exposes surfaces to radicals, ions, photons, vibrationally excited molecules and transient electric fields. Future catalyst design should therefore consider dielectric properties and plasma-surface coupling in addition to conventional activity and stability. Ni-based materials remain useful benchmarks, but resistance to coking and sintering is essential for continuous operation. Industrial implementation also requires scale-up without losing discharge uniformity. For DBD, simple geometric enlargement can change microdischarge density and residence-time distribution; modular numbering-up may therefore be more reliable. Microwave systems can handle larger gas flows but require efficient generators, impedance matching and thermal management. In all cases, H_2 purification can impose an additional energy penalty when CO, CO_2, residual CH_4 or higher hydrocarbons are present. A further methodological issue is the lack of uniform reporting. Studies often use different definitions for H_2 yield, energy efficiency and SEI,

which can make numerical comparisons misleading. Future experiments should report electrical input, absorbed power, feed composition, flow rate, residence time, conversion, H_2 production rate, energy yield and carbon balance under clearly defined conditions. Such reporting would allow meaningful techno-economic and life-cycle comparisons.

Overall, the evidence supports a development strategy based on optimized pulsed or microwave power delivery, plasma-specific catalyst design and low-carbon electricity. The principal target should not be maximum single-pass conversion, but the highest stable hydrogen productivity at the lowest practical specific electrical energy consumption.

Conclusion and Recommendations

Nonthermal plasma provides a flexible platform for hydrogen production through methane decomposition and reforming. DBD is particularly suitable for plasma-catalyst studies, while gliding arc and microwave systems offer higher power density and potentially greater throughput. Published microwave-plasma studies demonstrate that hydrogen energy yield can be improved substantially through reactor and process optimization. However, conversion alone is not an adequate measure of performance; H_2 yield, selectivity, specific energy consumption, product purity and reactor stability must be assessed together.

The most important barriers to practical deployment are electrical energy demand, nonuniform scale-up, catalyst deactivation and downstream separation. The strongest research direction is therefore an integrated system combining optimized plasma generation, selective and durable catalysts, renewable electricity and efficient H_2 separation. Standardized reporting of energy and conversion metrics is also necessary before different plasma technologies can be compared reliably.

References

[1]. Sanna A., Openshaw D., Oghotomo P., Bagnato G. Steam reforming of methane: state of the art and novel technologies. Reaction Chemistry & Engineering. 2025;10:1963–1977. https://doi.org/10.1039/D5RE00001G

[2]. Wang K., Ren X., Yin G., Hu E., Zhang H. Recent advances in plasma-based methane reforming for syngas production. Current Opinion in Green and Sustainable Chemistry. 2024; article 100981. https://doi.org/10.1016/j.cogsc.2024.100981

[3]. Yuan X., Sun J., Ma Y., Wang Y., Liu B., Cai Y., Yong X., Tu X. A kinetic study of nonthermal plasma pyrolysis of methane: Insights into hydrogen and carbon material production. Chemical Engineering Journal. 2024;499:156396. https://doi.org/10.1016/j.cej.2024.156396

[4]. Cai Y., Mei D., Chen Y., Bogaerts A., Tu X. Machine learning-driven optimization of plasma-catalytic dry reforming of methane. Journal of Energy Chemistry. 2024;96:153–163. https://doi.org/10.1016/j.jechem.2024.04.022

[5]. Czylkowski D., Hrycak B., Jasiński M., Dors M., Mizeraczyk J. Microwave plasma-based method of hydrogen production via combined steam reforming of methane. Energy. 2016;113:653–661. https://doi.org/10.1016/j.energy.2016.07.088

[6]. Akande O., Lee B.J. Plasma steam methane reforming (PSMR) using a microwave torch for commercial-scale distributed hydrogen production. International Journal of Hydrogen Energy. 2022;47(5):2874–2884. https://doi.org/10.1016/j.ijhydene.2021.10.258

[7]. Kreuznacht S., Böke M., von Keudell A. Space-resolved gas temperature of a microwave plasma torch used for hydrogen production via methane pyrolysis. Plasma Processes and Polymers. 2025;22:e2400089. https://doi.org/10.1002/ppap.202400089

[8]. Facas G.G., Calabrese G., Schüller N., Schreiber D., Zennegg M., Radoiu M., Dimopoulos Eggenschwiler P. Hydrogen production by microwave plasma CH_4 pyrolysis: Characterization via optical emission spectroscopy and response surface methodology. International Journal of Hydrogen Energy. 2025;157:150436. https://doi.org/10.1016/j.ijhydene.2025.150436

[9]. Fulcheri L., Dames E., Rohani V. Plasma-based conversion of methane into hydrogen and carbon black. Current Opinion in Green and Sustainable Chemistry. 2024;50:100973. https://doi.org/10.1016/j.cogsc.2024.100973

[10]. Abiev R.S., Sladkovskiy D.A., Semikin K.V., Murzin D.Y., Rebrov E.V. Non-Thermal Plasma for Process and Energy Intensification in Dry Reforming of Methane. Catalysts. 2020;10(11):1358. https://doi.org/10.3390/catal10111358

[11]. Niknezhad S.S., Staack D., Pistikopoulos E.N. Natural gas to hydrogen via a novel process intensified plasma-based reformer. Applied Energy. 2024;373:123911. https://doi.org/10.1016/j.apenergy.2024.123911

[12]. Shen M., Guo W., Tong L., Wang L., Chu P.K., Kawi S., Ding Y. Non-thermal plasma driven dry reforming of methane: electron energy-input power coupling mechanism and catalyst design criteria. Frontiers of Chemical Science and Engineering. 2025;19(9):84. https://doi.org/10.1007/s11705-025-2596-4

[13]. Kreuznacht S., Purcel M., Böddeker S., Awakowicz P., Xia W., Muhler M., Böke M., von Keudell A. Comparison of the performance of a microwave plasma torch and a gliding arc plasma for hydrogen production via methane pyrolysis. Plasma Processes and Polymers. 2023;20(1):e2200132. https://doi.org/10.1002/ppap.202200132

[14]. Garcia-Villalva R., Biset-Peiró M., Alarcón A., Bacariza C., Murcia-López S., Guilera J. Comparison of methane reforming routes for hydrogen production using dielectric barrier discharge plasma-catalysis. International Journal of Hydrogen Energy. 2024;59:1367–1375. https://doi.org/10.1016/j.ijhydene.2024.02.161

[15]. Song L., Kong Y., Li X. Hydrogen production from partial oxidation of methane over dielectric barrier discharge plasma and $NiO/\gamma\text{-}Al_2O_3$ catalyst. International Journal of Hydrogen Energy. 2017;42(31):19869–19876. https://doi.org/10.1016/j.ijhydene.2017.06.008

[16]. Khoja A.H., Azad A.K., Saleem F., Khan B.A., Naqvi S.R., Mehran M.T., Amin N.A.S. Hydrogen Production from Methane Cracking in Dielectric Barrier Discharge Catalytic Plasma Reactor Using a Nanocatalyst. Energies. 2020;13(22):5921. https://doi.org/10.3390/en13225921

[17]. Ghanbari M., Binazadeh M., Zafarnak S., Taghvaei H., Rahimpour M.R. Hydrogen production via catalytic pulsed plasma conversion of methane: Effect of $Ni–K_2O/Al_2O_3$ loading, applied voltage, and argon flow rate. International Journal of Hydrogen Energy. 2020;45(27):13899–13910. https://doi.org/10.1016/j.ijhydene.2020.03.099

[18]. Wang Q., Wang J., Zhu T., Zhu X., Sun B. Characteristics of methane wet reforming driven by microwave plasma in liquid phase for hydrogen production. International Journal of Hydrogen Energy. 2021;46(69):34105–34115. https://doi.org/10.1016/j.ijhydene.2021.08.006

[19]. Kerscher F., Stary A., Gleis S., Ulrich A., Klein H., Spliethoff H. Low-carbon hydrogen production via electron beam plasma methane pyrolysis: Techno-economic analysis and carbon footprint assessment. International Journal of Hydrogen Energy. 2021;46(38):19897–19912. https://doi.org/10.1016/j.ijhydene.2021.03.114

[20]. Chiremba E., Zhang K., Kazak C., Akay G. Direct nonoxidative conversion of methane to hydrogen and higher hydrocarbons by dielectric barrier discharge plasma with plasma catalysis promoters. AIChE Journal. 2017. https://doi.org/10.1002/aic.15769

[21]. Whitehead J.C. Plasma-catalysis: Is it just a question of scale? Frontiers of Chemical Science and Engineering. 2019;13:264–273. https://doi.org/10.1007/s11705-019-1794-3

[22]. Tu X., Whitehead J.C., Nozaki T., editors. Plasma Catalysis: Fundamentals and Applications. Cham: Springer; 2019. https://doi.org/10.1007/978-3-030-05189-1

[23]. Moghaddam A.L., Hejazi S., Fattahi M., Kibria M.G., Thomson M.J., AlEisa R., Khan M.A. Methane pyrolysis for hydrogen production: navigating the path to a net zero future. Energy & Environmental Science. 2025;18:2747–2790. https://doi.org/10.1039/D4EE06191H

[24]. Cao M., Li S., Wang S., Zhou X., Ma G., Chen Y. Enhanced Hydrogen Production via Methane Cracking in a Dielectric Barrier Discharge Plasma Reactor: Structural and Operational Parameter Optimization. Industrial&Engineering Chemistry Research. 2026;65(16):8233–8243. https://doi.org/10.1021/acs.iecr.5c05406

[25]. Sarkinbaka Z.M., Marvin M.K. Towards plasma-assisted methane pyrolysis for hydrogen production: A review. Next Energy. 2026;12:100700. https://doi.org/10.1016/j.nxener.2026.100700

UDC: 533.9.082.5

INVESTIGATION OF PLASMA CHARACTERISTICS PRODUCED ON A BINARY SODIUM CHLORIDE SURFACE

Davletov Ikrom Yusubovich
Professor, Urgench State University named after Abu Rayhan Biruni
Vapayev Murod Ergashovich
Associate *Professor (PhD), Urgench State University named after Abu Rayhan Biruni*
Japakov Azamat Ikrombayevich
Associate *Professor (PhD), Urgench State University named after Abu Rayhan Biruni*
azamat@urdu.uz
Sotimova Mahbuba Qadamoy qizi
Assistant teacher, Urgench State University named after Abu Rayhan Biruni

Annotatsiya: Mazkur tadqiqot qattiq holatdagi natriy xlorid (NaCl) namunasi yuzasiga Nd:YAG lazer impulsli ta`sir ettirilganda hosil bo`ladigan plazma spektroskopikyondashuv asosida tahlil qilindi.Tajribalar 10^{-2} Torr bosimli vakuumda, 1064 nm to`lqin uzunligi va 20 ns impuls davomiyligiga ega lazer yordamida bajarildi.Plazmaning elektron zichligi hamda elektron temperaturasi asosiy diognostik kattaliklar sifatida baholandi.Elektron zichlik spektral chiziqlarning Stark kengayishidan,temperaturasi asosiy diagnostik kattaliklar sifatida baholandi.Elektron zichlik spektral chiziqlarning Stark kengayishidan, temperatura esa Boltsman grafigi usulidan foydalanib topildi. Ushbu ikki kattalikdan kelib chiqib, plazmaning qo‘shimcha fizik parametrlari ham hisoblandi.

Kalit so‘zlar: *LIBS, spektroskopiya, lazer plazmasi, elektronlar zichligi, elektron temperaturasi.*

Аннотация: В исследовании рассмотрена плазма, возникающая при импульсном облучении твердого образца NaCl Nd:YAG-лазером. Измерения выполнены в вакууме при давлении 10^{-2} Torr; использовалось излучение с длиной волны 1064 нм и длительностью импульса 20 нс. По спектрам излучения определены электронная концентрация и температура плазмы. Концентрация электронов оценивалась по штарковскому уширению спектральных линий, а температура — по построению зависимости Больцмана. На основе этих величин дополнительно рассчитаны характеристики исследуемой плазмы.

Ключевые слова: *LIBS, спектроскопия, лазерная плазма, электронная плотность, электронная температура.*

Abstract: The present study examines the plasma produced when a solid NaCl sample is exposed to pulsed Nd:YAG laser radiation. Measurements were performed at a vacuum pressure of 10^{-2} Torr with a 1064 nm laser pulse lasting 20 ns. Emission spectral were used to evaluate two principal plasma quantities: electron density and electron temperature. The electron density was obtained from Stark broadening of selected spectral lines, whereas the temperature was derived from a Boltzmann plot. The resulting values were subsequently used to estimate several additional plasma characteristics.

Key words: *LIBS, spectroscopy, laser plasma, electron density, electron temperature.*

Introduction

Today, laser-induced breakdown spectroscopy (LIBS) is widely used as an elemental spectrochemical analysis method for binary and multi-element alloys. The LIBS method allows the analysis of materials in any aggregate state—gas, liquid, or solid—regardless of form [1–4]. Laser pulses are directed at the sample to atomize a small amount of material, which leads to the formation of a microplasma. The interaction of laser radiation with atoms and electrons produces plasma at high temperatures, and the plasma emits light across various spectral ranges. The plasma light is spectrally analyzed, and based on each element's unique emission spectrum, it makes it possible to determine the sample's elemental composition. LIBS is a convenient method for the quantitative determination of isotopic concentrations of sodium and chlorine. In modern high-performance charge-storage batteries, sodium-chloride-based alloys are of significant importance due to their high energy density and electrochemical properties. With the development of the battery manufacturing industry, the demand for high-tech materials in battery production is steadily increasing. Sodium chloride mixtures are the main component of molten salt mixtures used as both a coolant and a fuel carrier in advanced nuclear reactors [2]. Sodium chloride is used as a radiation shielding material due to its low neutron absorption and excellent thermal properties[2].

Currently, sodium chloride alloys are used for various purposes in fields such as nuclear energy, optics, materials science, and radiation detection, and there is a great need to process and recycle these metals.

Literature Review

Laser ablation (LA) is a well-known technique that can be used in a number of material processing and analytical applications [1, 2]. Those applications include micro-nanostructuring, colorizing of metals, controlling the wetting properties of laser-processes materials [3, 4], laser-induced breakdown spectroscopy (LIBS) [5], nanoparticle production [6], and pulsed laser deposition [7]. These techniques are based on the production of plasma plumes on the target's surface during the interaction with ultrashort laser pulses [8]. Understanding the effects of plasma temperature and electron density is crucial in optimizing the products of the laser ablation of any target. The dependence of the sizedistribution of nanoparticles that are produced during laser ablation on the laser fluence has been previously observed [9]. In addition, LA-based LIBS allows for direct and rapid determination of the elemental composition of materials

through analyzing the parameters of laser-induced plasma, which can in turn be useful for the analysis of LIBS.

Research Methodology

Calculating the parameters of the plasma plumes based on the Stark broadening technique can be also useful in understanding the nature of the LIBS structures formed on the surface [8]. The relation between the ablated plasma parameters and the formed LIBS during the propagation of the plasmonic polaritons (SPP) and their interference with the electric field of the ablating pulses [10]. SPP is a result of the motion of free electrons excited during the ablation process [11]. The correlation between the plasma parameters and morphological characteristics of the ablated surfaces. LIBS analysis revealed that when the laser fluence was increased from 5.2 J cm−2 to 10.4 J cm−2, both electron temperature and electron number density of the plasma was observed to increase due to enhanced energy deposition. At peripheral ablated areas, flakes, cavities, cones and craters with multiple ablated layers were formed. Fluence is one of the main parameters for the modification of surfaces and the generation of laser plasma plumes by femtosecond laser pulses. These two plasma parameters are important to understand,optimize and control the process of ablation, structuring as well as thin film deposition.

Analysis and Results

The objective of this work was to characterize the plasma generated from a binary sodium-chloride material by means of LIBS and to evaluate its principal physical parameters. A solid NaCl sample was irradiated in a 10^{-2} Torr vacuum chamber with an Nd:YAG laser at 1064 nm. Each laser pulse had an energy of 100 mJ and a duration of 20 ns; the focusing lens had a focal length of 25 cm. The emitted radiation was collected and analyzed with an Ocean Optics HR-4000 fiber-optic spectrometer covering approximately 200–1100 nm. The experimental arrangement is presented in Figure 1

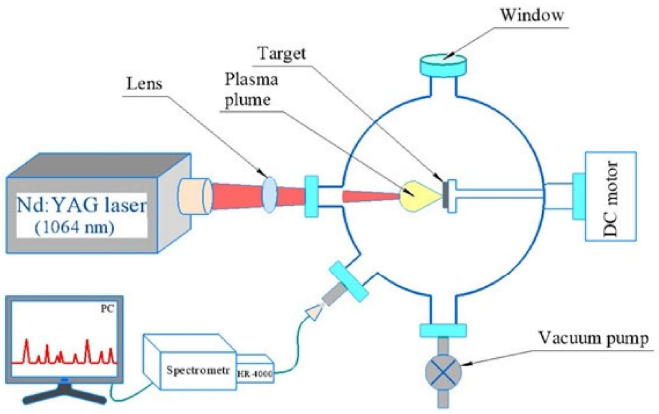

Figure 1. Experimental setup

The recorded emission spectrum contains transitions attributable to neutral and singly ionized sodium and chlorine, corresponding to the I and II charge states (Figure 2). For the selected lines, both their central wavelengths and spectral widths were extracted. These quantities were then used to estimate the free-electron concentration through the Stark-broadening technique.The electron concentrations were evaluated

from the Stark-broadened spectral features. Figure 2 presents the emission spectrum obtained from the NaCl sample.

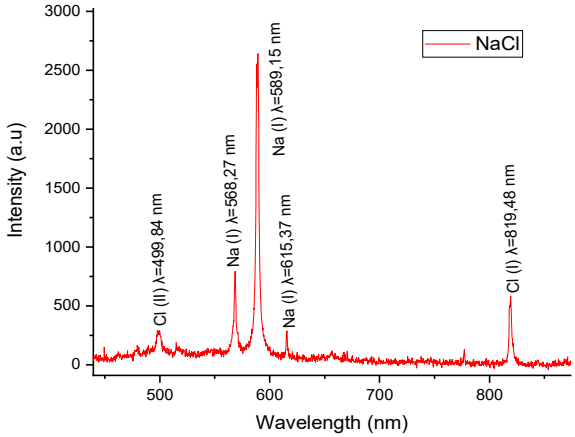

Figure 2. Plasma emission spectrum of the NaCl mixture

The Stark effect refers to the modification, including displacement and splitting, of atomic or molecular energy levels and spectral lines in the presence of an electric field. In a plasma, electric microfields generated by charged particles can therefore alter the observed profile of an emission line. Broadening of a spectral line in a plasma is strongly influenced by collisions involving charged particles. The relation connecting the Stark contribution to the measured full width at half maximum (FWHM) and the electron density can be written as follows:

$$\Delta\lambda_{\frac{1}{2}} = \left[2W\left(\frac{n_e}{10^{16}}\right) + 3{,}5A\left(\frac{n_e}{10^{16}}\right)^{\frac{1}{4}} \cdot \left(1 - \frac{3}{4}N_D^{-\frac{1}{3}}\right) W\left(\frac{n_e}{10^{16}}\right) \right] \overset{0}{\text{A}} \qquad (1)$$

In this expression, ND denotes the number of particles contained in the Debye sphere, A is associated with ion–ion interactions, and W represents the electron interaction parameter. The two terms account for contributions arising from electron and ion interactions. For non-hydrogen-like ions, electron-impact broadening is the dominant Stark contribution, while the ion–ion term can be neglected under the conditions considered here [5–7]. The resulting simplified Stark relation is therefore used for the density evaluation.

$$\Delta\lambda_{\frac{1}{2}} = 2W\left(\frac{n_e}{10^{16}}\right) \overset{0}{\text{A}}. \qquad (2)$$

Here, FWHM denotes the measured spectral width and ne is the electron density. The spectra of Na^+ and Cl^- transitions in the I and II ionization states were used to obtain density values for the selected wavelengths (Table 1). Each FWHM value was obtained by fitting the corresponding line profile with a Gaussian function (Figure 3). Where neighboring transitions overlapped, the individual components were resolved before fitting. The electron-impact parameter W was taken from the tabulated data reported in [5].

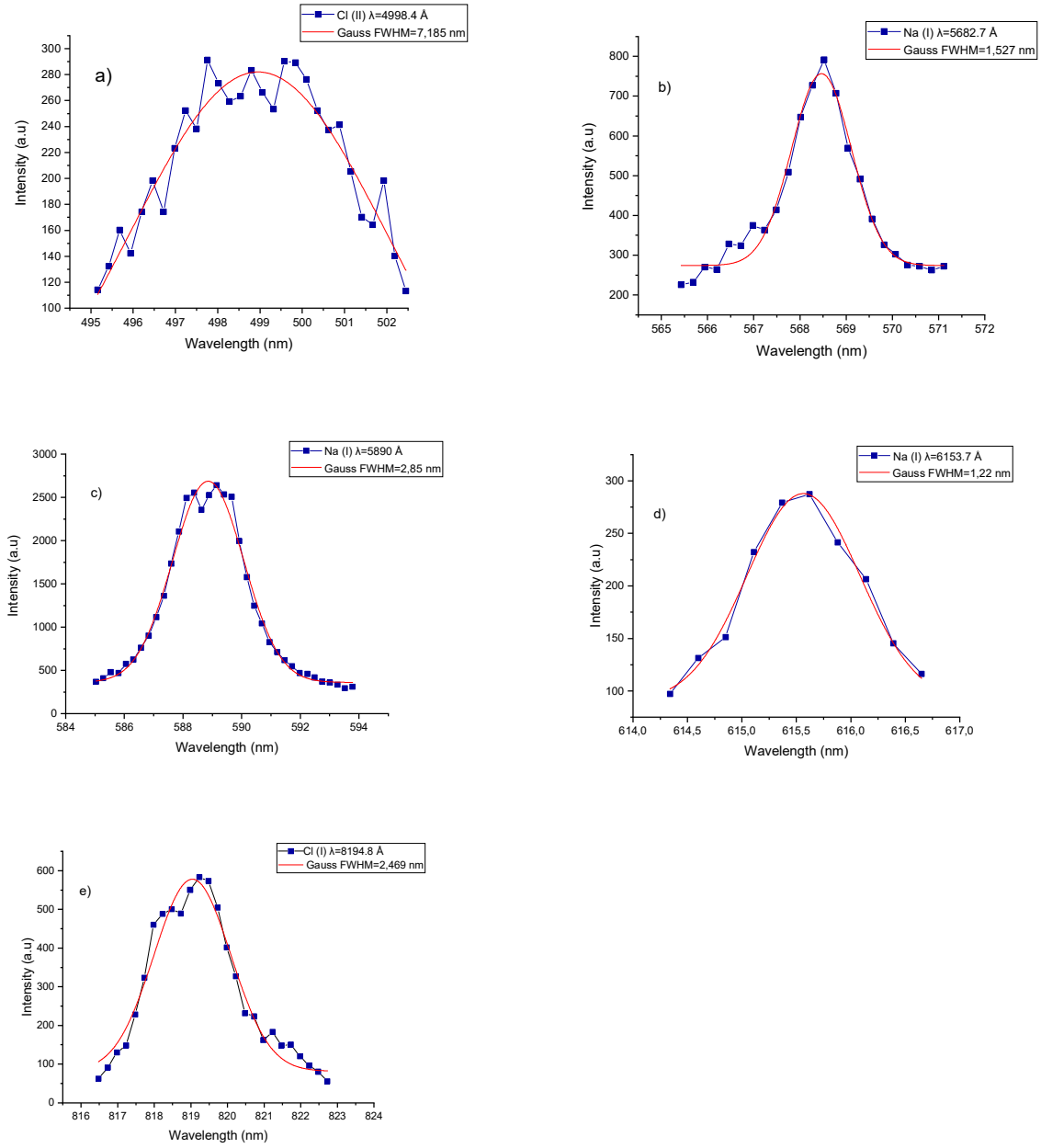

Figure 3. Plasma formed on the surface of the NaCl melt under laser irradiation *a)* Cl (II), λ = 499.84 nm b) Na I, λ = 568.27 nm, *c)* Na I, λ = 589.15 nm d) Na I, λ = 615.37 nm *e)* Cl I, λ = 819.48 nm spectral lines matching with a Gaussian pulse.

Table 1.

Atom/ion	**Wavelength $\lambda_{ki,Z}$, (nm)**	**Configuration**	**Elektronic interaction parameter w (Å)**	**Electron density n_e , $(10^{17})cm^{-3}$**
Cl (II)	499,84	$3s^2 3p^4(^1D)4p$	0,08	89,8
Na I	568,27	$2p^6 3p\text{-}2p^6 4d$	1,97	0,8
Na I	589,15	$2p^6 3s\text{-}2d^6 3p$	0,316	9,02
Na I	615,37	$2p^6 3p\text{-}2p^6 5s$	0,564	2,16
Cl I	819,48	$3s^2 3p^4(^3P)4p$	0,65	3,8

The electron density obtained independently from each selected emission line is summarized in Table 1. If a plasma were in complete thermodynamic equilibrium, its excited-state populations and particle distributions could be described by a single temperature. Laser-produced plasmas, however, do not generally reach full equilibrium. For spectroscopic analysis, the local thermodynamic equilibrium (LTE) approximation is often adopted. Under LTE conditions, collisional processes establish population distributions among energy levels sufficiently rapidly for temperature-based descriptions to be useful. The equilibration behavior differs for electrons and heavy particles because of their different masses [8]. For a plasma satisfying the local thermodynamic equilibrium approximation, the population of excited states can be represented by the Boltzmann distribution [9]:

$$\frac{n_{k,Z}}{n_Z} = \frac{g_{k,Z}}{P_Z} \exp\left(-\frac{E_{k,Z}}{k_B T}\right) \tag{3}$$

In this notation, Z identifies the ionization stage; Z = 0 and Z = 1 refer to neutral and singly ionized species, respectively. The quantities kB and T denote the Boltzmann constant and plasma temperature, while nk,Z, E(k,Z), and gk,Z describe the population, energy, and statistical weight of an excited level. The terms nZ and PZ correspond to the population and thermodynamic partition function of the relevant ionization stage. For an optically thin plasma, where self-absorption is small, the intensity Iz of a transition between two levels can be expressed in terms of the transition probability and wavelength as follows.

$$I_Z = \frac{hc}{4\pi\lambda_{ki,Z}} A_{ki,Z} L \frac{n_Z}{P_Z} g_{k,Z} \exp\left(-\frac{E_{k,Z}}{k_B T}\right) \tag{4}$$

Here h is Planck's constant, c is the speed of light, L represents the characteristic plasma length, Aki,Z is the transition probability, and λki,Z is the wavelength of the selected transition. Taking the natural logarithm of the corresponding population-intensity relation gives the linear form used for the Boltzmann analysis.

$$\ln\left(\frac{I_Z \lambda_{ki,Z}}{g_{k,Z} A_{ki,Z}}\right) = -\frac{1}{k_B T} E_{k,Z} + \ln\left(\frac{hcLn_Z}{4\pi P_Z}\right) \tag{5}$$

When the logarithmic population term is plotted against the appropriate upper-level energy for several transitions belonging to the same ionization stage, a linear dependence is obtained under the assumed LTE and optically thin conditions. The slope of this relation is directly connected with the plasma temperature. Thus, the temperature can be extracted from the fitted Boltzmann line. Using several emission lines from the same species improves the reliability of the Boltzmann-temperature estimate. In the present analysis, three neutral-sodium transitions at 568.27, 589.15, and 615.37 nm were selected and substituted into equation (5) to construct the Boltzmann plot shown in

Figure 4. The atomic parameters listed in Table 2 were used in this calculation. The fitted slope corresponds to a plasma temperature of T = 1.318 eV.

Table 2.

Atom/ion	*Wavelength $\lambda_{ki,Z}$, (nm)*	*Upper level E_k,(sm^{-1})*	*Lower level E_i,(sm^{-1})*	*High-level energy level g_k*	*Transition probability A_{ki}, (s^{-1})*
Na I	568,27	34548,76	16956,17	2	$1{,}01\times 10^{7}$
Na I	589,15	66956,17	0.000	2	$6{,}14\times 10^{7}$
Na I	615,37	33200,67	16856,17	2	$2{,}5\times 10^{6}$

The experimentally determined electron density and temperature provide the basis for estimating additional plasma properties. One such quantity is the Debye length, which characterizes the distance over which electric fields are screened in a quasi-neutral plasma.

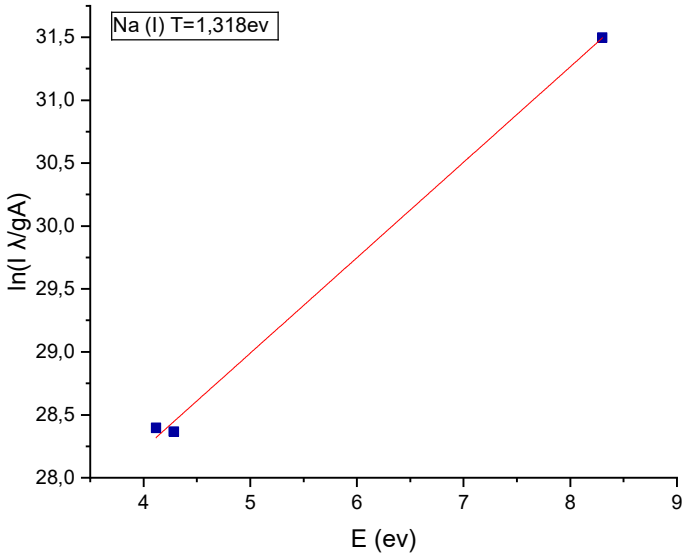

Figure 4. Boltzmann distribution plot of the Na ion transition emission spectrum lines. The slope corresponds to a plasma electron temperature of T = 1.318 eV.

Its value is determined from the electron density and temperature according to equation (6).

$$\lambda_D = \left[\frac{\varepsilon_0 k_B T_e}{N_e e^2}\right]^{1/2} \approx 743 \times \left(\frac{T_e}{N_e}\right)^{\frac{1}{2}}, \quad (cm) \qquad (6)$$

The Debye length λD may also be used to define the Debye sphere, the characteristic volume surrounding a charged particle over which screening is important. The number of charged particles contained in this sphere, ND, is obtained from equation (7).

$$N_D = \frac{4\pi}{3} N_e \lambda_D^3 \qquad (7)$$

The measured electron density also determines the characteristic oscillation rate of electrons in the plasma. This quantity is known as the plasma frequency and is obtained from equation (8).

$$\omega_p = \left(\frac{N_e e^2}{\varepsilon_0 m}\right)^{1/2} \qquad (8)$$

Here e denotes the elementary charge, m is the electron mass, and ε₀ is the vacuum permittivity. With these constants fixed, the plasma frequency is governed primarily by the electron density, as expressed by equation (9).

$$f_p = \frac{\omega_p}{2\pi} \approx 8{,}98\sqrt{N_e} \qquad (9)$$

For laser-generated plasma, the electromagnetic field does not penetrate indefinitely into the plasma. The characteristic penetration distance, commonly called the plasma skin depth (PSD), is calculated using equation (10).

$$PSD = \frac{c}{f_p} \approx 5{,}31 \times 10^5 N_e^{-\frac{1}{2}}, \quad (cm) \qquad (10)$$

Table 3.

Atom/ion	*FWHM (Å)*	*λ_D (10^{-4} sm)*	*N_D (10^6)*	*f_p(GHz)*	*PSD(sm)*
Cl (II)	71.85	0.3063	1.08	26.9	0.0177
Na I	15.2	3.248	11.47	2.54	0.188
Na I	28.5	0.967	3.41	8.53	0.056
Na I	12.2	1.976	6.97	4.17	0.114
Cl I	24.69	1.49	5.26	5.53	0.086

For every selected spectral line, the measured electron density and temperature were used to calculate the Debye length, the number of particles in the Debye sphere, the plasma frequency, and the skin depth; the resulting values are listed in Table 3. Another relevant process is inverse bremsstrahlung (IB), in which free charged particles gain energy from the electromagnetic field during collisions. In the laser-produced plasma, interaction of the laser field with free electrons and ions can consequently contribute to absorption. Under the conditions of this experiment, the corresponding absorption coefficient was evaluated from equation (11).

$$\alpha_{IB} = 1{,}37 \times 10^{-26} \lambda^3 N_e^2 T_e^{-1/2}, \qquad (11)$$

In equation (11), λ is the wavelength of the incident laser radiation. The experiment used λ = 1064 nm. The electron velocity distribution in a hot plasma depends on both particle energy and temperature. A characteristic thermal electron velocity for the investigated plasma can therefore be estimated from equation (12).

$$v_{T_e} = \sqrt{\frac{k_B T_e}{m_e}} \approx 4{,}19 \times 10^7 T_e^{\frac{1}{2}}, \ (cm/s) \qquad (12)$$

The electron–ion collision frequency is another important parameter because collisions affect energy transfer and the interaction of the plasma with the electromagnetic field. For the measured electron density and temperature, this rate was determined from equation (13).

$$v_{ei} = 2{,}9 \times 10^{-6} N_e T_e^{-3/2} ln\Lambda\,, \quad \left(\frac{cm}{s}\right) \qquad (13)$$

Here the Coulomb logarithm and the ionic charge state enter the collision description. At a specified electron temperature, the characteristic thermal de Broglie wavelength of the electrons can be calculated from equation (14).

$$\lambda_{th,e} = \sqrt{\frac{h^2}{2\pi m_e k_B T_e}} \approx 6{,}919 \times 10^{-8} \frac{1}{T_e^{\frac{1}{2}}}\,, \quad (14)$$

To further characterize the NaCl plasma, four additional quantities were evaluated: the inverse-bremsstrahlung absorption coefficient, thermal electron velocity, electron–ion collision frequency, and thermal de Broglie wavelength. Their values for the selected spectral lines are presented in Table 4.

Table-4.

Atom/ion	$v_{Te}(10^9$ cm/s)	α_{IB} (10^{-12}cm^{-1})	V_{ei} (10^6s^{-1})	$\lambda_{th,e}$ (10^{-9} cm)
Cl (II)	5.18	1115.8	212	5.47
Na I		0.13	2.26	
Na I		18.4	23.85	
Na I		1.2	5.9	
Cl I		8.8	10.3	

Conclusion and Recommendations

Solid NaCl sample was investigated in a vacuum of 10^{-2} Torr using pulsed Nd:YAG laser irradiation at 1064 nm with a 20 ns pulse duration. Optical emission spectroscopy was applied to characterize the resulting plasma. Electron density was derived from Stark broadening of selected Na and Cl emission lines, while the electron temperature was obtained from a Boltzmann analysis of three Na I transitions. The measured density and temperature were then used to calculate the Debye length, Debye-sphere population, plasma frequency, skin depth, inverse-bremsstrahlung absorption coefficient, electron thermal velocity, electron–ion collision frequency, and thermal de Broglie wavelength. These results provide a spectroscopic description of the plasma produced from the binary NaCl material and can support further interpretation of the physical processes taking place during laser–matter interaction.

References:

[1] J. M. Gomba, C. D'Angelo, D. Bertuccelli and G. Bertuccelli, Spectrochim. Acta Part B 56, 695 (2001)
[2] D. A. Cremers and L. J. Radziemski, Handbook of Laser-Induced Breakdown Spectroscopy (John Wiley & Sons, Ltd, Chichester, 2006)
[3] A. W. Miziolek, V Palleschi and I Schechter, Laser-induced breakdown spectroscopy (LIBS): Fundamentals and applications (Cambridge University Press, New York, 2006)
[4] J. S. Cowpe, R D Pilkington, J S Astin and A E Ahill, J. Phys. D: Appl. Phys. 42, 165202 (2009)
[5] H. R. Griem, Plasma Spectroscopy (McGraw-Hill, New York, 1964).
[6] Experimental Stark widths and shifts for spectral lines. J. Phys. Chem. Ref. Data, Vol.31, No. 3, 2002.

[7] B. Verhoff, S. S. Harilal, "Dynamics of femto- and nanosecond laser ablation plumes investigated using optical emission spectroscopy" JOURNAL OF APPLIED PHYSICS 112, 093303 (2012)
[8] David A. Cremers, Leon J. Radziemski, Basics of the LIBS Plasma. "Handbook of Laser-Induced Breakdown Spectroscopy" 2013// DOI:10.1002/9781118567371
[9] H R Griem, Principles of plasma spectroscopy (Cambridge University Press, Cambridge, 1997)
[10] NIST Atomic Spectra Database, http://physics.nist.gov
[11] J. A. A. C. Aragón, "Characterization of laser-induced plasmas by optical emission spectroscopy: A review of experiments and methods," Spectrochimica Acta Part B: Atomic Spectroscopy, vol. 63, pp. 893–916, 2008.
[12] B. R. Nek M Shaikh, S Hafeez, Y Jamil and M A Baig, "Measurement of electron density and temperature of a laser-induced zinc plasma," Journal of Physics D: Applied Physics, vol. 39, pp. 1384-1391, 2006.
[13] D. R. C. S. Yalcin, G.P. Smith, G.W. Faris, "Influence of ambient conditions on the laser air spark" Applied Physics B, vol. 68, pp. 121–130, 1999.
[14] Seesahai, Brandon, "Plasma Temperature Measurements in the Context of Spectral Interference" (2016). Honors Undergraduate Theses. 140.
[15] W F Luo, X X Zhao, "Characteristics of the aluminum alloy plasma produced by a 1064 nm Nd:YAG laser with different irradiances". Pramana – J. Phys., Vol. 74, No. 6, June 2010

UDC: 537.5:546.83

THERMIONIC EMISSION PROPERTIES OF OXIDIZED HAFNIUM, ZIRCONIUM, TITANIUM, AND NIOBIUM IN A BARIUM ATOM FLUX

Tursunmetov Kamiljan Axmetovich
Professor, Faculty of Physics, National University of Uzbekistan
Turgunboyev Farxod Yusupjanovich
Director, named of S. Kh. Sirojiddinov Academic Lyceum under the National University of Uzbekistan
fturgunboev573@gmail.com
Ergasheva Iroda Islomjon qizi
Physics Teacher, School №. 86, Yunusabad District, Tashkent, Uzbekistan

Annotatsiya. Ushbu maqolada bariy atomlari oqimida oksidlangan o‘tuvchi metallar (Hf, Zr, Ti va Nb) ning termoemission hamda adsorbsion xususiyatlari o‘rganilgan. Namunalar sirtining tozaligi va oksidlanish jarayoni yuqori vakuum sharoitida Oje-elektron spektroskopiyasi usuli bilan nazorat qilingan. Eksperimental natijalar shuni ko‘rsatdiki, toza metallarning chiqish ishi bir-biriga yaqin bo‘lishiga qaramay, ularning kislorod va bariy bilan o‘zaro ta’siri taglik metallining kristall panjarasi simmetriyasiga kuchli bog‘liq. Geksagonal zich joylashgan (GZU) kristall panjaraga ega bo‘lgan Hf, Zr va Ti da uch o‘lchamli suboksidlar hosil bo‘lib, kislorod hajmga chuqur diffuziyalanadi va sirtda bariyning adsorbsiyasi kuchsiz kechadi. Natijada Hf–O–Ba va Zr–O–Ba tizimlarida elektronning chiqish ishi 3,10–3,20 eV darajasida yuqori saqlanib qoladi. Bu esa qoplamasiz dispenser katodlarga nisbatan emissiya toki zichligini qariyb 10^4 martaga kamaytirish imkonini beradi. Aksincha, hajmiy markazlashgan kubik (OTsK) panjarali niobiyda kislorod sirtda qolib, tizimning dipol momentini oshiradi va chiqish ishini keskin pasaytiradi. Olingan natijalar asosida Hf va Zr

plyonkalarini 1100–1300 K ishchi haroratlarda ishlaydigan termoelektron katodlar uchun yuqori samarali antiemission materiallar sifatida qo‘llash tavsiya etiladi.

Kalit so‘zlar: *Termoelektron emissiya, elektronning chiqish ishi, antiemission metallar, gafniy, titan, sirkoniy, niobiy, volfram, oksid, suboksid.*

Аннотация. В данной статье исследованы термоэмиссионные и адсорбционные свойства окисленных переходных металлов (Hf, Zr, Ti и Nb) в потоке атомов бария. Чистота поверхности и процесс окисления образцов контролировались методом оже-электронной спектроскопии в условиях сверхвысокого вакуума. Экспериментальные данные показали, что несмотря на близкие значения работы выхода чистых металлов, их взаимодействие с кислородом и барием существенно зависит от симметрии кристаллической решетки подложки. В металлах с гексагональной плотноупакованной (ГПУ) решеткой (Hf, Zr, Ti) формируются объемные трехмерные субоксиды, кислород диффундирует вглубь объема, а адсорбция бария на поверхности оказывается слабой. В результате работа выхода систем Hf–O–Ba и Zr–O–Ba сохраняется на высоком уровне 3,10–3,20 эВ, снижая плотность тока термоэмиссии примерно в 10^4 раз по сравнению с открытой поверхностью катода. Напротив, в объемно-центрированном кубическом (ОЦК) ниобии кислород локализуется на поверхности, увеличивая дипольный момент и снижая работу выхода. На основе полученных результатов пленки гафния и циркония рекомендуются в качестве высокоэффективных антиэмиссионных материалов в интервале температур 1100–1300 К.

Ключевые слова: *термоэлектронная эмиссия, робота выход электрона, антиэмиссионные металлы, гафний, титан, цирконий, ниобий, вольфрам, оксид, субоксид.*

Abstract. This paper investigates the thermionic emission and adsorption properties of oxidized transition metals (Hf, Zr, Ti, and Nb) exposed to a flux of barium atoms. The surface cleanliness and oxidation kinetics were monitored using Auger electron spectroscopy under ultra-high vacuum conditions. The experimental findings reveal that despite similar initial work functions of the clean metals, their interaction with oxygen and barium is fundamentally governed by the substrate crystal lattice symmetry. In metals with a hexagonal close-packed (hcp) crystal lattice (Hf, Zr, Ti), three-dimensional interstitial suboxides are formed, where oxygen is strongly bound within the bulk lattice, resulting in weak barium adsorption on the surface. Consequently, the work functions of the Hf–O–Ba and Zr–O–Ba systems remain significantly high at 3.10–3.20 eV, thereby suppressing the thermionic emission current density by roughly 10^4 times compared to uncoated dispenser cathodes. In contrast, for body-centered cubic (bcc) niobium, oxygen localizes at the surface, increasing the dipole moment and markedly lowering the work function. Based on these insights, thin films of hafnium and zirconium are recommended as highly efficient anti-emission coatings operating at 1100–1300 K.

Key words: *thermionic emission, robot electron yield, anti-emission metals, hafnium, titanium, zirconium, niobium, tungsten, oxide, suboxide.*

Introduction

Investigating the emission properties of metals with hexagonal close-packed (hcp) crystal structures, which are utilized as anti-emission materials in electron devices, is of substantial scientific and practical interest for developing multi-beam electron sources and shaping electron beams of predetermined configurations [1]. This issue has acquired heightened relevance in connection with the development of modified multi-beam electron systems for aerospace engineering applications [2].

The emission characteristics of zirconium, hafnium, and titanium have been investigated by numerous authors [3, 4], as well as in our previous works [5, 6]. Study [7] addressed the thermal stability of thin films of these metals, their influence on the emission properties of metal-barium and metal-oxygen-barium systems [8], and their anti-emission performance. In addition, the temperature regimes ensuring the stability of these metal films were identified [7].

Research Methodology

In the present study, the comparative emission properties of Hf, Zr, Ti, and Nb in a barium atom flux were investigated. Their oxidation in an oxygen ambient and subsequent surface composition were monitored under ultra-high vacuum conditions using Auger electron spectroscopy (AES). The operating base pressure was maintained at $\leq (1\text{-}2) \times 10^{-9}$ Torr.

The Hf, Zr, and Ti specimens were prepared from iodide-refined rods and fabricated in the form of disks with a thickness of 1-1.5 mm and a diameter of 10-16 mm.

For comparative analysis, polycrystalline niobium samples were likewise investigated, as niobium exhibits a work function comparable to those of Hf, Zr, and Ti, but possesses a different crystal structure-specifically, a body-centered cubic (bcc) lattice. This distinction provides insight into the role of the crystal lattice symmetry in the adsorption mechanism of barium atoms, as well as the specific role of oxygen in the formation and stabilization of the metal-oxygen-barium (Me-O-Ba) system.

The surface cleaning of the metals, thermionic emission measurements, and surface elemental composition monitoring via Auger electron spectroscopy (AES) were conducted in an all-metal ultra-high vacuum system. The apparatus was equipped with an oil-free pumping system capable of achieving and maintaining a base pressure of (1-2) 10^{-9} Torr.

The Auger spectrometer, equipped with a four-grid retarding field quasi-spherical analyzer, had an energy resolution of 0.4%.

The barium source was a molybdenum quasi-Knudsen cell loaded with “BaTi” getter pellets. The cell was equipped with an integrated heater and a W-Re (BP-5/20) thermocouple to monitor the temperature.

The work functions of the pristine samples and Me-O-Ba systems were determined using the total current and contact potential difference methods. This was realized by mounting an electron gun on the anode assembly (Faraday cup). The dipole moment of barium on the target surfaces was evaluated from the work function versus coverage degree curves measured at specified substrate temperatures. The emission and

adsorption characteristics of all specimens were examined in a barium atom flux with an intensity of 1.2×10^{12} atoms/($cm^2\cdot s$).

Following system outgassing, the samples were subjected to high-temperature thermal flashing under a vacuum of $(1\text{-}5)\times10^{-9}$ Torr, and the surface state was continuously monitored by AES. Upon the complete disappearance of Auger peaks corresponding to oxygen, carbon, and other residual contaminants, the thermionic emission current was measured, and the work function of the clean substrate was determined using the total current method.

The measured work function values were 3.95 ± 0.05 eV for hafnium, 3.85 ± 0.05 eV for zirconium, 4.05 ± 0.05 eV for titanium, and 4.0 ± 0.05 eV for niobium. These values are in good agreement with our previous findings [3-5] as well as published literature data [9].

Analysis and results

Subsequently, barium adsorption curves on the Zr, Hf, Ti, and Nb substrates were recorded at temperatures of 1000, 1100, and 1200 K, and the minimum work function (φ_{min}) values of the systems were identified. At T = 1000 K, the values were as follows:

- Ti–Ba system: $\varphi_{min} = 2.35 \pm 0.05$ eV
- Hf–Ba system: $\varphi_{min} = 2.38 \pm 0.05$ eV
- Zr–Ba system: $\varphi_{min} = 2.36 \pm 0.05$ eV
- Nb–Ba system: $\varphi_{min} = 2.35 \pm 0.04$ eV

These results are consistent with reported literature data [9]. The marginal variation among the minimum work function values of the Me-Ba systems can be explained by the Langmuir model, as the initial work functions of the underlying substrates are close to one another, lying within the narrow range of 3.85-4.05 eV.

It should also be noted that these values show negligible dependence on the substrate crystal structure, despite Zr, Hf, and Ti possessing a hexagonal close-packed (hcp) lattice, whereas Nb exhibits a body-centered cubic (bcc) structure.

The oxidation procedure was carried out in an oxygen ambient at a pressure of $(5 \pm 1) \times 10^{-6}$ Torr and a substrate temperature of T = 1000 K for 30 minutes. Following oxidation, oxygen was evacuated, and the samples were annealed at T = 1100 K for 30 minutes under a base pressure of $p \leq (1\text{-}2) \times 10^{-9}$ Torr to stabilize the surface composition and structure.

Thereafter, barium adsorption curves were recorded in the Ba flux at 1000, 1100, and 1200 K, and the minimum work function values of the Me-O-Ba systems were determined. Oxidation of the systems with an hcp crystal lattice induced only a slight decrease (≤ 0.10 eV) in the minimum work function, whereas in the Nb-O-Ba system this reduction reached 0.20-0.25 eV. This observation confirms the hypothesis regarding the formation of bulk suboxides in metals with an hcp lattice structure.

To evaluate and compare emission characteristics, S-curves of the oxidized metals exposed to the barium atom flux were measured at T = 1000 K. Based on these relationships, temperature dependencies of the work function for the Me-O-Ba systems were constructed, as presented in Figure 1.

The temperature dependence of the work function for the W-O-Ba system is also included for comparison. A comparative analysis of these data substantiates the conclusion that the interaction is relatively weak. This indicates that the adsorption of barium atoms on oxidized zirconium and hafnium surfaces is relatively weak. Under the operating temperatures of impregnated dispenser cathodes, the work functions of the Hf-O-Ba and Zr-O-Ba systems range from 3.10 to 3.20 eV. These values are approximately ~1 eV higher than the work functions of such thermionic cathodes. Consequently, the thermionic emission current density from anti-emission coatings of hafnium or zirconium is about 10^4 times lower than that from the uncoated cathode surface. This behavior fully satisfies the performance requirements for anti-emission materials. The temperature dependence of the work function for the Ti-O-Ba system differs from those of the Hf-O-Ba and Zr-O-Ba systems. This discrepancy is likely associated with the relatively higher solubility of oxygen in titanium, which facilitates maintaining a higher oxygen concentration on the metal surface during the experiment.

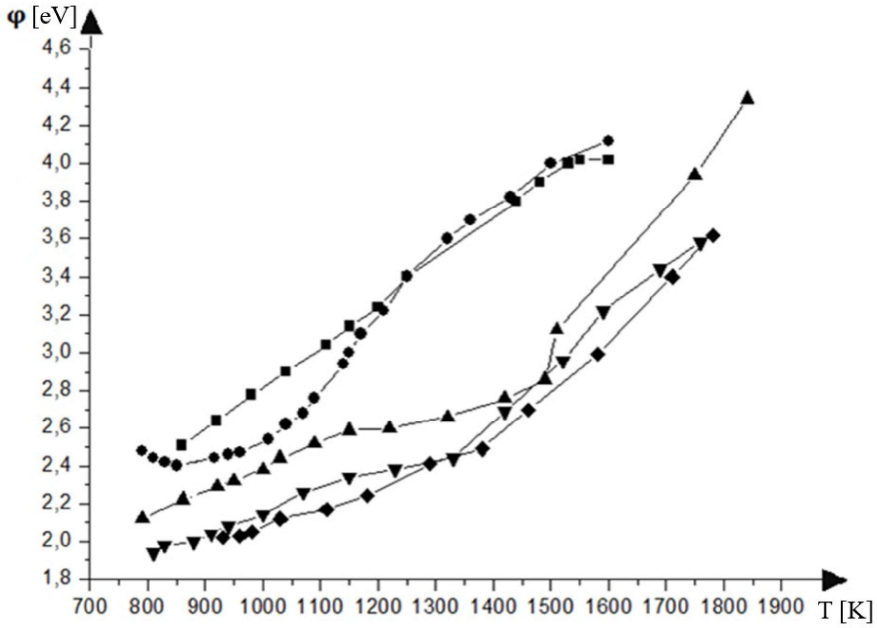

Figure 1. Temperature dependence of the work function for oxidized metals Hf (■), Zr (●), Ti (▲), V (▼), and Nb (◆) in a barium atom flux. The experiment was conducted at T = 1000 K. The oxidation procedure was carried out at an oxygen pressure of 5×10^{-6} Torr for 30 minutes.

The weak adsorption of barium atoms on oxidized hafnium and titanium compared to niobium and tungsten, alongside the minimal impact of oxygen on the emission and adsorption properties of zirconium and hafnium in a barium flux, is difficult to reconcile using classical frameworks. This is primarily because the initial work functions of these metals (excluding W) are all clustered around ~4 eV. However, the experimental data demonstrate that the thermal stability and emission efficiency of Me-O-Ba systems vary significantly and are strongly governed by the crystal lattice symmetry of the underlying metal.

Conclusion and Recommendations

During the oxidation of metals with a hexagonal close-packed (hcp) crystal lattice, such as Hf, Zr, and Ti, “bulk” (three-dimensional) suboxides of the Me_3O and Me_6O types are formed [10]. Oxygen atoms integrate into the interstitial sites of the hcp crystal

lattice, establishing exceptionally strong chemical bonds that yield stable suboxide structures of the Me_6O and Me_5O types. However, the oxygen atoms situated within the bulk lattice of Zr and Hf do not substantially enhance the interaction forces between the adsorbate atoms and the adsorbent. Therefore, when barium (or other electropositive atoms) adsorbs onto such oxidized metals, the work function of the system does not experience a significant reduction.

Under these conditions, as previously reported in [5], neither the dipole moment of the adsorbed atoms nor the heat of adsorption undergoes substantial modification on the surfaces of metals with an hcp crystal lattice.

In contrast, during the oxidation of niobium and tungsten-which crystallize in a body-centered cubic (bcc) lattice-three-dimensional “bulk” suboxides do not form [10]. Instead, oxygen atoms localized on the metal surface significantly enhance the dipole moment of the Me-O-Ba system, leading to a substantial decrease in its work function.

The concept outlined above is embodied in the model of Me-O-Ba and Me-O-Cs emission systems developed by K.A. Tursunmetov, F.Y. Turgunboyev, and E.Z. Imomov [11]. By taking into account the adsorbate configuration and the film structure of the emission system, this model consistently elucidates the physical mechanisms of efficient emission systems without internal contradictions.

Consequently, thin films of hafnium and zirconium can be recommended as highly effective anti-emission materials within the operating temperature range of thermionic cathodes (1100-1300 K).

References

[1] Pobedonostsev, A. S., & Sazonov, B. V. (2013). Electronics, Series 1: Microwave Technology, 3(518), 131–135.

[2] Melnikova, I. P. (2014). *Development of technological processes for fabricating cathode systems with improved physical and technical characteristics for high-power electrovacuum devices* (Doctoral dissertation). Saratov, 263 p. [in Russian].

[3] Dyubua, B. Ch., & Ermolaev, L. A. (1964). Anti-emission and anti-dynatron materials. *Voprosy Radioelektroniki. Ser. I. Elektronika*, (12), 176 [in Russian].

[4] Dyubua, B. Ch., & Popov, B. I. (1965). Some emission and adsorption properties of the barium-titanium system. *Voprosy Radioelektroniki. Ser. 1. Elektronika*, 10(6), 1161 [in Russian].

[5] Tursunmetov, K. A., & Gurkov, Yu. V. (1993). Investigation of the emission properties of clean and oxidized titanium, zirconium, and hafnium in a barium atom flux. *Uzbek Journal of Physics*, (5), 49 [in Russian].

[6] Tursunmetov, K. A., Turgunboyev, F. Yu., & Khamidjanov, I. Kh. (2010). Thermionic emission properties of the W-Hf-Ba system. *Uzbek Journal of Physics*, (1-2), 71 [in Russian].

[7] Tursunmetov, K. A. (1994). Investigation of the thermal stability of Ti, Zr-Hf thin films on tungsten surfaces. *Technical Physics Letters (Pis'ma v ZhTF)*, (19), 71 [in Russian].

[8] Tursunmetov, K. A., & Turgunboyev, F. Yu. (2016). In: *Proceedings of the Symposium "New Trends in the Development of Fundamental and Applied Physics" (IPS)*, Tashkent, November 10-11, p. 149.

[9] Fomenko, V. S. (1981). *Emission Properties of Materials: A Handbook*. Kiev: Naukova Dumka [in Russian].

[10] Kornilov, I. I., & Glazova, V. V. (1967). *Interaction of Refractory Metals of Transition Groups with Oxygen*. Moscow: Nauka, 253 p. [in Russian].

[11] Tursunmetov, K. A., & Imamov, E. Z. (1999). Detailed structural model of Me-O-Cs and Me-O-Ba emission systems. *Inorganic Materials (Izvestiya AN SSSR: Neorganicheskie Materialy)*, (9), 1 [in Russian].